

**DEVELOPMENT AND EXPERIMENTAL
VERIFICATION OF THE STIFFNESS MATRIX OF
THE HIPHAD HAPTIC DEVICE**

**A Thesis Submitted to
the Graduate School of Engineering and Science of
İzmir Institute of Technology
in Partial Fulfillment of the Requirements for the Degree of**

MASTER OF SCIENCE

in Mechanical Engineering

**by
Barış TANER**

**November 2015
İZMİR**

We approve the thesis of **Bariř TANER**

Examining Committee Members:

Assist. Prof. Dr. M. İ. Can DEDE

Department of Mechanical Engineering, İzmir Institute of Technology

Assist. Prof. Dr. Gökhan KİPER

Department of Mechanical Engineering, İzmir Institute of Technology

Assist. Prof. Dr. Erkin GEZGİN

Department of Mechatronics Engineering, İzmir Katip Celebi University

29 November 2015

Assist. Prof. Dr. M. İ. Can DEDE

Supervisor, Department of Mechanical
Engineering, İzmir Institute of
Technology

Prof. Dr. Metin TANOĞLU

Head of the Department of Mechanical
Engineering

Prof. Dr. Bilge KARAÇALI

Dean of the Graduate School of
Engineering and Sciences

DEDICATION

I dedicate this thesis to my parents Emine and Atilla Taner.

ACKNOWLEDGMENTS

I would never have been able to finish my dissertation without the guidance of my committee members, help from friends, and support from my family.

I would like to thank my parents, my brother, aunt and uncle and the rest of my family for their good wishes and support. I would like to express my deepest gratitude to my supervisor Assist. Prof. Dr. M. İ. Can Dede for his excellent guidance, caring, patience and immense knowledge. His guidance helped me in every project we were in and enlightened me in all the time of research and writing of this thesis.

I would like to express my gratitude to Assist. Prof. Gökhan Kiper, Assoc. Prof. H. Seçil Artem and Prof. Serhan Özdemir for their guidance and help throughout this thesis.

In particular, I would like to thank my dear friends and colleagues in IZTECH Robotics Lab. for their friendship, support and the fun they brought to the Lab., Emre UZUNOĞLU, Osman Nuri ŞAHİN, Emre TAVKAYA, Mert KANIK, Gün GÜZDÜZALP, Onur ÇELİK, Omar MAAROOF, Gizem ATEŞ, Çağhan KİRİŞÇİ, Barış ÇELİK(in short “çe”) and Mehmet KİRAZ.

ABSTRACT

DEVELOPMENT AND EXPERIMENTAL VERIFICATION OF THE STIFFNESS MATRIX OF THE HIPHAD HAPTIC DEVICE

In this work the evaluation of stiffness performance of HIPHAD haptic device has been studied with 2 semi-analytical and an experimental method in order to obtain the stiffness characteristics of the haptic device for precise motion tracking performance. Since the compliance of a robot depends highly on robot configuration and force is variable in the haptic applications, stiffness properties of main robot elements and methods of evaluating stiffness of a robot manipulator is investigated considering the computational costs. Virtual Joint Method (VJM) and Structural Matrix Analysis (SMA) method is applied to the case study. Although, structural matrix analysis reduces the computational time dramatically by reducing the node elements it is not accurate as Finite Element Analysis (FEA) method. Comparing the VJM to the SMA, it is applicable to online application due to its simplicity and flexibility. In addition, with FEA based link modelling VJM is as accurate as FEA method in finding stiffness of the manipulator. While both methods can include flexible joints FEA based link stiffness parameters computational costs for these methods is the performance criteria for choosing one. For the case study HIPHAD, the VJM method provides better result in terms of flexibility and computation cost with 0.035 seconds finding the resultant force while SMA method calculates result in 0.074 seconds.

Keywords and Phrases: virtual joint method, structural matrix analysis, stiffness, experimental Stiffness Analysis, haptics, HIPHAD

ÖZET

HIPHAD HAPTİK CİHAZININ DİRENGENLİK MATRİSİNİN OLUŞTURULMASI VE DENEYSEL OLARAK DOĞRULANMASI

Bu çalışmada, HIPHAD haptic cihazının direngelik karakteristiği, hassas hareket takibi sağlayabilmesi için, iki yarı analitik ve bir de deneysel yöntem ile bulunmuştur. Haptik uygulamalarda kuvvetin büyüklüğü ve yönü değişken olduğundan ayrıca robotların direngelik matrislerinin mafsalsal açılarına bağlı olarak değişiklik göstermesinden dolayı, robot kollarının direngelik matrisinin çıkarılmasında kullanılan metotlar gerektirdikleri hesaplama zamanı düşünülerek araştırılmıştır. Bu tezde Sanal Mafsalsal Metodu ve Yapısal Matris Analizi yöntemleri kullanılmıştır. Yapısal Matris Analizi metodu her ne kadar hesaplama zamanını azaltıyor olsa da modelin doğruluğu azalmaktadır. Sanal mafsalsal metodu ve yapısal matris analizi kıyaslandığında, sanal mafsalsal metodu daha esnek ve basit bir modelleme yöntemi sunmaktadır. Bunun yanı sıra sonlu elemanlar analizi kullanılarak bulunan direngelik değerleri sayesinde bu yöntem, sonlu elemanlar analizi kadar isabetli sonuçlar verebilmektedir. Yapısal matris analizi de sanal mafsalsal metodu da esnek mafsalsal modellerinde bulundurulabilir. Dolayısıyla bu iki metot arasındaki belirleyici fark hesaplama zamanlarından gelecektir. HIPHAD için VJM metodu daha doğru sonuçlar vermiştir. Yapısal matris analizi metodu ve sanal mafsalsal metodu için bir döngünün çözüm süresi 0.074 sn ve 0.035 olarak ölçülmüştür.

Anahtar Kelimeler ve Deyimler: sanal mafsalsal metodu, yapısal matris analizi, direngelik, deneysel direngelik analizi, haptik, HIPHAD

TABLE OF CONTENTS

LIST OF FIGURES	ix
LIST OF TABLES	xiii
CHAPTER 1 INTRODUCTION	15
CHAPTER 2 LITERATURE SURVEY.....	22
2.1. Possible Sources of Errors in Haptic Devices	23
2.2. Compensation Methods for Inaccuracy Factors.....	27
2.3. Stiffness Analysis of Robot Manipulators	30
2.3.1. Structural Matrix Analysis in Stiffness Modeling of Robot Manipulators	31
2.3.2. Finite Element Analysis in Stiffness Modeling	42
2.4. Conclusion for Literature Survey.....	58
CHAPTER 3 CASE STUDY: A PARALEL MECHANISM HAPTIC DEVICE	61
3.1. General Information and Specifications of HIPHAD v1.0	61
3.2. Hardware Used in the Haptic Device.....	63
3.3. Kinematic Analysis of the Haptic Device	65
3.4. Quasi-static Equilibrium Force Analysis	72
3.5. Calibration of the Haptic Device.....	84
3.6. Stiffness Calculation of HIPHAD Using SMA.....	89
3.7. Stiffness Calculation of HIPHAD Using VJM	95
CHAPTER 4 EXPERIMENTAL TEST SETUP	100
CHAPTER 5 RESULTS	109
5.1. Experimental Results	113

5.2. Semi-Analytical Results.....	122
5.2.1. Semi-Analytical Results of VJM	123
5.2.2. Semi-Analytical Results of SMA	131
5.3. Comparison	139
CHAPTER 6 CONCLUSIONS	145
REFERENCES	148

LIST OF FIGURES

<u>Figure</u>	<u>Page</u>
Figure 2.1 Diagram showing accuracy and spatial resolution (ISO 9283 Deifinition) ..	23
Figure 2.2 Positional accuracy metrics of a robot.	24
Figure 2.3 Inaccuracy factors of robot manipulators (Klimchik, 2011).	26
Figure 2.4 Modification of the trajectory of the manipulator depending on the robot model (Source: Klimchik et al., 2014).	29
Figure 2.5 Decomposition of a serial chain.	32
Figure 2.6 Coordinates of a revolute joint	35
Figure 2.7 Equivalent beam representing the manipulator for stiffness calculations	40
Figure 2.8 A rigid body defined by nodes v and w. The displacements of these nodes are given with dP_v , δ_v , dP_w and δ_w	40
Figure 2.9 Forcing on legs of parallel robot under an external forcing	47
Figure 2.10 A slender beam fixed from one end and subjected to a force from the other end. \vec{F} , \vec{M} and $\Delta\vec{S}$ are 3x1, 3x1 and 6x1 vectors defining the force, moment and deflection of the beam.	49
Figure 2.11 Link collecting the stiffness properties of the links in the serial chain	52
Figure 2.12 Test setup for stiffness matrix evaluation (Clinton, Zhang & Wavering, 1997).	55
Figure 2.13 Schematic for Stiffness measurement. The measurement is made by measuring the retroreflector with a laser tracker (Alicı & Shirinzadeh, 2005).	56
Figure 2.14 Milli-CATRASYs measuring device (Ceccarelli & Carbone, 2005).	57
Figure 3.1 In (a), location of the encoders are given by numbers 1, 2 and 3. In (b) enlarged view of encoder 1 is given	63
Figure 3.2 HIPHAD v1.0 device composed of 1) BLDC amplifier Box 2) Maxon Motor BLDCs 3) Quadrature Encoders	65
Figure 3.3 Translational parallel mechanism parameters	66
Figure 3.4 (a) Link and joint parameters (b) Joint limit (Dede et al., 2014).	67
Figure 3.5 Active and passive joint angles of a leg	68

Figure 3.6 Geometric and Kinematic properties of 3rd and 4th links of the 1 st leg	70
Figure 3.7 Geometric divisions of links and nodes represented for leg 1	73
Figure 3.8 Free Body Diagram of link 3 and link 4 of leg1	74
Figure 3.9 FBDs of l41, l42, l43 and l44 that are decomposed from link 4.	77
Figure 3.10 Reaction forces and moments on nodes for link 3.	79
Figure 3.11 FBD of the parallelogram.....	81
Figure 3.12 Test Setup for calibration	85
Figure 3.13 Checkerboard pattern in different orientations for calibration.	85
Figure 3.14 Construction of the total stiffness matrix \hat{K}_T of each leg.....	91
Figure 3.15 Construction of the overall \hat{A}_T matrix of a leg.....	92
Figure 3.16 Global stiffness matrix, \hat{K}_G of HIPHAD.....	92
Figure 3.17 Equivalent stiffness model of the mobile platform	93
Figure 3.18 Kinematic model of leg 1 of HIPHAD.....	96
Figure 4.1 Parameters affecting the selection of cameras for machine vision (Source: Calculating Camera Sensor Resolution and Lens Focal Length, 27.06.2014, http://digital.ni.com/)	102
Figure 4.2 Experimentation basement.	103
Figure 4.3 Brake replacement for the actuators.....	104
Figure 4.4 Complete experimentation setup.....	105
Figure 4.5 Experimentation stages.....	106
Figure 4.6 Meshes applied on the image plane.....	107
Figure 4.7 (a) Tracking patterns having 4 different circles. (b) Result of pattern tracking	107
Figure 4.8 (a) Non-interpolated and non-filtered measurement result. (b) Sub-pixel Interpolated and filtered measurement result.....	108
Figure 5.1 Placement of the nodes for experimentation.	109
Figure 5.2 Force vs Compliant Displacement at (220,220,220).	110
Figure 5.3 Procedure of joint stiffness estimation	112
Figure 5.4 Compliant displacement values of HIPHAD in u1-axis on Plane 1.	114
Figure 5.5 Compliant displacement values of HIPHAD in u1-axis on Plane 2.	115
Figure 5.6 Compliant displacement values of HIPHAD in u1-axis on Plane 3.	116

Figure 5.7 Compliant displacement of the HIPHAD under 700 g of force along (+)u1-axis throughout its workspace.....	116
Figure 5.8 Compliant displacement values of HIPHAD in u2-direction on Plane 1. ..	117
Figure 5.9 Compliant displacement values of HIPHAD in u2-direction on Plane 2. ..	118
Figure 5.10 Compliant displacement values of HIPHAD in u2-direction on Plane 2. ..	118
Figure 5.11 Compliance displacement of the HIPHAD under 700 g forcing along (+)u2-direction throughout its workspace.....	119
Figure 5.12 Compliant displacement values of HIPHAD in u3-direction on Plane 1. ..	120
Figure 5.13 Compliant displacement values of HIPHAD in u3-direction on Plane 2. ..	120
Figure 5.14 Compliant displacement values of HIPHAD in u3-direction on Plane 3. ..	121
Figure 5.15 Compliance displacement of the HIPHAD under 700 g forcing along (-)u3-direction throughout its workspace.....	122
Figure 5.16 Calculated compliant displacement values of HIPHAD by VJM in u1-direction on Plane 1.	123
Figure 5.17 Calculated compliant displacement values of HIPHAD by VJM in u1-direction on Plane 2.	124
Figure 5.18 Calculated compliant displacement values of HIPHAD by VJM in u1-axis on Plane 3.....	125
Figure 5.19 Calculated compliant displacement values of HIPHAD by VJM in u2-direction on Plane 1.	126
Figure 5.20 Calculated compliant displacement values of HIPHAD by VJM in u2-direction on Plane 2.	127
Figure 5.21 Calculated compliant displacement values of HIPHAD by VJM in u2-direction on Plane 3.	128
Figure 5.22 Calculated compliant displacement values of HIPHAD by VJM in u3-direction on Plane 1.	129
Figure 5.23 Calculated compliant displacement values of HIPHAD by VJM in u3-direction on Plane 2.	130
Figure 5.24 Calculated compliant displacement values of HIPHAD by VJM in u3-direction on Plane 3.	131
Figure 5.25 Calculated compliant displacement values of HIPHAD by SMA in u1-direction on Plane 1.	132

Figure 5.26 Calculated compliant displacement values of HIPHAD by SMA in u1- direction on Plane 2.	133
Figure 5.27 Calculated compliant displacement values of HIPHAD by SMA in u1- direction on Plane 3.	134
Figure 5.28 Calculated compliant displacement values of HIPHAD by SMA in u2- direction on Plane 1.	135
Figure 5.29 Calculated compliant displacement values of HIPHAD by SMA in u2- direction on Plane 2.	136
Figure 5.30 Calculated compliant displacement values of HIPHAD by SMA in u2- direction on Plane 3.	136
Figure 5.31 Calculated compliant displacement values of HIPHAD by SMA in u3- direction on Plane 1.	137
Figure 5.32 Calculated compliant displacement values of HIPHAD by SMA in u3- direction on Plane 2.	138
Figure 5.33 Calculated compliant displacement values of HIPHAD by SMA in u3- direction on Plane 3.	139
Figure 5.34 Surface plots representing the errors between VJM displacements and measured displacements on u1-direction.....	140
Figure 5.35 Surface plots representing the errors between VJM displacements and measured displacements on y-direction.....	142
Figure 5.36 Surface plots representing the errors between VJM displacements and measured displacements on u3-direction.....	143

LIST OF TABLES

<u>Table</u>	<u>Page</u>
Table 2.1 Denavit-Hartenberg parameters of links 1, 2, 3 and 4 to be combined in multi-beam approximation of the complex beam.....	52
Table 3.1 Specifications of HIPHAD v1.0 Design.....	62
Table 3.2 Specifications of Quanser Q8 DAQ	64
Table 3.3 Forces transmitted to the N17 node of each leg.	74
Table 3.4 Measured values from cameras and calculated joint limits by using potentiometers.....	87
Table 3.5 Measured Values from Cameras and Calculated Joint Limits by using Encoders	87
Table 3.6 Number of pulses read from the encoders.....	88
Table 3.7 Material and geometric properties of links.....	89
Table 3.8 Denavit-Hartenberg(D-H) parameters of 1 st leg's VJM model	97
Table 4.1 Hardware and software list.	100
Table 4.2 Camera Parameters	101
Table 5.1 External forces resulting in displacements given in Figure 5.2.....	110
Table 5.2 RMSE of compliant displacements calculated by VJM calculations results and experimental measurements in u1-axis	141
Table 5.3 RMSE of displacements calculated by VJM and measured in experimentation in u2-direction	142
Table 5.4 RMSE of displacements calculated by VJM and measured in experimentation in u3-direction	144

CHAPTER 1

INTRODUCTION

Haptics term describes the sense of touch. It is a concept that originated in ancient times and it is derived from the Greek term "haptios", which describes anything that can be touched. This sense binds the other senses and therefore it has an indispensable place in human perception. The sense of touch is used in different manners in human body such as the boundary of the human body (receptors under the skin) is used to perceive distances and calibrate sense of vision (Kern, 2009).

Humans are not only using the sense of touch for feeling physical boundaries but we are also receiving information about the texture of objects. Discrimination of objects are vital for humans; for example, it enables us to feel whether something is harmful or not, e.g. when touching a hot pan or holding a glass filled with cold water. This type of haptic sensation makes it possible for humans to feel textures that range from 1 μm to a few millimeters (Kern, 2009), which can be surface of a glass or a fabric. On the other hand, humans are also capable of qualifying the objects according to their weight and hardness. The two mechanisms for haptic sensation in our bodies are named as tactile and kinesthetic sensing. Tactile sensing is achieved through the nerve ends located under our skin, which provides us the information of heat, pressure and texture (Varalakshmi, 2012). On the other hand, kinesthetic sensing provides information about the kinesthetic parameters of the environment which are motion, location, weight, and rigidity (Bilgincaan et al., 2010).

Although, haptic information is important for humans to perceive spatial information, the first sensory information that were used in human machine interactions are visual and auditory information. With the technological improvements in data processing and transferring units, the haptic information are started to be used in human machine interactions (Bilgincaan et al., 2010). Human machine interactions in terms of haptic information exchange are realized by haptic devices. These haptic devices can be operated to communicate with a virtual reality environment (VR) or a teleoperated remote

system in a real distant environment and get the multimodal sensory information (Varalakshmi, 2012), (Hirche & Buss, 2012). Here "multimodal" refers to the perceptual capabilities of human being, which are visual, auditory and haptic senses. Haptic devices can be both kinesthetic devices and/or tactile devices, which are providing kinesthetic sensory information such as, motion and force and/or tactile sensory information such as texture and temperature of a surface (Kern, 2009). From now on, the concept haptics will cover the kinesthetic sub-senses, e.g. sensing force and motion.

Haptic feedback in teleoperated systems provide users extensive knowledge about the distant site and increases the feeling of being present in the remote site, which is generally termed as telepresence. Therefore, it enables the users to perform more complex and precise objectives in the remote environment. During the haptic interaction, not only the force and position information about the environment is provided to the user, but also it allows the user to manipulate (by means of a telerobotic manipulation) the distant environment, which is referred to as slave environment in a teleoperation setting or virtual environment in virtual reality (VR) applications. During this manipulation not only the positional information but also the velocity and the acceleration of the contact of the slave device can be reflected to the user. In this case motion tracking of the haptic master device should be improved for a precise operation, since the chain composed of remote environment, teleoperator or VR and haptic device is closed with the human user (Hirche & Buss, 2012). However, as this kind of systems are human-in-the-loop-systems, the performance of the haptic system highly relies on the physical coupling and visuo-haptic co-location of the users hand and the slave device in remote environment through haptic interface.

Physical coupling in haptic applications refers to transmit the mechanical resistance of the remote environment to the user and the mechanical resistance is the impedance. Mechanical impedance Z is the ratio of force, F , to the velocity, v , respectively ratio of the moment, M , to angular velocity, ω . Measures for the level of coupling of human and remote environment are presented by (LAWRANCE, 1992), (Yokokohji & Yoshikawa, 1994), (Hokayem & Spong, 2006) as transparency and by (Colgate & Brown, 1994) as impedance width.

Transparency, T , is a factor that gives the relation of the input impedance, which is the impedance of the remote environment interaction, Z_{in} and the felt impedance by the user referred to as output impedance, Z_{out} , given in Equation 1.1.

$$T = \frac{Z_{in}}{Z_{out}} \quad (1.1)$$

This means that, when transparency of a system gets close to "one", the input impedance is not distorted by the haptic system. Therefore, the user controlling the haptic device feels the input impedance perfectly. If a device has a transparency greater than one, then this device cannot mimic the stiffness of the contact occurring in the slave site and a softer contact force is felt by the user (Kern, 2009) Impedance width, Z -width, provides the impedance range that can be stably provided by the haptic device. Therefore, Z -width measure provides us the information about the difference between the minimum and maximum impedance of the haptic device. Z_{min} stands for the minimum resistance, which is induced by the friction and inertial properties of the motors, joints and links of the haptic device and felt by the user during free motion. Z_{max} gives the maximum impedance that can be rendered by the haptic device under a very stiff contact condition. The mathematical representation for Z -width is provided in Equation 1.2.

$$Z - \text{width} = Z_{max} - Z_{min} \quad (1.2)$$

In haptic systems, Z -width and Transparency which are used to identify the performance of the system, are related to the factors such as sampling time of the controller, encoder quantization and unavoidable dynamic properties of the haptic device that are friction, inertia, backlash and stiffness (Koul, Manivannan & Saha, 2013) (Lee et.al., 2010). Other than improving the controllers, algorithms and sensors, the mechanical design of haptic devices are fronting the advanced kinematic structure with high-strength and light-weight materials and reduced cross-sections of the links (Ahmad et al., 2014). While using light-weight materials with reduced cross-sections reduces Z_{min} in terms of decreasing the perceived inertia during free motion, it also affects adversely the mechanical stiffness properties of the haptic device that is directly related to Z_{max} , transparency and positional accuracy (Carbone, 2003).

Positional accuracy is an important parameter in fusing the visual and kinesthetic feedback that is named as visuo-haptic. Seeing the remote device and receiving the kinesthetic stimuli at the same spatial location improves the perception of the remote environment and makes the interaction more natural. This spatial information of the visual and haptic feedback can be misaligned due to a physical property of the haptic device which is the stiffness (Barbieri et al., 2014). Consequently, performance criteria of haptic devices, which is described previously, have a common variable that is the stiffness of a haptic device.

Bodies under load change their reference configuration into final configuration, which are their deformed shapes, also known as compliant displacements (Przemieniecki, 1985). The same rule exists for the multi-body mechanical systems, such as robot manipulators. As defined in (Rivin, 1999), stiffness is the capacity of a mechanical systems to sustain loads without excessive changes of its geometry. In a more quantitative way, stiffness is defined as ratio of force applied on a deformable body to the compliant displacements (NOF, 1985). Therefore, if a robotic structure has high stiffness values, then it can resist more forces without compromising its positional accuracy. The structures having low stiffness are called to be compliant. Although, level of compliance of a robot indicates the safety of the manipulator while working with a human and provides advantages in assembly processes, it has an adverse impact on positional accuracy. Therefore, in applications that require better positional accuracy and stiffness, such as haptic devices, low compliance and high stiffness is desired. However, compliance of a human-machine interface can also serve for increasing the safety of the user. The level of the required compliance of a haptic device relies on the application. When a haptic device is used for rehabilitation purposes, the main performance criterion becomes the controllable compliance and not positional accuracy and when a haptic device is used in critical missions such as surgical robotics, the main performance criterion becomes the positional accuracy.

Relying on the previously described basis, the motivation of this master thesis study is to develop the stiffness model of a kinesthetic haptic device to evaluate and in the future studies possibly improve its stiffness characteristics and position tracking accuracy. The kinesthetic haptic device, HIPHAD, constructed in Iztech Robotics

Laboratory, IRL, by (Bilginca et al., 2010) for high precision haptic applications is the haptic device used for the case study in this thesis.

This thesis focuses on evaluation of stiffness matrix of HIPHAD under quasi-static equilibrium configuration, which can be also referred as unloaded mode. This means that deflections due to external loads are small enough so that the relation between deflections and forces can be assumed as linear. Structural Matrix Analysis method (SMA), and Virtual Joint Method (VJM), among the other stiffness calculation methods are used to obtain an analytical stiffness matrix equation. The calculated stiffness matrices are compared to each other with respect to the performance criteria, which are computational time and accuracy of the used methods. The actual stiffness values of the case study are acquired using an experimental method, in which the deflections are measured with vision sensors. The data acquired in the experiments are used in verifying the results obtained by the SMA method and VJM method. To achieve this goal, the listed objectives are set:

1. Design and construction of the test setup including external force exertion mechanisms and camera mounting structure.
2. Employment of image processing methods for accurate and high resolution positional measurement in three-dimensional (3D) environment.
3. Stiffness matrix calculation of HIPHAD device.
4. Verification of the stiffness matrix calculations through experiments
5. Stiffness characteristics mapping of HIPHAD device throughout its workspace.

The contributions of this thesis work are:

1. Measurement of compliant displacements with vision sensors.

The compliant displacements are measured using stereo-vision cameras and image processing techniques. This technique, allows us to measure the stiffness of a mechanism without any electro-mechanical component attached to the mechanism that changes the stiffness characteristics. Since there is no mechanical connection between the

robot and the measurement device, this method can be applied to mobile robots, e.g. humanoids.

2. Extension of the analysis of HIPHAD device by its stiffness evaluation that can possibly be used to increase motion tracking accuracy.

HIPHAD device was developed within High Precision Haptic Device Design project funded by EU FP7 Marie-Curie International Re-integration Grant to be used in high precision applications. In this manner, it was constructed with low density aluminum alloy and high precision brushless-DC (BLDC) motors. In order to increase its performance in terms of motion tracking accuracy, its stiffness characteristics are evaluated for the first time.

3. Obtaining an analytical stiffness matrix expression of HIPHAD device that is suitable for implementing in online compliant error compensation techniques.

Since forces will be random in a haptic application, integrating a computationally effective expression for stiffness matrix in an impedance controller and using this controller in the master system will improve the force transmission and motion tracking performance of a haptic device.

Preliminary works for this study have been published and presented in an international proceeding of ROMANSY-2014 XX CISM-IFTtoMM SYMPOSIUM. The study was executed in the course of improving the accuracy of the HIPHAD device was executed to calibrate and experimentally validate the kinematics of a novel haptic device. HIPHAD v1.0. External measurement of the absolute position of the mechanism was carried out by using a vision-aided algorithm, which is 2-D correlation, on the images taken by the cameras facing along 13 and 12 directions. Calibration of the mechanism was made by measuring the positive and negative end of the workspace and relating them to the sensor voltages. Test results also indicate the precision errors in manufacturing and assembling the device which are accounted for by performing the calibration. Vision-aided measurements were experimented and calibration of forces exerted by the mechanism to the human operator is pointed as a future work.

This master thesis is composed of 6 chapters and these chapters are Introduction, Literature Survey, Analytical Stiffness Calculation of HIPHAD, Experimental Evaluation

of Stiffness Matrix of HIPHAD, Test Results and Conclusion. In second Chapter, possible error sources in haptic devices are listed and compensation techniques for these errors are provided. In addition, analytical and experimental methods for developing stiffness matrix of robot manipulators are given and digital image processing techniques for object tracking is provided. In Chapter 3, the stiffness matrix calculation of HIPHAD device with SMA and VJM is provided. Chapter 4 is dedicated to experimental method for stiffness matrix evaluation of HIPHAD. After that, analytical and experimental results are provided in Chapter 5. Finally, evaluation on the outcomes of the methods are made and conclusions are presented in Chapter 6.

CHAPTER 2

LITERATURE SURVEY

Examples for haptic applications can be sorted with respect to their need for precision from coarse applications such as entertainment and art design to fine applications such as medical operations. Precision of a haptic device can be affected by a number of factors. In order to understand these factors, haptic device operation conditions should be taken into consideration. In haptic applications, force feedback is sent to the user through haptic devices and under contact condition, these forces result in the compliant bending of the haptic device. The force transmission and motion tracking capability of the haptic device is crucial in precise haptic applications, since any divergence between master and slave device motions and/or weak force transmission will result in a faulty perception of the slave environment by the user and an undesired motion of the slave device. To identify and improve the performance of a haptic device, performance criteria like motion tracking accuracy, transparency and Z-width has to be understood and parameters influencing these criteria has to be exposed. One of these parameters is the stiffness of the haptic device since the stiffness properties of haptic devices directly affect all the mentioned performance criteria.

In this chapter, sources of errors that degrade the performance of haptic devices are listed. Methods for compensating these errors are then provided and on-line compensation methods in the literature for eliminating the effects of compliant errors are reviewed. In this work, offline compensation methods are disregarded since in a high precision master-slave haptic application there is no pre-determined trajectory of the master device. Methods developed for evaluating stiffness matrix of robot mechanisms are provided in order to determine the compliance errors. Later, experimental methods for calibration of the robots and verification of robot mechanisms' stiffness matrices are presented. Finally, analytical and experimental methods for calculating stiffness properties of robots are discussed and compared.

2.1. Possible Sources of Errors in Haptic Devices

In general, performance of a robot manipulator is given by two noteworthy points. They are payload and positional accuracy of the robot manipulator and performance of the manipulator is determined by these factors. These terms are explained in (Merlet, 2006) and metrics for payload capacity is given by payload/weight ratio which is the load that a robot can carry per its unit weight. In evaluation of the positioning accuracy usually three metrics are used as absolute accuracy, repeatability and resolution (Klimchik, 2011). Absolute accuracy is defined in as robot's ability of positioning its wrist at a desired target within workspace. In this sense, it is defined as one-half of the resolution. Accuracy of a robot arm depends on the mechanical inaccuracies, control algorithms and system resolution that is provided in Figure 2.1.

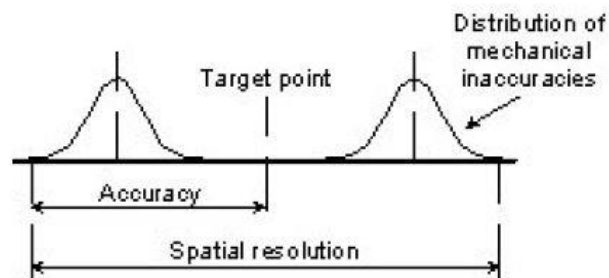


Figure 2.1 Diagram showing accuracy and spatial resolution (ISO 9283 Definition)

The repeatability is a term giving the numerical value of maximum difference between numerous measurements of position that a robot can achieve for a desired pose. This measure shows how a point repeated by the robot. Resolution in positioning is defined in ISO 9283 standard as the smallest incremental move that a robot can achieve. This term includes the effects of two distinguished factors that are control resolution and programming resolution. Control resolution is the smallest reading that a position sensor can do and the programming resolution is the smallest allowable position increment and

referred to as the basic resolution unit (BRU). These positional accuracy metrics are provided in Figure 2.2 as an example.

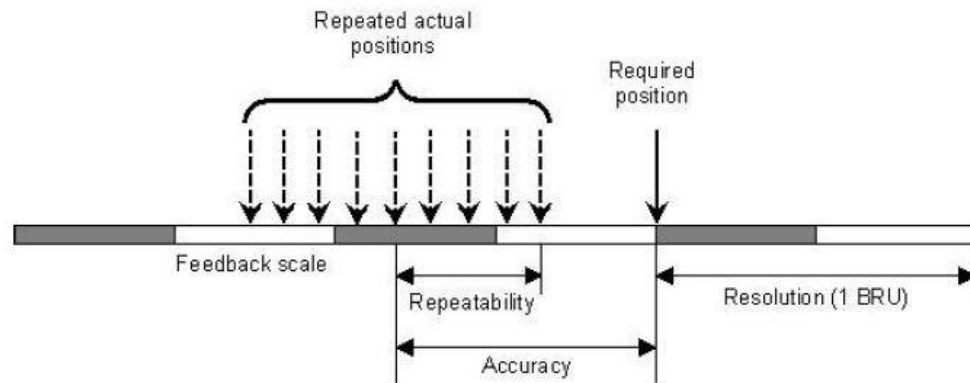


Figure 2.2 Positional accuracy metrics of a robot.

Considering the haptic systems, mainly two control schemes exist, which are admittance and impedance type controllers. For haptic systems having admittance type of controller, user exerts force on the haptic master device and this force is converted to motion command through an admittance model. Slave robot is manipulated with this motion command and measured position of the slave robot is sent back to the haptic master device. On the other hand, systems having impedance type of controller has to receive motion command from the user and send it to the slave site. Then the contact forces are displayed to the user. Concerning the mentioned schemes, position tracking of the haptic master device is important for displaying the position signals coming from the slave environment in the systems that have admittance type of controller. For haptic systems having impedance type of controller, haptic master device displays force signals coming from the slave site; therefore, it is the force signal to be tracked. Due to the mentioned control natures of admittance and impedance type of haptic systems, performance criteria introduced for industrial robots are valid for haptic master devices with admittance controller. For haptic master devices with impedance controller, key point is not tracking the absolute position of the slave robot but tracking the force with respect to the motion of the slave robot (penetration velocity and depth occurring in the slave site between the environment and the slave robot). In this concept, performance

criteria defined for industrial robots do not completely match with the task executed by impedance type of haptic devices. In this thesis an impedance type of haptic device is the subject and for this device motion tracking is affected by the encoder resolution and compliance of the links and actuators.

In haptic applications, besides the tracking accuracy, another performance measure is the ability of a haptic device to transmit the impedance characteristics of the slave environment (Baser, 2012). This performance measure is related to the design features of haptic devices that are transparency and Z-width. The design features, which are mentioned in the Introduction section, are affected by the stiffness properties of the actuator and the mechanism. High stiffness in robot manipulators like haptic devices can be achieved by using over-constraint mechanisms as robot structure and high-strength links in manipulator construction. Increasing stiffness of haptic devices improves the Z-max, however, at the same time it negatively affects Z-min and transparency due to the frictional forces created on the bearings resulted from the internal stresses and the inertia of the haptic device resulted from the increased weight of the high-strength links.

Motion tracking and force transmission performance of haptic devices are affected by the same factors that affect the positioning performance of industrial robots. Positioning performance degradation of a robot is a result of the accumulation of the errors that are divided into two main categories given in (Meggiolaro, Dubowsky & Mavroidis, 2004) and (Gong, Yuan & Ni, 2000). Inaccuracy factors in robotic manipulators are listed in Figure 2.3.

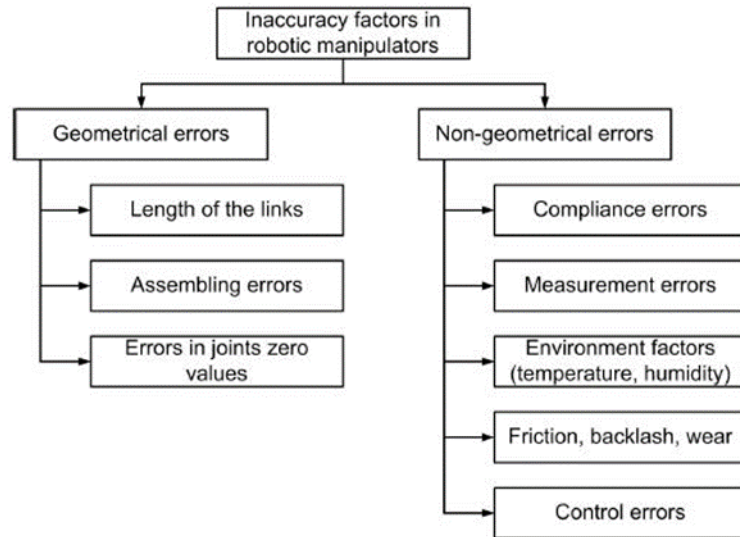


Figure 2.3 Inaccuracy factors of robot manipulators (Klimchik, 2011).

Geometrical errors that are listed in Figure 2.3 originate from non-ideal geometry of the links and joints of the robot manipulator. Deviation in the geometry of robot parts are results of the errors occurred in manufacturing and assembly processes. Any deviations in orthogonality, parallelism of the links and joints, differences in the link lengths and errors in joint zero values are reasons of geometrical errors (Meggiolaro, Dubowsky & Mavroidis, 2005 ; Chen & Chao, 1987). The effects of geometrical errors are observed as differences between the nominal and actual pose of the end-effector. It is the reason of the 90% of the errors in positional accuracy of robot manipulators under free motion or relatively small forces (Klimchik, 2011). These factors affecting the positional accuracy in industrial robots also affect the motion tracking performance of a haptic device. Non-geometric errors, however, are results of environment factors, such as humidity, temperature, actuator deficiencies, measurement errors and control errors (Aoyagi et al., 2012). Among the non-geometrical errors that are listed in Figure 2.3, influence of the compliance errors is the most significant error source in tracking performance of haptic devices (Di Alessio et al., 2004).

In haptic applications there are two separate phases with respect to the force applied by the device namely, the free motion phase and the contact phase. Haptic device in free motion is back-driven by the user force that is required only to overcome the

minimum impedance of the device, which is induced by the inertia and the friction of haptic device. Therefore in this phase, geometric errors dominate non-geometric errors due to constant environmental factors, measurement, backlash friction wear and control errors, which are the similar to industrial robots working in free space (Klimchik, 2011). This phase continues until the slave system on remote environment makes a contact with its surrounding environment.

When a contact is made in the slave environment and acquired force measurements are sent to haptic device at the user side, it is now a new phase in which perception of impedance of the contacted object in remote site becomes important. Impedance of the contact condition is displayed by the haptic device to the user by exerting forcing to the user through the handle of the device. Haptic devices tend to deform under this forcing. This is not desired for precise tracking of the haptic device handle since the actual position of the handle deviates from the acquired position of the handle. Obviously, this is true when the motion acquisition sensors are placed in the joint composition of the haptic device mechanism, which is the usual exercise in commercially available haptic devices. Therefore, in contact condition, the non-geometrical errors dominate the geometrical errors and calculation of them becomes important (Lopez, 2012).

In order to reach higher performance ratings in motion tracking of haptic devices, compensation of geometric and non-geometric errors is critical. For this reason, methods found in the literature for compensating the geometric and non-geometric errors are provided in the next section.

2.2. Compensation Methods for Inaccuracy Factors

A common compensation technique for geometric errors is to calibrate the position calculation algorithm by measuring the absolute position of the end-effector. Measurement methods in robot calibration are listed in (Kosić, Đalić & Marić, 2010), (Švaco et al., 2014) and (Schwenke et al., 2008) as, laser projection, theodolite, 2D machine vision, portable coordinate measuring machines, stereo vision camera systems

and laser tracking devices. Measured errors can be given by linear equations if they are geometric errors (Meggiolaro, Dubowsky & Mavroidis, 2005), hence they can be compensated in the workspace of the robot by feeding them into the robot controller with the nominal joint values (Gong, Yuan & Ni, 2000). Another example for compensating such an error was done by (Dede et al., 2014). In this work, absolute position of the HIPHAD haptic device was measured by stereo vision system and active joint limits were calculated using these measurements.

Methods used in calibration cannot be applied for the errors that are not linear in the workspace such as non-geometric errors created by payloads, thermal effects and measurement errors. For these kind of errors compensation is done in two means that are off-line and on-line compensations. In off-line compensation, errors on the control points or nodes are mapped and trajectory is modified with respect to these errors. In the works of many researchers, who are working on error compensation of machining centers, modification of the desired trajectory is generally applied in this way. In this direct approach, a primary absolute position measurement is made for the first operation and errors are recorded then for the following operations the path is modified according to the measured errors (Shen et al., 2012).

In the work of (Klimchik et al., 2014), an off-line compensation method depending on the stiffness properties calculated under the auxiliary loads and external forces is made. Robot control program that defines the trajectory is modified with respect to the calculated deformations. Differing from the previously given methods, in this approach internal sensors that are already on the robot are used given in Figure 2.4.

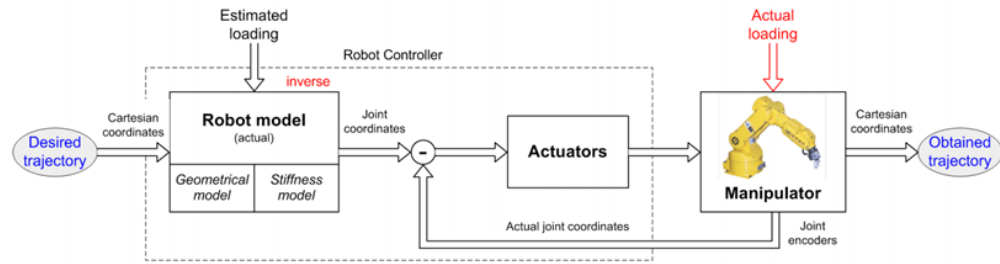


Figure 2.4 Modification of the trajectory of the manipulator depending on the robot model (Source: Klimchik et al., 2014).

Method explained in Figure 2.4 incorporates the stiffness model of the robot in the robot controller, which calculates the joint coordinates according to desired trajectory and estimated loading.

(Wang, Yu, & Liao, 2004) introduced the compensation of compliant errors based on the error prediction and compensation by NC-code conversion which can be applied on-line. In this method, accumulated errors in the workspace as a result of geometric, gravity and stiffness effects are predicted and these errors vary with respect to the robot configuration and applied external forces. Finally, trajectory is modified and it is fed into the servo controller of the NC machine via NC conversion software.

In haptic device applications, forces can be displayed in any direction and magnitude. Maintaining a better motion tracking between the master and the slave devices, while displaying these random forces, requires computation of compliant errors and compensation of the slave trajectory sent from the master side in real time. Therefore, on-line compensation provides best solution for the compensation of compliant errors for haptic device applications. The difficulty in applying an on-line compensation method stems from the complexity of the mathematical stiffness model for especially multi-DoF systems. Calculation of the stiffness matrix provides the relation between the forces exerted on the robot and the compliant displacements of the robot mechanism, which are the reason of the compliant errors at the end-effector. Therefore, in the next subsection, methods for stiffness analysis for robot manipulators are explained.

2.3. Stiffness Analysis of Robot Manipulators

The linear relation between the external forces acting on the end-effector and displacement of the end-effector due to the external forces is generally given by the stiffness matrix, \hat{K} , (Clinton, Zhang, & Wavering, 1997) and provided in the Equation 2.1. The diagonal elements of \hat{K} constitute the relation of the force and compliant displacements, when the coupling of these deformations is not taken into account. However, to represent the coupling between the compliant displacements and rotations, non-diagonal elements of stiffness matrix can be presented in \hat{K} . The linear relation in Equation 2.1 is valid only for small magnitudes of displacements $\Delta\bar{S}$ and under static conditions (Carbone, 2003).

$$\bar{W}=\hat{K} \cdot \Delta\bar{S} \quad (2.1)$$

The external load vector \bar{W} is also known as wrench which has linear and rotational elements as provided in Equation 2.2.

$$\bar{W}=(F_x,F_y,F_z,T_x,T_y,T_z)^T \quad (2.2)$$

In Equation 2.2, F_x , F_y and F_z are external force components and T_x , T_y and T_z are the external moment components applied on the manipulator's end effector and $\Delta\bar{S}$ is given in Equation 2.3.

$$\Delta\bar{S}=(U_x,U_y,U_z,U_\alpha,U_\gamma,U_\delta)^T \quad (2.3)$$

where U_x , U_y and U_z are the linear displacement components of the end-effector along the Cartesian coordinate axes and U_α , U_γ and U_δ are the angular displacement components of the end-effector represented in Euler angles for a selected Euler angle sequence.

For displaying minimum impedance in free motion and maximum impedance in stiff wall contact conditions, haptic devices are made of high-strength low-density materials. These materials with reduced weight and cross-sectional areas result in structural deformations under external loading conditions (Carbone, 2003). Therefore, calculation of stiffness matrix of the haptic device in early stages of the design enables the designers to improve the stiffness characteristics of the device. Moreover, a closed form stiffness matrix of the final design can also be used to improve positional accuracy during the operation.

In literature, three approaches are generally employed to find the linear relation between displacement and the external wrench for robot mechanisms. These methods are structural matrix analysis (SMA), finite element analysis (FEA) and virtual joint method (VJM). Apart from these methods, (Ceccarelli & Carbone, 2002) provides another approach called as matrix product method. All four methods are explained and discussed in the next subsections. Moreover, the identification of the link stiffness parameters and experimental methods for evaluating the stiffness characteristic of robot manipulators are provided.

2.3.1. Structural Matrix Analysis in Stiffness Modeling of Robot Manipulators

SMA is based on considering the manipulator as a spatial frame of beam elements. Originally this method is used for calculating the deformations of the structures (Przemieniecki, 1985) and it is the oldest method for finding stiffness of structures. Then this method is slightly modified to be used for calculating the deformation of robots (Clinton, Zhang & Wavering, 1997). In this method, external forces and end-effector displacements are represented by nodal forces and displacements. Nodal displacements and forces are related with nodal stiffness matrices, which depend on the geometrical and mechanical properties of the element such as configuration of the robot, link lengths, cross-sectional area of the links, Young's and Coulomb's modulus and inertias of the beams. Most recently (Deblaise, Hernot, & Maurine, 2006) have provided an analytical

method, which is a modification of the SMA method, for calculating stiffness matrix of parallel mechanisms.

In this section, SMA is given over the example of a serial chain, since the steps for calculating the stiffness matrix of a parallel robot relies on calculating each leg's stiffness as if they are distinct serial chains and then to combine them in an overall stiffness matrix of the parallel robot. Decomposition of a serial kinematic chain that is composed of joints and links for carrying out SMA is given in Figure 2.5. In this figure, the serial chain is decomposed into structural elements that are defined between the nodes 1, 2 and 3. These elements are the kinematic elements of the links of this serial chain and have their own geometric and mechanical properties which are defined with respect to their local frames. For the element between fixed-end, which is the base of the robot manipulator, and node 1, the stiffness matrix is defined in Local Frame 1. Stiffness matrix of this element gives the deformation of the node 1 under the related nodal force. For the next element that is between nodes 2 and 3, stiffness matrix is defined for the Local Frame 2. In this decomposition, joints i and j couples the nodes coming before and after these joints.

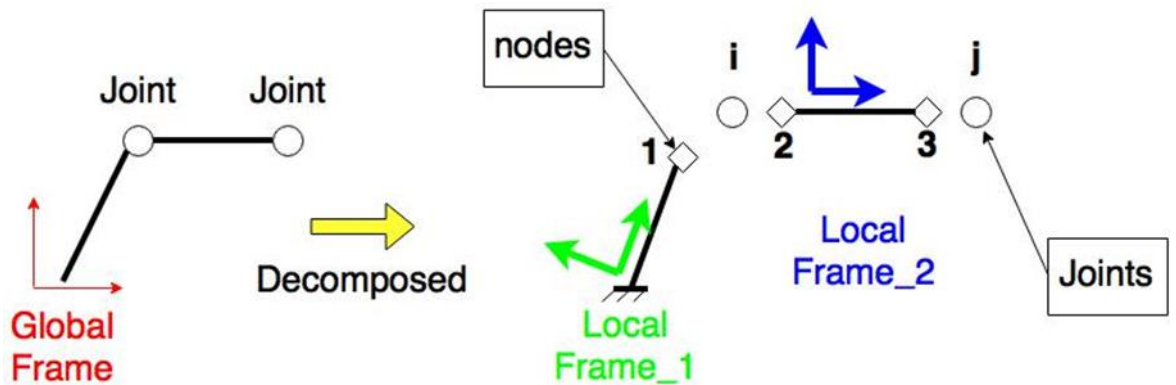


Figure 2.5 Decomposition of a serial chain.

For beam elements subjected to external wrenches, a stiffness matrix is defined and expressed in the local frame of that beam. In SMA, beams can be defined by two means (McGuire, Gallagher, & Ziemian, 2000); (1) beam that has a fixed tip and one node corresponding to the other tip, which is indicated as Link 1 in Figure 2.5, (2) beam that has two nodes on each end, which is indicated as Link 2 in Figure 2.5. Stiffness matrix of beams having one node is given by a 6x6 matrix provided in Equation 2.4.

$${}^b\hat{\mathbf{K}}^1 = \begin{bmatrix} \frac{EA}{L} & 0 & 0 & 0 & 0 & 0 \\ 0 & \frac{12EI_z}{L^3} & 0 & 0 & 0 & \frac{-6EI_z}{L^2} \\ 0 & 0 & \frac{12EI_y}{L^3} & 0 & \frac{6EI_y}{L^2} & 0 \\ 0 & 0 & 0 & \frac{GJ}{L} & 0 & 0 \\ 0 & 0 & \frac{6EI_y}{L^2} & 0 & \frac{4EI_y}{L} & 0 \\ 0 & \frac{-6EI_y}{L^2} & 0 & 0 & 0 & \frac{4EI_y}{L} \end{bmatrix} \quad (2.4)$$

In Equation 2.4, the indices of ${}^b\hat{\mathbf{K}}^1$ matrix indicate base as b and link frame number as 1. Elements of the matrix are calculated using the flexible beam assumption given in (McGuire, Gallagher, & Ziemian, 2000). For beams having two nodes, the stiffness matrix can be represented by a 12x12 square matrix, given in Equation 2.5.

$${}^2\hat{\mathbf{K}}^2 = \begin{bmatrix} {}^2\hat{\mathbf{K}}_{22}^2 & {}^2\hat{\mathbf{K}}_{23}^2 \\ {}^2\hat{\mathbf{K}}_{32}^2 & {}^2\hat{\mathbf{K}}_{33}^2 \end{bmatrix} \quad (2.5)$$

${}^2\hat{\mathbf{K}}_{ij}^2$ given in Equation 2.5 stands for the stiffness matrices of the nodes, which relates the displacement of a node to a nodal force. Subscripts i and j identifies the acting point of forces and nodes that stiffness matrix is built for, respectively (Przemieniecki, 1985). After this matrix is developed in its local frame, then it is transformed to the base frame to be superposed with the other stiffness matrices. This transformation of the local stiffness matrix ${}^2\hat{\mathbf{K}}_{ij}^2$ is accomplished by using a rotation matrix given in Equation 2.6. Transformation equation for the local stiffness matrix is shown in Equation 2.7.

$$\hat{\mathbf{P}} = \begin{bmatrix} \hat{\mathbf{R}}^{(b,2)} & 0 & 0 & 0 \\ 0 & \hat{\mathbf{R}}^{(b,2)} & 0 & 0 \\ 0 & 0 & \hat{\mathbf{R}}^{(b,2)} & 0 \\ 0 & 0 & 0 & \hat{\mathbf{R}}^{(b,2)} \end{bmatrix} \quad (2.6)$$

$${}^b \hat{\mathbf{K}}^2 = \hat{\mathbf{P}} \cdot {}^2 \hat{\mathbf{K}}^2 \cdot \hat{\mathbf{P}}^{-1} \quad (2.7)$$

In Equation 2.6, $\hat{\mathbf{R}}^{(b,2)}$ stands for the 3x3 rotation matrix from world frame to the local frame 2. As the stiffness values for links are calculated with respect to the same base frame, they can be superposed and assembled in a global stiffness matrix. For the example given in Figure 2.5, the stiffness matrix assembly becomes,

$${}^b \hat{\mathbf{K}}_T = \begin{bmatrix} {}^b \hat{\mathbf{K}}^1 & \mathbf{0}_{6,6} & \mathbf{0}_{6,6} \\ \mathbf{0}_{6,6} & {}^b \hat{\mathbf{K}}_{22}^2 & {}^b \hat{\mathbf{K}}_{23}^2 \\ \mathbf{0}_{6,6} & {}^b \hat{\mathbf{K}}_{32}^2 & {}^b \hat{\mathbf{K}}_{33}^2 \end{bmatrix} \quad (2.8)$$

In this equation $\mathbf{0}_{6,6}$ is 6 by 6 zero matrix.

After the stiffness properties of the robot mechanism are calculated, the kinematic relations between nodal displacements are developed to model the joints of the structure and the elements that are considered to be rigid. Characteristic of the revolute joint is that all motions of the nodes 1 and 2 are the same except the rotational motion of node 2 about the joint axis z_{21} .

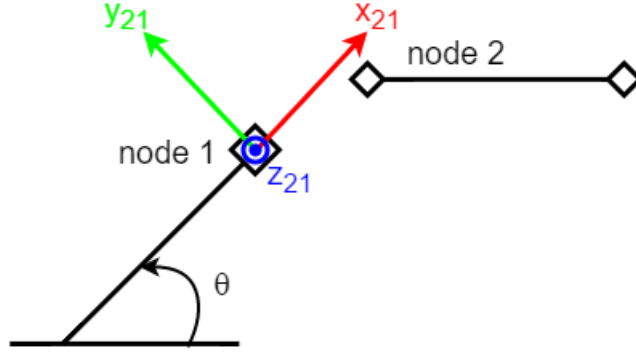


Figure 2.6 Coordinates of a revolute joint

Since all of the stiffness matrices, which relates the nodal displacements to the nodal wrenches, are defined according to the world frame, x_{21} and y_{21} unit vectors should also be written in the world frame. These unit vectors given in Figure 2.6 are extracted from the rotation matrix of the related frame by finding the projection of the unit vectors on world frame. This projection is done by multiplying the rotation matrix $R^{(b,2)}$ which is provided in Equation 2.6 with the x , y and z axes defined on the world frame that is given by ${}^b x_{21}$, ${}^b y_{21}$ and ${}^2 x_{21}$, ${}^2 y_{21}$ in Equation 2.9 stands for the unit vectors of the Local Frame 1 defined in the world frame. It should be noted that these unit vectors may change depending on the axis of motion of the joint.

$${}^b \vec{x}_{21} = \hat{R}^{(b,2)} \cdot {}^2 \vec{x}_{21} \quad , \quad {}^b \vec{y}_{21} = \hat{R}^{(b,2)} \cdot {}^2 \vec{y}_{21} \quad (2.9)$$

This kinematic relation can be defined such that these two nodes make the same displacements in 5 DoF other than the last DoF, which is the rotation about the axis of motion of the first joint (Deblaise, Hernot, & Maurine, 2006). This relation can be given in the following matrix equation provided below.

$$\begin{bmatrix} \hat{I}_3 & \mathbf{0}_{3,3} & -\hat{I}_3 & \mathbf{0}_{3,3} \\ \mathbf{0}_{2,3} & \Omega_{21} & \mathbf{0}_{2,3} & -\Omega_{21} \end{bmatrix} \begin{bmatrix} dP_2 \\ \delta_2 \\ dP_1 \\ \delta_1 \end{bmatrix} = \begin{bmatrix} \mathbf{0}_{3,1} \\ \mathbf{0}_{2,1} \end{bmatrix} \quad (2.10)$$

where Ω_{21} is a 2x3 matrix having the unit vectors perpendicular to the axis of rotation of that revolute joint. These unit vectors are given in Equation 2.9 with ${}^b\bar{x}_{21}$ and ${}^b\bar{y}_{21}$ and they are defined with respect to the 1st frame. \hat{I} in Equation 2.10 stands for the 3x3 identity matrix and 0_{ij} stands for the ij dimensional zero matrix.

$$\Omega_{21} = \begin{bmatrix} {}^b\bar{x}_{21}^T \\ {}^b\bar{y}_{21}^T \end{bmatrix} \quad (2.11)$$

The Equation 2.10 can be represented with the following equation,

$$\begin{bmatrix} \hat{A}_{21} & -\hat{A}_{21} \end{bmatrix} \cdot \begin{bmatrix} \Delta\bar{X}_2 \\ \Delta\bar{X}_1 \end{bmatrix} = \begin{bmatrix} \bar{0}_{5,1} \end{bmatrix} \quad (2.12)$$

where \hat{A}_{21} , $\Delta\bar{X}_2$ and $\Delta\bar{X}_1$ are given as Equation 2.13.

$$\hat{A}_{21} = \begin{bmatrix} \hat{I}_3 & \hat{O}_3 \\ \hat{O}_{2,3} & \hat{\Omega}_{21} \end{bmatrix}; \quad \Delta\bar{X}_2 = \begin{bmatrix} d\bar{P}_2 \\ \bar{\delta}_2 \end{bmatrix}; \quad \Delta\bar{X}_1 = \begin{bmatrix} d\bar{P}_1 \\ \bar{\delta}_1 \end{bmatrix} \quad (2.13)$$

As shown in Equation 2.12, perfect revolute joints do not allow any linear displacements along \bar{x}_{21} , \bar{y}_{21} and \bar{z}_{21} and any angular displacements about \bar{x}_{21} and \bar{y}_{21} . General stiffness matrix \hat{K}_G , nodal force vector \bar{F}_G and nodal displacement vector $\Delta\bar{X}_G$ are defined in Equation 2.14.

$$\hat{K}_G = \begin{bmatrix} {}^b\hat{K}_T & \hat{A}^T \\ \hat{A} & \hat{O} \end{bmatrix}; \quad \bar{F}_G = \begin{bmatrix} \bar{F}_k \\ \bar{O} \end{bmatrix}; \quad \Delta\bar{X}_G = \begin{bmatrix} \Delta\bar{X}_k \\ \bar{\lambda} \end{bmatrix} \quad (2.14)$$

The A matrix is a (5m)x(6k) matrix where m is the number of joints and k is the number of the nodes defined for the serial chain. For a serial chain, \hat{A} matrix is constructed using Equation 2.12. In this matrix, nodes attached to each other on joints

have the kinematic constraints and the others that are not on the joints are represented with a zero matrix. The nodal force vector F_K is developed by carrying out static force analysis for each node. λ in Equation 2.14 is a 5x1 vector representing the Lagrange multiplier for the node. Considering the structure given in Figure 2.5, Equation 2.14 can be written such that $\bar{F}_G^T = [\bar{F}_1^T \quad \bar{F}_2^T \quad \bar{F}_3^T \quad \bar{0}_{1,6}]$ and $\Delta \bar{X}_G^T = [\Delta \bar{X}_1^T \quad \Delta \bar{X}_2^T \quad \Delta \bar{X}_3^T \quad \bar{\lambda}_{1,5}^T]$, for this system \hat{K}_G is written as:

$$\hat{K}_G = \begin{bmatrix} {}^b \hat{K}_{6,6}^1 & \hat{0}_{6,6} & \hat{0}_{6,6} & \hat{A}_{2,6}^T \\ \hat{0}_{6,6} & {}^b \hat{K}_{22}^2 & {}^b \hat{K}_{23}^2 & -\hat{A}_{2,3}^T \\ \hat{0}_{6,6} & {}^b \hat{K}_{32}^2 & {}^b \hat{K}_{33}^2 & \hat{0}_{6,5} \\ \hat{A}_{2,6} & -\hat{A}_{2,3} & \hat{0}_{5,6} & \hat{0}_{5,5} \end{bmatrix} \quad (2.15)$$

If the boundary conditions for the robot are defined perfectly, which means that robot is rigidly fixed to a stationary base, the deformations of nodes can be calculated by using Equation 2.16,

$$\Delta \bar{X}_G = \hat{K}_G^{-1} \cdot \bar{F}_G \quad (2.16)$$

In this set of linear equations \bar{X}_G , \bar{F}_G and \hat{K}_G will be subjected to simple permutation operations. The permutation of these vectors and matrices will give the same set of equations with a different alignment. The purpose of this operation is to separate the node of interest from the others, which will help us to find out an equivalent stiffness matrix for the robot structure. If we define a 3x3 permutation matrix of P composed of vectors $\varepsilon_1 = [1 \ 0 \ 0]$; $\varepsilon_2 = [0 \ 0 \ 1]$; $\varepsilon_3 = [0 \ 1 \ 0]$ and M composed of $M_1 = [a_{11} \ a_{12} \ a_{13}]$; $M_2 = [a_{21} \ a_{22} \ a_{23}]$; $M_3 = [a_{31} \ a_{32} \ a_{33}]$ such that, $P^T = [\varepsilon_1 \ \varepsilon_2 \ \varepsilon_3]$ and $M^T = [M_1 \ M_2 \ M_3]$, then the matrix multiplication of P by a 3x3 matrix of M from left will give the matrix M_L with rows interchanged according to the permutation vector, which can be shown as;

$$P \cdot M = M_L; \quad \begin{bmatrix} 1 & 0 & 0 \\ 0 & 0 & 1 \\ 0 & 1 & 0 \end{bmatrix} \cdot \begin{bmatrix} a_{11} & a_{12} & a_{13} \\ a_{21} & a_{22} & a_{23} \\ a_{31} & a_{32} & a_{33} \end{bmatrix} = \begin{bmatrix} a_{11} & a_{12} & a_{13} \\ a_{31} & a_{32} & a_{33} \\ a_{21} & a_{22} & a_{23} \end{bmatrix} \quad (2.17)$$

If the inverse of P matrix, which comes out to be itself, were multiplied from right, the resultant matrix M_R would be the M matrix with the columns interchanged according to the permutation vectors (Stuart & Weaver, 1991) as shown in Equation 2.18.

$$M \cdot P^{-1} = M_R; \quad \begin{bmatrix} a_{11} & a_{12} & a_{13} \\ a_{21} & a_{22} & a_{23} \\ a_{31} & a_{32} & a_{33} \end{bmatrix} \cdot \begin{bmatrix} 1 & 0 & 0 \\ 0 & 0 & 1 \\ 0 & 1 & 0 \end{bmatrix} = \begin{bmatrix} a_{11} & a_{13} & a_{21} \\ a_{21} & a_{23} & a_{22} \\ a_{31} & a_{33} & a_{23} \end{bmatrix} \quad (2.18)$$

ΔX_P , F_P and K_P , given in Equation 2.19, are the permutations of \bar{X}_G , \bar{F}_G and \hat{K}_G and they provide a simple solution in finding the equivalent stiffness matrix of a structure, which is defined for a specified node.

$$\hat{K}_P = \hat{P} \cdot \begin{bmatrix} {}^b \hat{K}_T & \hat{A}^T \\ \hat{A} & 0 \end{bmatrix} \cdot \hat{P}^{-1}; \quad \bar{F}_P = \hat{P} \cdot \begin{bmatrix} \bar{F}_G \\ 0 \end{bmatrix}; \quad \Delta \bar{X}_P = \hat{P} \cdot \begin{bmatrix} \Delta \bar{X}_G \\ \bar{\lambda} \end{bmatrix} \quad (2.19)$$

When the permutations of \bar{X}_G , \bar{F}_G and \hat{K}_G are found according to the method previously described, these vectors and matrices become:

$$\Delta \bar{X}_P = \begin{bmatrix} \Delta \bar{X}_1 \\ \Delta \bar{X}_2 \\ \bar{\lambda} \\ \Delta \bar{X}_3 \end{bmatrix}, \quad \bar{F}_P = \begin{bmatrix} \bar{F}_1 \\ \bar{F}_2 \\ \bar{0}_{6,1} \\ \bar{F}_3 \end{bmatrix}, \quad \hat{K}_P = \begin{bmatrix} {}^b \hat{K}_{6,6}^1 & \hat{0}_{6,6} & \hat{A}_{21}^T & \hat{0}_{6,6} \\ \hat{0}_{6,6} & {}^b \hat{K}_{22}^2 & -\hat{A}_{21}^T & {}^b \hat{K}_{23}^2 \\ \hat{A}_{21} & -\hat{A}_{21} & \hat{0}_{5,5} & \hat{0}_{5,6} \\ \hat{0}_{6,6} & {}^b \hat{K}_{32}^2 & \hat{0}_{5,6} & {}^b \hat{K}_{33}^2 \end{bmatrix} \quad (2.20)$$

For the ease of calculation, Equation 2.20 can be divided into a block representation so that the node of interest is isolated from the other terms as presented in Equation 2.21. In this block representation, $\Delta \bar{X}_R$ and \bar{F}_R represent the rest of the elements

of $\Delta\bar{X}_p$ and \bar{F}_p other than $\Delta\bar{X}_3$ and F_3 . \hat{K}_p in Equation 2.20 is represented by the elements K_{R1} , K_{R2} , K_{R3} and ${}^bK_{33}^2$ in Equation 2.21.

$$\Delta\bar{X}_p = \begin{bmatrix} \Delta\bar{X}_R \\ \Delta\bar{X}_3 \end{bmatrix}, \quad \bar{F}_p = \begin{bmatrix} \bar{F}_R \\ \bar{F}_3 \end{bmatrix}, \quad \hat{K}_p = \begin{bmatrix} \hat{K}_{R1} & \hat{K}_{R2} \\ \hat{K}_{R3} & {}^b\hat{K}_{33}^2 \end{bmatrix} \quad (2.21)$$

As described in (Deblaise, Hernot, & Maurine, 2006), if a linear equation set is written and expanded in the form of $\hat{K}_p \cdot \Delta\bar{X}_p = \bar{F}_p$, following equations are formulated:

$$\hat{K}_{R1} \cdot \Delta\bar{X}_R + \hat{K}_{R2} \cdot \Delta\bar{X}_3 = \bar{F}_R \quad (2.22)$$

$$\hat{K}_{R3} \cdot \Delta\bar{X}_R + {}^b\hat{K}_{33}^2 \cdot \Delta\bar{X}_3 = \bar{F}_3 \quad (2.23)$$

If $\Delta\bar{X}_R$ is left alone in Equation 2.22 and then substituted into Equation 2.23, the final expression provided in Equation 2.24 gives the compliant displacement of node 3 with an equivalent stiffness matrix and force.

$$\Delta\bar{X}_3 = (-\hat{K}_{R3} \cdot \hat{K}_{R1}^{-1} \cdot \hat{K}_{R2} + {}^b\hat{K}_{33}^2)^{-1} \cdot (\bar{F}_3 - \hat{K}_{R3} \cdot \hat{K}_{R1}^{-1} \cdot \bar{F}_R) \quad (2.24)$$

Equivalent stiffness matrix \bar{K}_E and equivalent force \bar{F}_E that are implicitly written in Equation 2.24 are presented explicitly in Equation 2.25. This equivalent representation for stiffness calculations for the single DoF mechanism of concern is illustrated in Figure 2.7.

$$\begin{aligned} \hat{K}_E &= (-\hat{K}_{R3} \cdot \hat{K}_{R1}^{-1} \cdot \hat{K}_{R2} + {}^b\hat{K}_{33}^2) \\ \bar{F}_E &= (\bar{F}_3 - \hat{K}_{R3} \cdot \hat{K}_{R1}^{-1} \cdot \bar{F}_R) \end{aligned} \quad (2.25)$$

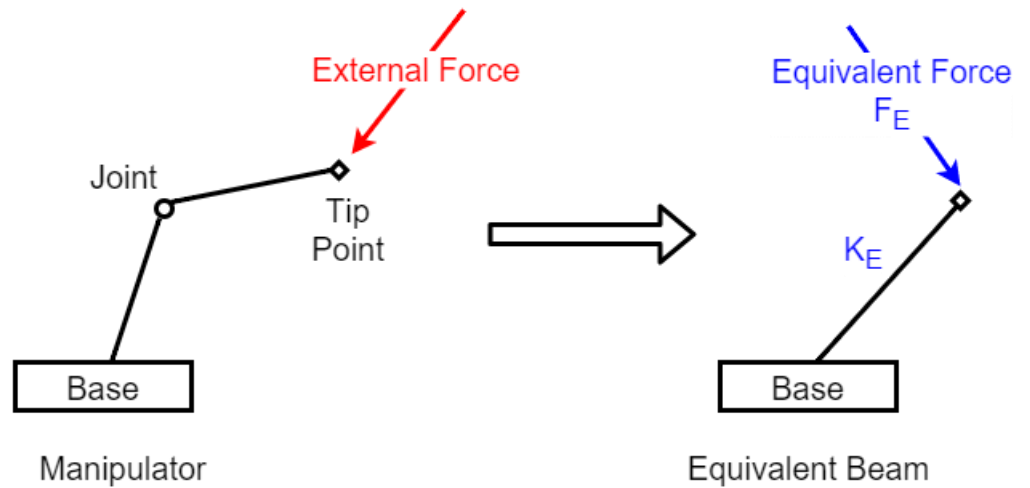


Figure 2.7 Equivalent beam representing the manipulator for stiffness calculations

Once the equivalent stiffness matrix for a serial chain of a parallel mechanism is calculated, it can be combined with the rest of serial chains' stiffness matrices for finding the equivalent stiffness matrix and equivalent force vector for the parallel mechanism as explained in (Deblaise, Hernot, & Maurine, 2006). The method of combining the equivalent stiffness matrices of serial chains for a parallel robot relies on a kinematic constraint defined for the mobile platform of the parallel robot. This kinematic constraint states that, if any two nodes are defined on a rigid body, the compliant displacements between them is zero, which is expressed by Equation 2.26. Therefore, the vector \vec{L}_{vw} , which is shown in Figure 2.8, defines the relative position of the nodes and it is constant.



Figure 2.8 A rigid body defined by nodes v and w . The displacements of these nodes are given with dP_v , δ_v , dP_w and δ_w .

$$\begin{aligned}\delta_v &= \delta_w \\ \mathbf{P}_v &= \mathbf{P}_w + \tilde{\mathbf{L}}_{vw} \cdot \delta_w\end{aligned}\quad (2.26)$$

This kinematic relation ensures that there is no energy stored in the rigid body.

$$\begin{bmatrix} \hat{\mathbf{0}}_{3,3} & -\hat{\mathbf{I}}_3 & \hat{\mathbf{0}}_{3,3} & \hat{\mathbf{I}}_3 \\ -\hat{\mathbf{I}}_3 & \hat{\mathbf{0}}_{3,3} & \hat{\mathbf{I}}_3 & \tilde{\mathbf{L}}_{vw} \end{bmatrix} \cdot \begin{bmatrix} \bar{\mathbf{P}}_v \\ \bar{\delta}_v \\ \bar{\mathbf{P}}_w \\ \bar{\delta}_w \end{bmatrix} = \begin{bmatrix} \bar{\mathbf{0}}_{3,1} \\ \bar{\mathbf{0}}_{3,1} \end{bmatrix}\quad (2.27)$$

$\tilde{\mathbf{L}}_{vw}$ is a skew symmetric matrix of $\vec{\mathbf{L}}_{vw} = [\mathbf{L}_x \ \mathbf{L}_y \ \mathbf{L}_z]^T$, which is a vector defined from node v to node w.

$$\tilde{\mathbf{L}}_{vw} = \begin{bmatrix} 0 & -\mathbf{L}_z & \mathbf{L}_y \\ \mathbf{L}_z & 0 & -\mathbf{L}_x \\ -\mathbf{L}_y & \mathbf{L}_x & 0 \end{bmatrix}\quad (2.28)$$

Thus the simplified form of Equation 2.27 can be written as:

$$\begin{bmatrix} \hat{\mathbf{B}} & \hat{\mathbf{B}}_{vw} \end{bmatrix} \cdot \begin{bmatrix} \Delta \bar{\mathbf{X}}_v \\ \Delta \bar{\mathbf{X}}_w \end{bmatrix} = \begin{bmatrix} \bar{\mathbf{0}}_{6,1} \end{bmatrix}\quad (2.29)$$

$\hat{\mathbf{B}}$, $\hat{\mathbf{B}}_{vw}$ in Equation 2.29 are written as:

$$\hat{\mathbf{B}} = \begin{bmatrix} \hat{\mathbf{0}}_3 & -\hat{\mathbf{I}}_3 \\ -\hat{\mathbf{I}}_3 & \hat{\mathbf{0}}_3 \end{bmatrix}, \quad \hat{\mathbf{B}}_{vw} \hat{=} \begin{bmatrix} \mathbf{0}_3 & \hat{\mathbf{I}}_3 \\ \hat{\mathbf{I}}_3 & \tilde{\mathbf{L}}_{vw} \end{bmatrix}\quad (2.30)$$

Equivalent stiffness matrix of the parallel kinematic robot can be obtained using the kinematic relation given in Equation 2.29. The analogy remains same for implementing these kinematic relations and given by Equation 2.20.

2.3.2. Finite Element Analysis in Stiffness Modeling

Analytical methods for the stiffness calculations of the robots generally produce complex closed form analytical expressions which are hard to solve (Pêgo et al., 2013). Generally in analytical methods, links having complex shapes are simplified and joints are considered to be rigid, which means that material properties of the joints do not affect the overall displacement of the robot but they are only used in defining kinematic relations. Such approximations reduce the accuracy of the robot's stiffness model that is less useful in design improvement stage of the robot manipulator as discussed in (Aginagaa et al., 2012) and (Deblaise, Hernot, & Maurine, 2006).

In order to overcome this inaccuracy in analytical methods, robot's stiffness model can be constructed by FEA. This method reduces infinite dimensional robot model into finite dimension and these finite regions are called as elements. Then these elements are given a certain number of nodes depending on their geometry such as, cube and pyramid. Then the approximate solutions of an element are calculated among these nodes. These solutions are approximated, so that they guarantee a continuous solution for the nodes shared by the neighbor elements (Logan, 2011).

FEA shares the same basis with the SMA; however, it reduces the element size from links and joints to finite sized geometric shapes of cubes and pyramids. By this way more accurate geometries of the links, joints and end-effector can be modeled (Klimchik, 2011). This property of FEA makes it far more accurate compared to the SMA, since the links and joints can be modeled in their original shape and the node of interest can be extracted from the others just as described in SMA (Huang, Zhao & Whitehouse, 2002). However, increased number of nodes generates larger matrices to be dealt with, which

requires higher computational cost. Due to this higher computational cost, this method is generally preferred to be used in the final stage of the design procedure (Carbone, 2003).

2.3.3. Virtual Joint Method in Stiffness Modeling

VJM assumes that the links of a robot manipulator are rigid and compliances of the links are represented with localized springs placed in the joints. These auxiliary joints are called virtual joints and they lump the compliances of links and joints onto one point. Due to this approach, this method is also called as lumped method (Gosselin, 1990). For the structure having compliant joints and rigid links, static equilibrium equations are derived and linearized to obtain Cartesian stiffness matrix of the manipulator as explained in (Zhang & Gosselin, 2002). In this work, joints were assumed to be the dominating source of compliance and as an application of the method, stiffness of a serial manipulator was derived. In the works (Zhang & Gosselin, 2002), (Xi et al., 2004) and (Majou et al., 2007), the compliances of the links were also lumped in the virtual joints and VJM were applied on parallel mechanisms. Since the links' and joints' stiffness are lumped on a joint and the rigid body assumption is made in calculations of end-effector positions, this method simplifies the stiffness calculation (Klimchik, 2011).

When this method was first applied by (Gosselin, 1990), the compliant elements were defined by only one degree of freedom springs. This approach was not capable of representing a general stiffness matrix for the links and thus, for the whole manipulator. To improve its accuracy, several virtual joints were used to represent the translational and rotational degrees of freedoms (Majou, 2007). In this work, compliances of the links were calculated by considering the links as flexible beams and stiffness values for these links were derived by relating the external forces to the displacement (Majou et al., 2007). Finally, in the work of (Pashkevich, Chablat & Wenger, 2008) the compliances of the links are obtained using a FEA-based approach. In this approach, links are modeled in a 3D CAD environment and imported into FEA software. By using FEA tools, a 6x6 symmetrical semi-definite, non-negative stiffness matrices is obtained for each link after several numerical simulations. As a result of this, stiffness parameters of the links and joints are calculated more accurately with the help of FEA. Although this process requires

more computational time for finding a link stiffness, it is executed once for a design. That is the reason that this method can be used in VJM calculations and can be used in closed-form analytical solutions.

Stiffness calculations in VJM originate from the basic equations given below. Equation 2.31 is derived from the geometric model of the manipulator and it relates the translational and rotational displacements of virtual joints to the end-effector's compliant displacement. In Equation 2.32, static equilibrium of the manipulator is given and finally in Equation 2.33, the changes in virtual joints are related to the reaction forcing by Hooke's Law (Gosselin, 1990).

$$\delta t = J_{\theta} \cdot \delta \theta \quad (2.31)$$

$$\tau = J_{\theta}^T \cdot F \quad (2.32)$$

$$\tau = K_{\theta} \cdot \delta \theta \quad (2.33)$$

In Equation 2.31, δt vector includes the translational and rotational compliant displacements of the end-effector, J_{θ} is the Jacobian matrix and δ_{θ} is the translational and rotational displacements of virtual joints. In 2.32, τ stands for the vector of reactions in the virtual joints, F stands for the vector of external forces and moments. Finally, K_{θ} contains the stiffness information of the virtual joints. After some symbolic manipulations Equations, 2.31, 2.32 and 2.33 can be combined in one equation presented in 2.34. In Equation 2.34, Cartesian stiffness matrix is given as $K_C = J_{\theta} \cdot K_{\theta}^{-1} \cdot J_{\theta}^T$ in unloaded mode, where the external load is relatively small. The reason to specify the external load as small is that the calculations include kinematic relations which would change if there is relatively large amount of force which causes change in the configuration of the robot. Therefore, this stiffness matrix calculations holds only in the vicinity of the initial condition where the external forcing is relatively small.

$$\delta t = (J_0 \cdot K_0^{-1} \cdot J_0^T) \cdot \delta \theta \quad (2.34)$$

It is obvious in Equation 2.34 that the important issue for this approach is finding the stiffness matrix K_0 for the virtual joints. In the first studies for VJM, this matrix was developed in a way that the compliancy due to forces and moments are considered to be decoupled (Gosselin, 2002). This resulted in a diagonal 6 by 6 matrix. In the following works, the stiffness matrix definition is improved by including the coupling of the deflections due to the forces and moments (Li, 2008).

When this method is first applied to parallel mechanisms, some assumptions were made. In these assumptions, parallel robots were not considered as over-constraint mechanisms and compliances of the manipulator was concentrated in the actuated joint (Gosselin, 1990). Then in following works by (Zhang, 2002) and (Xi et al., 2004), VJM is extended to links' and passive joints' compliances. Recently, in the works of (Pashkevich, Chablat & Wenger, 2008) and (Pashkevich, Chablat & Wenger, 2009), stiffness values of the links are obtained via numerical simulations.

Generally, each serial chain of a parallel robot includes an active joint and passive joints. Therefore, in stiffness calculations passive joint effects are considered. As denoted in (Klimchik, 2011), passive joints can be eliminated when the geometric constraints imposed by the manipulator assembly are not redundant. In this case, the original formulation provided in Equation 2.34 can be applied. However, in the case of over-constrained and under-constrained mechanisms the elimination of passive joints cannot be applied directly. This problem is studied by (Majou et al., 2007) and (Pashkevich, Chablat & Wenger, 2008), in which internal loops like parallelograms in a serial chain is converted to an equivalent serial link. The technique proposed in (Pashkevich, Chablat & Wenger, 2008) requires inversion of a square matrix of size $(6 + n_0) \times (6 + n_0)$ where n_0 is the number of passive joints. This square matrix is composed of link stiffness matrices and Jacobian matrices of both virtual springs and passive joints. When the inverse of this matrix is taken, Cartesian stiffness K_C matrix can be extracted from this matrix which is provided in Equation 2.35.

$$\begin{bmatrix} \mathbf{K}_c & * \\ * & * \end{bmatrix} = \begin{bmatrix} \mathbf{J}_\theta \cdot \mathbf{K}_\theta^{-1} \cdot \mathbf{J}_\theta^T & \mathbf{J}_q \\ \mathbf{J}_q^T & \mathbf{0} \end{bmatrix}^{-1} \quad (2.35)$$

\mathbf{J}_θ is the Jacobian matrix formulated for the virtual springs and \mathbf{J}_q is the Jacobian matrix formulated for the passive joints. Once the stiffness matrices of serial chains that connect the base and the moving platform of a parallel manipulator are calculated, they can be integrated into a general stiffness model under some assumptions. These assumptions are that there should be no internal loops in the serial chain and serial chains connect to the same point on the moving platform (Xi, 2004). The method for combining the legs that is not connected to the same point is provided in (Klimchik, 2011). When these conditions are met, stiffness matrices of serial chains of a parallel manipulator can be superposed directly as given in Equation 2.36.

$$\begin{bmatrix} \mathbf{K}_c & * \\ * & * \end{bmatrix} = \begin{bmatrix} \mathbf{J}_\theta \cdot \mathbf{K}_\theta^{-1} \cdot \mathbf{J}_\theta^T & \mathbf{J}_q \\ \mathbf{J}_q^T & \mathbf{0} \end{bmatrix}^{-1} \quad (2.36)$$

where i is the kinematic chains and n is the number of chains (Pashkevich, Chablat & Wenger, 2009).

Compared to the other methods, VJM has low computational cost due to the simplicity in modeling of the compliance model of the robot manipulator. With the proposed method of finding virtual spring parameters by FEA, VJM method proved to be comparable with FEA method in terms of accuracy (Klimchik, 2011).

2.3.4. Matrix Product Method

Matrix product method is proposed by (Ceccarelli & Carbone, 2002), which simply decomposes the stiffness behavior of the parallel robot into its force transmission, stiffness values of leg components, leg geometry and leg configuration. The parallel robot, which is given in Figure 2.9, is under the effect of an external wrench \mathbf{W} and this

results in the compliant displacement of the end-effector by ΔS . Here these parameters are given as $\bar{W}=(F_x,F_y,F_z,T_x,T_y,T_z)^T$ and $\Delta\bar{S}=(U_x,U_y,U_z,U_\alpha,U_\gamma,U_\delta)^T$.

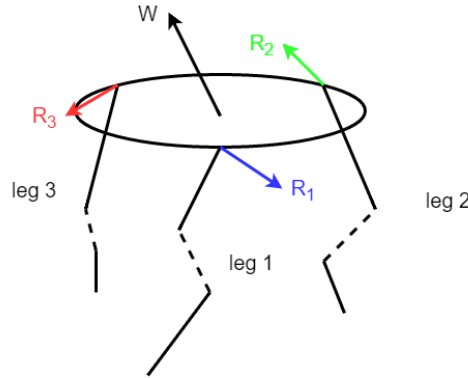


Figure 2.9 Forcing on legs of parallel robot under an external forcing

The method is performed by finding a relation between external wrench W and the reaction forcings R_1 , R_2 and R_3 that are applied on the end-effector of a robot from the leg 1, 2 and 3. For the parallel robot scenario as given in (Ceccarelli & Carbone, 2002), the force transmission matrix, T , is an $n \times m$, non-diagonal matrix. Here the n is the number of external wrench components, which is 6 for the general case, and m is the total number of reaction forcing components. Therefore, if reaction forcings R_1 , R_2 and R_3 have the all the force and moment components in x , y and z directions, then m becomes 18. The relation between W and the reaction forcings is given in Equation 2.37.

$$W=T \cdot R \quad (2.37)$$

Then, these reaction forcing vector is related to the individual displacements of the compliant elements of the mechanism, which are the links, joints and actuators in each leg of the parallel robot. Therefore, the relation is set by the stiffness values of the compliant elements and this is provided in Equation 2.38.

$$R=K \cdot \Delta l \quad (2.38)$$

Here the stiffness matrix K is defined according to the reference frame and includes stiffness values of all three legs for the case presented in Figure 2.9. In addition,

Δl is composed of Δl_1 , Δl_2 and Δl_3 each has linear and rotational displacements in x, y and z directions.

$$\hat{K} = \begin{bmatrix} K_1 & 0 & 0 \\ 0 & K_2 & 0 \\ 0 & 0 & K_3 \end{bmatrix}_{(18 \times 18)} \quad (2.39)$$

$$\Delta l = [\Delta l_1 \quad \Delta l_2 \quad \Delta l_3]_{(1 \times 18)}^T \quad (2.40)$$

Once the stiffness reaction forcing vector R is related to the leg displacements Δl , the coordinate variation at the joint, which connects the leg the end-effector, can be found. This variation can be positional and/or rotational difference and it is represented for the case presented in Figure 2.9 which has three legs as $e = [e_1 \quad e_2 \quad e_3]^T$, where $e_k = [x_k \quad y_k \quad z_k \quad \theta_{x_k} \quad \theta_{y_k} \quad \theta_{z_k}]^T$ is the coordinate variation of leg k . The relation between coordinate variation and the leg deformations are defined with C which is given in 2.41.

$$\Delta l = C^{-1} \cdot e \quad (2.41)$$

After coordinate variations of the joints that are between the legs and the end-effector are calculated, the pose of the end-effector is found by applying a geometric relation. This is done by finding parametric plane equations A that is a function of the coordinate variations e , which is given in 2.51.

$$e = A^{-1} \cdot \Delta S \quad (2.42)$$

After these steps are finished, then these matrices can be combined together to form the matrix product method as presented in 0.43. The total stiffness matrix of parallel robot K_{TOTAL} is then formulated as shown in 0.44.

$$W = M \cdot K \cdot C^{-1} \cdot A^{-1} \cdot \Delta S \quad (2.43)$$

$$K_{TOTAL} = M \cdot K \cdot C^{-1} \cdot A^{-1} \quad (2.44)$$

2.3.5. Identification of Link Stiffness Matrices

The stiffness matrices for links are generally determined by approximating the links as simple beams and this method is named as single beam approximation. In the literature, this method appears to be the most used one. Stiffness of a link can be easily determined by relating the forcing \vec{F} acting on the link and translational and rotational deformations of the link (Yoon et al., 2004). For example considering a load F on a beam, the deflection of the link $\Delta\vec{S}$ is shown in Figure 2.10.

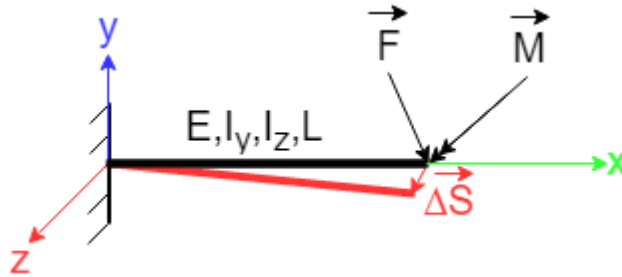


Figure 2.10 A slender beam fixed from one end and subjected to a force from the other end. \vec{F} , \vec{M} and $\Delta\vec{S}$ are 3×1 , 3×1 and 6×1 vectors defining the force, moment and deflection of the beam.

For example, considering the force vector to be in x-direction only and moments to be zero, deflection of the beam can be found by applying following equation. In Equation 2.46, \vec{F} and $\Delta\vec{S}$ is related with a constant value that is the stiffness of the beam in x direction.

$$\Delta x = \frac{F_x \cdot L}{A \cdot E} \quad (2.45)$$

$$\Delta x \cdot \frac{A \cdot E}{L} = F_x \quad (2.46)$$

With this analogy the other stiffness elements can be written as provided in Equation 2.47 (Przemieniecki, 1985).

$$\hat{\mathbf{K}} = \begin{bmatrix} \frac{EA}{L} & 0 & 0 & 0 & 0 & 0 \\ 0 & \frac{12EI_z}{L^3} & 0 & 0 & 0 & \frac{-6EI_z}{L^2} \\ 0 & 0 & \frac{12EI_y}{L^3} & 0 & \frac{6EI_y}{L^2} & 0 \\ 0 & 0 & 0 & \frac{GJ}{L} & 0 & 0 \\ 0 & 0 & \frac{6EI_y}{L^2} & 0 & \frac{4EI_y}{L} & 0 \\ 0 & \frac{-6EI_y}{L^2} & 0 & 0 & 0 & \frac{4EI_y}{L} \end{bmatrix} \quad (2.47)$$

However, for the links having complex shapes, determination of link stiffness can be made by multi-beam approximation (Klimcik, 2011). In this approximation, link is divided into several pieces of serial links connected rigidly, which have simple geometric shapes. The stiffness matrices of these smaller links can then be combined by any stiffness matrix calculation method that is presented in this thesis. Schematic representation of this method is illustrated on a link that is given in Figure 2.11. Link shown in Figure 2.11 has varying cross-sectional areas along its length and it is not a straight beam. Provided in the figure, this link is divided into simpler pieces that are link1, link2, link3 and link 4 respectively. To model this complex link more accurately, stiffness properties of these simpler links are calculated first and then integrated to each other in the right sequence. The integration can be done with SMA or VJM depending on the preferred method used for the analysis of whole system. Considering the stiffness analysis of a robot that contains this complex link provided in Figure 2.11, is executed with SMA, then the links 1 to 4

can be integrated to each other with SMA. In this case, the procedure of integration is provided by Equation 2.52.

Symbolically, links 1, 2, 3 and 4 has stiffness matrices given in Equations 2.48, 49, 50 and 51. Subscripts written in these equations are giving identification of the nodes to the related links respectively. Therefore, they are provided in the equations by the numbers 1 and 2. It should also be noted that stiffness matrices are rotated according to the rotation of these links with respect to the world coordinate.

$${}^b \mathbf{K}^{\text{link1}} = \begin{bmatrix} {}^b \mathbf{K}_{11}^{\text{link1}} & {}^b \mathbf{K}_{12}^{\text{link1}} \\ {}^b \mathbf{K}_{21}^{\text{link1}} & {}^b \mathbf{K}_{22}^{\text{link1}} \end{bmatrix} \quad (2.48)$$

$${}^b \mathbf{K}^{\text{link2}} = \begin{bmatrix} {}^b \mathbf{K}_{11}^{\text{link2}} & {}^b \mathbf{K}_{12}^{\text{link2}} \\ {}^b \mathbf{K}_{21}^{\text{link2}} & {}^b \mathbf{K}_{22}^{\text{link2}} \end{bmatrix} \quad (2.49)$$

$${}^b \mathbf{K}^{\text{link3}} = \begin{bmatrix} {}^b \mathbf{K}_{11}^{\text{link3}} & {}^b \mathbf{K}_{12}^{\text{link3}} \\ {}^b \mathbf{K}_{21}^{\text{link3}} & {}^b \mathbf{K}_{22}^{\text{link3}} \end{bmatrix} \quad (2.50)$$

$${}^b \mathbf{K}^{\text{link4}} = \begin{bmatrix} {}^b \mathbf{K}_{11}^{\text{link4}} & {}^b \mathbf{K}_{12}^{\text{link4}} \\ {}^b \mathbf{K}_{21}^{\text{link4}} & {}^b \mathbf{K}_{22}^{\text{link4}} \end{bmatrix} \quad (2.51)$$

Once the stiffness matrices of the links are calculated, they are integrated with the exact method provided for whole robotic structure.

$${}^b \mathbf{K}^{\text{TOTAL}} = \begin{bmatrix} {}^b \mathbf{K}_{11}^{\text{link1}} & {}^b \mathbf{K}_{12}^{\text{link1}} & 0_{6,6} & 0_{6,6} & 0_{6,6} \\ {}^b \mathbf{K}_{21}^{\text{link1}} & {}^b \mathbf{K}_{22}^{\text{link1}} + {}^b \mathbf{K}_{11}^{\text{link2}} & {}^b \mathbf{K}_{12}^{\text{link2}} & 0_{6,6} & 0_{6,6} \\ 0_{6,6} & {}^b \mathbf{K}_{21}^{\text{link2}} & {}^b \mathbf{K}_{22}^{\text{link2}} + {}^b \mathbf{K}_{11}^{\text{link3}} & {}^b \mathbf{K}_{12}^{\text{link3}} & 0_{6,6} \\ 0_{6,6} & 0_{6,6} & {}^b \mathbf{K}_{21}^{\text{link3}} & {}^b \mathbf{K}_{22}^{\text{link3}} + {}^b \mathbf{K}_{11}^{\text{link4}} & {}^b \mathbf{K}_{12}^{\text{link4}} \\ 0_{6,6} & 0_{6,6} & 0_{6,6} & {}^b \mathbf{K}_{21}^{\text{link4}} & {}^b \mathbf{K}_{22}^{\text{link4}} \end{bmatrix} \quad (2.52)$$

In the case of VJM, the procedure of integration can be done by generating the Denavit-Hartenberg (D-H) parameters of the complex link as if it is a mechanism. For

example, a simple beam can be modelled with six virtual joints that have virtual joint parameters of S_{1i} , S_{2i} , S_{3i} , θ_{1i} , θ_{2i} , θ_{3i} . The subscript i represents the identification number of the link.

Table 2.1 Denavit-Hartenberg parameters of links 1, 2, 3 and 4 to be combined in multi-beam approximation of the complex beam.

	d	θ	a	α
1	$S1+L_i$	$\pi/2$	0	$\pi/2$
2	$S2$	$\pi/2$	0	$\pi/2$
3	$S3$	$\pi/2$	0	$\pi/2$
4	0	θ_1	0	$\pi/2$
5	0	θ_2	0	$\pi/2$
6	0	θ_3	0	$\pi/2$
7	0	β_i	0	$-\pi/2$

L and β are the length and angular displacement between links. β is defined from the previous to the next link and it is a constant. After putting D-H parameters of all links one after another in the required sequence, the orientation matrix and position vector can be calculated and from this knowledge Jacobian Matrix of the link can be computed. When the Jacobian and stiffness parameters of the link is set into the Equation 2.36, the stiffness matrix of the complex link can be found.

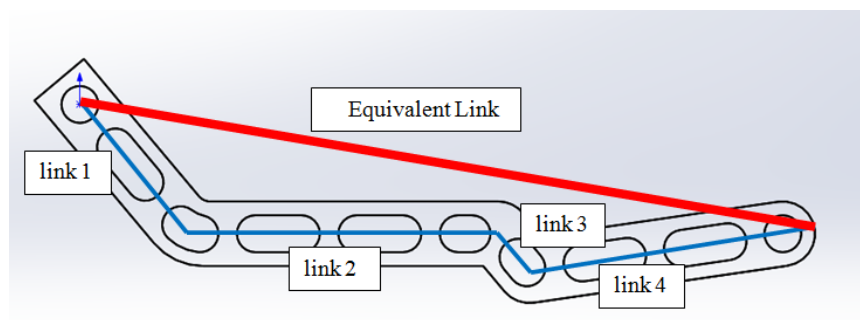


Figure 2.11 Link collecting the stiffness properties of the links in the serial chain

Although the method of dividing a complex link into smaller pieces provides better results and it is computationally more convenient, practically it does not provide accurate results to most of the robots which have non-uniform cross sections in their links (Klimchik, 2011). An example for such links can be the one in Figure 2.11. The circular cavities that are cut out of the link for reducing the weight, makes the analysis of the stiffness properties harder.

To achieve better accuracy in determining the stiffness of links, another method is proposed by (Paskevich et al., 2010). In this method, links are modeled in a CAD environment and then exported to an FEA software. In this software, the mechanical properties of the links are selected and proper fixtures are defined to one end of the link to construct a cantilever beam approach. Forces and torques are applied systematically to the other end of the link and deflection field of the free end of the link is measured. This deflection field is the compliant displacements of the reference point's neighborhood. Then FEA simulations are repeated for forces and moments in different directions. Finally, link's stiffness model identification is done according to the data of deflections and applied forcings.

For small deformations, the stiffness properties are defined through stiffness matrix K , which defines the linear relation

$$\begin{bmatrix} F \\ M \end{bmatrix} = K \cdot \begin{bmatrix} p \\ \psi \end{bmatrix} \quad (2.53)$$

where p and ψ are the translational and rotational displacement vectors of the free end and F and M are the force and moment vectors causing these displacements.

After carrying out simulations for different forces and moments, link's stiffness matrix can be computed from the linear system provided in Equation 2.54.

$$k = \begin{bmatrix} F_1 & \dots & F_m \\ M_1 & \dots & M_m \end{bmatrix}^{-1} \cdot \begin{bmatrix} P_1 & \dots & P_m \\ \Psi_1 & \dots & \Psi_m \end{bmatrix} \quad (2.54)$$

where k is the inverse of the stiffness matrix of the link, K and m is the number of experiments (Pashkevich, 2010). In each experiment only one force or moment is applied on the link, given in equation 2.55, therefore, in each test one column of stiffness matrix will be computed.

$$\begin{aligned} F_1 &= (F_x, 0, 0)^T & M_1 &= (0, 0, 0)^T; & F_4 &= (0, 0, 0)^T & M_4 &= (M_x, 0, 0)^T; \\ F_2 &= (0, F_y, 0)^T & M_2 &= (0, 0, 0)^T; & F_5 &= (0, 0, 0)^T & M_5 &= (0, M_y, 0)^T; \\ F_3 &= (0, 0, F_z)^T & M_3 &= (0, 0, 0)^T; & F_6 &= (0, 0, 0)^T & M_6 &= (0, 0, M_z)^T; \end{aligned} \quad (2.55)$$

Finally, after 6 experiments the stiffness matrix for the link is computed as,

$$K = \begin{bmatrix} p_1/F_x & p_2/F_y & p_3/F_z & p_4/M_x & p_5/M_y & p_6/M_z \\ \psi_1/F_x & \psi_2/F_y & \psi_3/F_z & \psi_4/M_x & \psi_5/M_y & \psi_6/M_z \end{bmatrix}^{-1} \quad (2.56)$$

Since there is a statistical approach by evaluating the deflections for various forcings and the link shapes, coupling between rotational and translational deflections and joint particularities are taken into the account, this method provides a reduction of errors in the calculation of a link's stiffness matrix from 20-50 % to 0.1%. These error reduction values are taken from the works of (Klimchik, 2011) and (Pashkevich, Chablat & Wenger, 2009).

2.3.6. Experimental Methods

In calculation of stiffness matrix of robots, previously described methods provide solutions, which are more accurate like FEA solutions or computationally effective that can be used in on-line calculations. Although, the difference between the analytical and experimental solutions are getting closer with the improvements in the analytical models, there is still a remarkable error between these solutions for high precision applications

(Carbone, 2011). To identify the deviation of the stiffness model from the real case experiments are executed. These experiments share the same methodology that is to measure the displacement of the robot's end-effector under external wrenches. In literature, researchers have measured the end-effector displacements with various absolute measurement devices for example, (Clinton, Zhang, & Wavering, 1997) used dual indicators in measurement and followed the test procedure outlined in ASME Standard B5.54 (1993) that is given in the Figure 2.12.

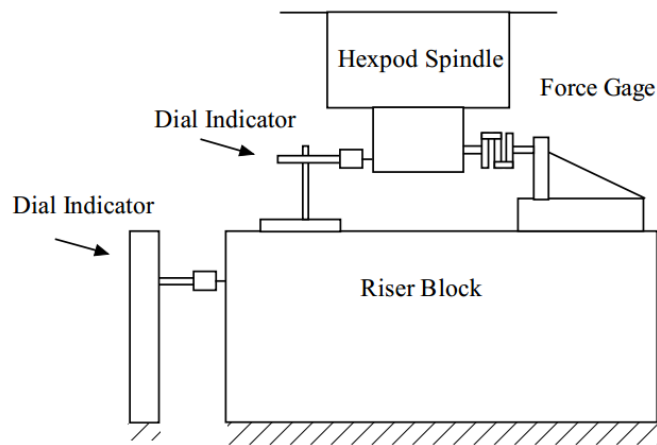


Figure 2.12 Test setup for stiffness matrix evaluation (Clinton, Zhang & Wavering, 1997).

Another study (Alicı & Shirinzadeh, 2005) made use of laser tracker for measuring the displacement of a serial robot at heuristically determined points in its workspace. In this experiment force is applied through a wire on the end-effector and resultant forces in three axis is found through a force sensor. A schematic for experimental method is given in Figure 2.13.

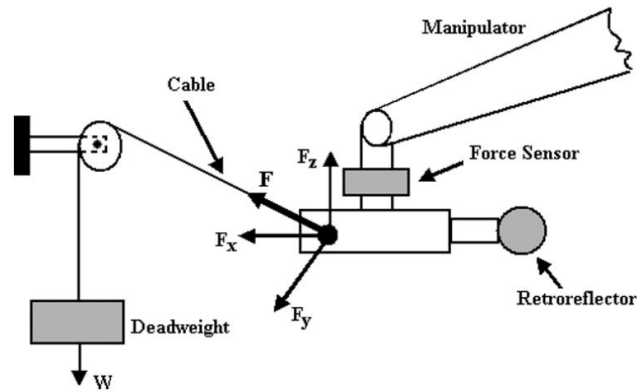


Figure 2.13 Schematic for Stiffness measurement. The measurement is made by measuring the retroreflector with a laser tracker (Alic1 & Shirinzadeh, 2005).

Previously provided strategies were executed with complex testing procedures with expensive measurement devices. Therefore, mapping the stiffness characteristics of manipulators are limited (Carbone, 2011). In the work of (Pinto, Corral, Altuzarra & Hernández, 2010), a measurement cycle is provided for compliance measurements and this cycle defines a 5 step testing procedure. The procedure starts by dividing the workspace into points, where the stiffness measurements is executed. Secondly, the localization of the joints has to be done either by control or by manually with some fixtures. This step is followed by the 3rd phase that is the preload phase. Step 3 is made for removing the joint clearances since, only the compliant displacements are intended to be acquired. The step 4 were defined to be full load phase, in which pre-load and an additional load is applied onto the end-effector of the manipulator. In last phase the stiffness matrix of the robot is calculated according to the measurements taken in this phase. Measurements are taken along 3 axis for including the effect of the moments created.

Another method for measuring the compliant displacements is built by researchers (Ceccarelli & Carbone, 2005) which is named as Milli-CATRASYs. This device is able to exert wrenches on the point H, Q and F on the end-effector of the robot manipulator given in Figure 2.14, while measuring the compliant displacements of the wire that is connected to the same points. Then the displacements measured through the LVDT sensors, can be used in calculating the end-effector displacements using the trilateration

technique (Carbone, 2003). Linear Variable Differential Transformers (LVDT) are analog sensors for measuring displacements. The position measurement occurs through electromagnetic coupling. This sensors provide high repeatability. Due to this reason it provides theoretically infinite resolution (marmatek.com/lvdt-rvdt/).

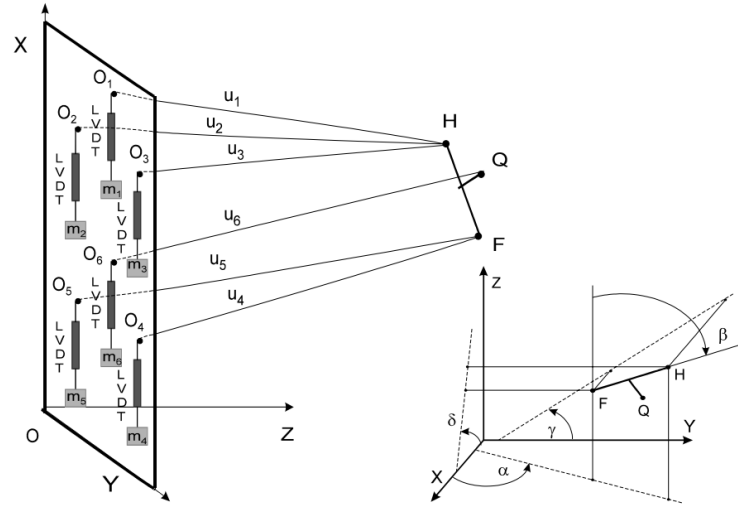


Figure 2.14 Milli-CATRASYs measuring device (Ceccarelli & Carbone, 2005).

As defined in (Carbone, 2011), stiffness matrix of a robot manipulator is symmetric under the conditions of external wrenches and reference frame that the displacement is going to be measured. As given in the work (Kumar, 1997), multiple solutions were calculated for a conservative mechanical system depending on the manipulator and the parameterization of its joint space. Due to this reason, calculation of a 6x6 Cartesian stiffness matrix requires 6 distinguished experiments, which are executed for 6 wrenches. The wrenches, stiffness coefficients and compliant displacements for each experiment is given in Equation 2.57.

$$\begin{aligned}
 {}^iW &= [{}^iF_x \quad {}^iF_y \quad {}^iF_z \quad {}^iM_x \quad {}^iM_y \quad {}^iM_z]^T \\
 {}^iK &= [K_{i1} \quad K_{i2} \quad K_{i3} \quad K_{i4} \quad K_{i5} \quad K_{i6}]^T \quad ; \quad i=1 \rightarrow 6 \\
 {}^i\Delta X &= [{}^i\Delta x \quad {}^i\Delta y \quad {}^i\Delta z \quad {}^i\Delta\theta_x \quad {}^i\Delta\theta_y \quad {}^i\Delta\theta_z]^T
 \end{aligned} \tag{2.57}$$

The measured results for these experiments are collected in the way given in Equation 2.58 and the numerical solution for 6 set of linear equations gives the stiffness matrix coefficients of ${}^i\mathbf{K}$.

$$\begin{bmatrix} {}^i\Delta\mathbf{X} & 0_{6,1} & 0_{6,1} & 0_{6,1} & 0_{6,1} & 0_{6,1} \\ 0_{6,1} & {}^i\Delta\mathbf{X} & 0_{6,1} & 0_{6,1} & 0_{6,1} & 0_{6,1} \\ 0_{6,1} & 0_{6,1} & {}^i\Delta\mathbf{X} & 0_{6,1} & 0_{6,1} & 0_{6,1} \\ 0_{6,1} & 0_{6,1} & 0_{6,1} & {}^i\Delta\mathbf{X} & 0_{6,1} & 0_{6,1} \\ 0_{6,1} & 0_{6,1} & 0_{6,1} & 0_{6,1} & {}^i\Delta\mathbf{X} & 0_{6,1} \\ 0_{6,1} & 0_{6,1} & 0_{6,1} & 0_{6,1} & 0_{6,1} & {}^i\Delta\mathbf{X} \end{bmatrix} \cdot {}^i\mathbf{K} - {}^i\mathbf{W} = 0 \quad i=1 \rightarrow 6 \quad (2.58)$$

Then, the coefficients are combined in a stiffness matrix that is provided in Equation 2.59.

$$\mathbf{K} = \begin{bmatrix} K_{11} & K_{12} & K_{13} & K_{14} & K_{15} & K_{16} \\ K_{21} & K_{22} & K_{23} & K_{24} & K_{25} & K_{26} \\ K_{31} & K_{32} & K_{33} & K_{34} & K_{35} & K_{36} \\ K_{41} & K_{42} & K_{43} & K_{44} & K_{45} & K_{46} \\ K_{51} & K_{52} & K_{53} & K_{54} & K_{55} & K_{56} \\ K_{61} & K_{62} & K_{63} & K_{64} & K_{65} & K_{66} \end{bmatrix} \quad (2.59)$$

2.4. Conclusion for Literature Survey

In this section, methods exist in the literature are given with their details. Firstly, SMA method is explained. SMA takes the robot manipulator as a structure and uses each compliant element's stiffness properties to find the overall stiffness value of the structure. In this approach, the compliant elements are represented with at most 2 nodes and compliant relations between these nodes are superposed in a global stiffness matrix to compute the displacement due to external wrenches. The matrix operations and required mathematical manipulations to end up with an equivalent stiffness matrix for the robot structure is shown. Since the compliant elements of the robot manipulator is given with less number of nodes, computational complexity of the stiffness calculation is lower than

the FEA based method yet the method involves matrix operations of large sizes. Furthermore, approximating a simpler shape for links reduces the accuracy of the method. Lastly, this method is provided for the unloaded mode, which means that external forces and moments are relatively low.

Another method provided here is the VJM. This method simplifies the model by representing the compliancy of the links on joints and allowing a rigid body approach for the robot manipulator. Since this method uses the conventional kinematic calculations, computational complexity is low. An important point for this approach is determining the stiffness matrix of the virtual springs.

Matrix Product Method(MPM) calculates the stiffness matrix of the manipulator by simply making matrix product of matrices that gives the force transmission capability, stiffness values of leg components, leg geometry and leg configurations. This method also provides a closed form representation for the overall stiffness matrix of a parallel kinematic robot manipulator. Since these matrices are written according to the moving platform of the parallel manipulator and considering the parallel kinematic robots with decoupled motion, displacement and coordinate variation matrices due to the stiffness of each leg has lower dimensions. However, complexity increases when the robot have another type of motion characteristics.

As provided in the literature, first given by the decoupled stiffness values are introduced for all force and moment components. Then this is improved by providing the coupled effects of the deflections. After that, it is improved by providing a multi-beam approach to the links. Finally, a FEA-based approach is given. The FEA-based method improves the accuracy of the stiffness model for the robot manipulators composed of links having non-geometric shapes. Furthermore, this method is applied once for a manipulator before the stiffness calculations, therefore, it does not increase the calculation time of the stiffness matrix of the manipulator.

Experimentation for compliancy evaluation is done by measuring the absolute position of the robot that is given by several examples in the literature. The tools for these researches changes from micrometers, inclinometers and modified LVDT systems, which has to touch the end-effector of the robot, to laser trackers and stereo vision cameras that

is measuring the end-effector position of the robot from a distance. The important points for absolute position measurement to be used in compliancy evaluation is to follow a testing procedure and to consider the number of tests to find the stiffness property at a point. Moreover, the testing device should not include its own stiffness into the measurement.

Considering the goals of this thesis, the stiffness calculation methods to be applied must be the one that provides most accurate result for stiffness matrix with least amount of computational expense. Comparing the methods provided in this section VJM and SMA gives the best trade of between accuracy and the computational efficiency. VJM and SMA can be improved by implementing a FEA-based approach for link stiffness identification. For experimentation, using vision sensors provide a good solution considering a wider workspace observation with minimum calibration and not including stiffness of the measuring devices to the evaluated robot.

CHAPTER 3

CASE STUDY: A PARALEL MECHANISM HAPTIC DEVICE

Haptic devices find use in many VR and teleoperation applications such as computer aided design (Ott et al. 2010), entertainment (Faust & Yoo 2006), (Web, 2012), education (Kretz et al., 2005), training (Basdogan et al., 2001), rehabilitation (Broeren et al. 2004), nano-manipulation (Sieber et al., 2008), virtual prototyping (Zhu & Lee, 2004) and virtual sculpting (Leu et al., 2005). Various types of haptic devices are developed, and they are employed in different types of tasks. Especially for accurate teleoperation (Hokayem & Spong, 2006) and precision required VR and medical applications (Ferreira & Mavroidis, 2006), haptic systems that have higher precision levels compared to the current commercially available haptic devices are required. In order to meet this precision criterion, a 6-DoF desktop haptic device, HIPHAD v1.0, was designed and constructed in previous thesis study in IZTECH Robotics Laboratory (Bilgincaan et al., 2010).

In this master thesis, a lower mobility version of HIPHAD v1.0 is taken under the consideration. In the original design, a wrist mechanism was included that was composed of the last 3 DoF and it was a passive serial kinematic chain. Since there were no actuation system in this wrist mechanism, it was not able to reflect any haptic feedback. Therefore, last 3 DoF are excluded from the device and a mobile platform with a fixed handle is assembled to the device. In the following sub-sections, components, kinematic and quasi-static equilibrium analyses, and calibration of this modified version of HIPHAD device is introduced.

3.1. General Information and Specifications of HIPHAD v1.0

HIPHAD v1.0 was designed to provide position feedback signals in the joint space in order to indirectly calculate the pose of the tool handled by the user in space through direct kinematics. Therefore it was configured as a 6-DoF mechanism. Only point-type of contact was designated to be reflected back to the user and to accomplish this only translational motion was required to be constrained by the actuators during operation. The device had hybrid structure which is composed of a 3-DoF active parallel translational mechanism and a 3-DoF passive serial-spherical wrist mechanism. Specifications of the device are listed in Table 3.1.

Table 3.1 Specifications of HIPHAD v1.0 Design.

Sensation Type	Kinesthetic
Mechanical Structure	Hybrid
Control Structure	Open-Loop Impedance
Application Type	Desktop Device
Degrees of Freedom of Motion	6
Type of Contact Simulation	Point-Type of Contact (Forces in 3D)
Continuous Exertable Force	> 0.8 N in all directions
Nominal Positional Resolution	< 0.1 mm
Workspace	120mm W x 120mm H x 120mm D
Footprint	< 200 mm ²

In open-loop impedance type haptic devices, due to the random motion of the operator, no control can be employed to avoid singular positions. Therefore, motion through singular positions must be restricted by design. During the design procedure two singularity conditions are encountered and avoided by necessary precautions in design.

More information on the mechanical design of the device can be found in (Bilgincaan et al., 2010).

3.2. Hardware Used in the Haptic Device

HIPHAD is composed of mechanical, electro-mechanical, and electronics units to facilitate an impedance type haptic system. The mechanical interface of HIPHAD is described in Section 3.3. The electro-mechanical parts used in the mechanism are the sensors and the electrical actuators. HIPHAD has parallelograms in each driving axis that allows using separate position sensors other than the position sensor attached on the rear end of the actuator. With this advantageous design feature, the positional measurements are not restricted to low resolution sensors. In the original design of HIPHAD, potentiometers were used to acquire the angular position of the actuated link indirectly from the other grounded link's angular position. In this thesis work, the potentiometers are swapped with 10-bit quadrature encoders, which resolves a complete turn into 4096 finite steps. In this way, noise problem on the analog potentiometer sensors were eliminated. These sensors, provided in Figure 3.1, are attached on the passive grounded axes of the parallelograms.

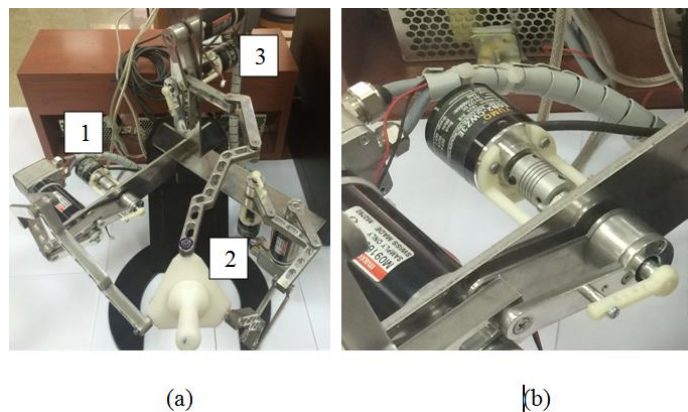


Figure 3.1 In (a), location of the encoders are given by numbers 1, 2 and 3. In (b) enlarged view of encoder 1 is given

The Data Acquisition Card (DAQ) used in this haptic system is the Q8 DAQ from Quanser Consulting Inc. This is a single-board, PCI based, hardware-in-the-loop (HIL) control board. The specification of the Q8 DAQ are given in Table 3.2. In order to interface the HIPHAD device with a computer, 3 quadrature encoder inputs and 3 D/A converters of this DAQ are used. Theoretically, the Q8 DAQ can operate up to 100 KHz sampling rate that is far more than the human motion frequency. It stated that human can feel the haptic feedback that range from 10 Hz to 1 KHz, therefore, haptic devices should be able to provide force feedback in this frequency range (Kern, 2009).

Table 3.2 Specifications of Quanser Q8 DAQ

Item	Quantity	Property
Analog Inputs	8	14-bit
Analog Outputs	8	12-bit
Quadrature Encoder Inputs	8	
I/O Channels	32	Programmable
Dedicated Counter/Timers	2	32-bit
Reconfigurable Encoder Counter/Timers	2	24-bit
PWM Inputs	2	
PCI bus Interface		32-bit 33 MHz

The actuators used in HIPHAD device were selected according to the required continuous torque. To comply with the HIPHAD specifications, a brushless direct current (BLDC) motor from Maxon Motors was selected to provide a maximum of 310 mNm continuous torque to operate without any transmission in direct drive mode.

BLDC amplifiers to drive these motors are Maxon Motor drivers that receive drive signals as analogue voltage inputs in the range of ± 10 VDC. The Q8 DAQ can provide

± 10 VDC analog outputs and therefore, it can drive the motors in their full range. Also BLDC amplifiers allow current control of the motors, which means that torque control can be done. Another important feature of these BLDC amplifiers is that their sampling rate is 1 KHz, which is sufficient for this haptic device application.

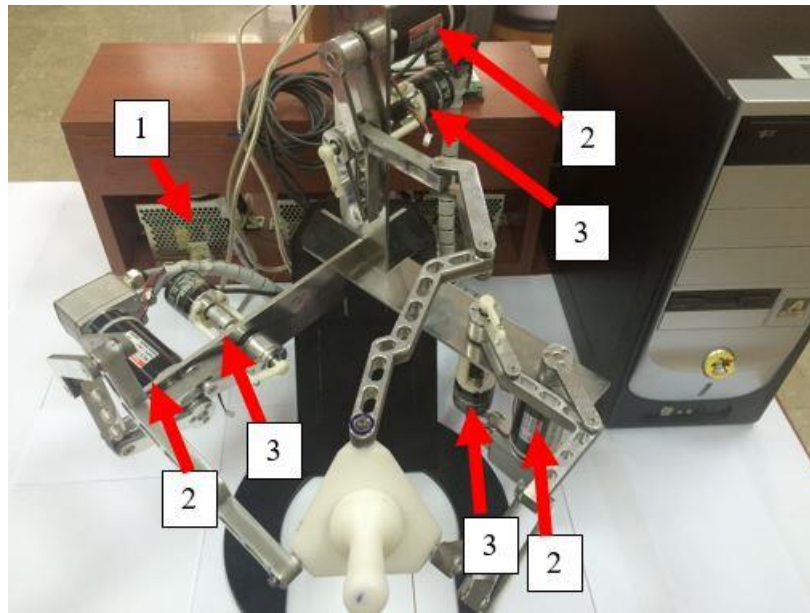


Figure 3.2 HIPHAD v1.0 device composed of 1) BLDC amplifier Box 2) Maxon Motor BLDCs 3) Quadrature Encoders

The manufactured prototype of HIPHAD v1.0 is presented in Figure 3.2 with all of its components. The electro-mechanical and electronic parts denoted by 1, 2, 3 and 4 of the system are provided.

3.3. Kinematic Analysis of the Haptic Device

In HIPHAD v1.0, the translational motion demand to be sent to the slave system is based on the calculation of the wrist point position W_r with respect to the base frame in the task space by utilizing the real-time measurements from the position sensors in direct kinematics calculations. Therefore, the wrist location is measured in an indirect

way which means, direct kinematics is used to calculate the motion demand. The translational mechanism and its parameters are represented in Figure 3.3.

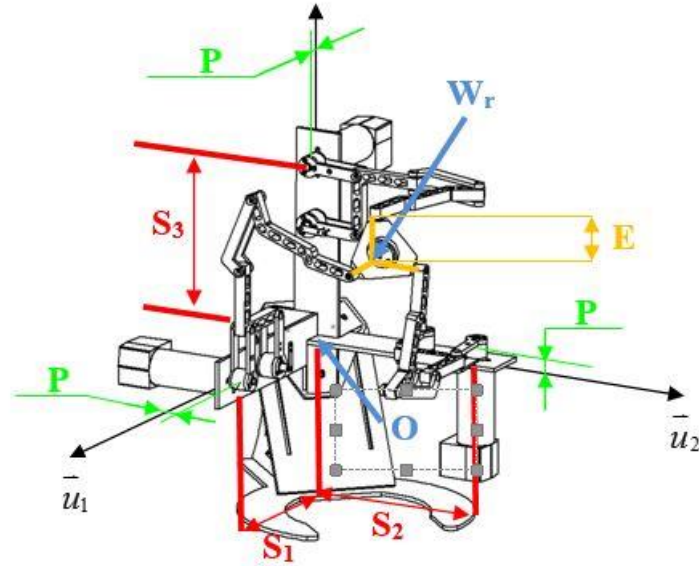


Figure 3.3 Translational parallel mechanism parameters

Translational parallel mechanism of HIPHAD is an R-Cube mechanism, which has decoupled motion along its Cartesian axes shown in the figure as \bar{u}_i ; $i=1,2,3$. Hence, motion along any Cartesian axis is actuated by the actuator located on that axis. In Equation 3.1, calculation of the position vector of the wrist point $\overrightarrow{OW_r}$ with respect to the Cartesian frame, $\mathcal{F} = \mathcal{F}\{O; \bar{u}_1, \bar{u}_2, \bar{u}_3\}$, origin point, O, is described.

$$\begin{aligned} \overrightarrow{W_r} &= \sum_{i=1}^3 W_{ri} \bar{u}_i & i=1,2,3 & \quad (3.1) \\ W_{ri} &= S_i + l_i \cdot \sin(\theta_{i1}) - E \end{aligned}$$

S_1, S_2 and S_3 in Figure 3.3 are the distances from the origin to the related actuation axis along related Cartesian axis. These parameters define the workspace location with respect to the origin, O. Zero/initial/homing position of the mechanism is defined to be in the middle of the workspace and the offsets, which defines the positional difference between the tip point of each leg and wrist point of HIPHAD, is given by the parameter

E in all 3 axes by orthogonal orange lines in Figure 3.3. There is an offset between the base and the first link of the parallelogram by an amount of P, which is denoted in Figure 3.3 by green lines. The initial positions of actuators that define the initial position of the wrist point are given in the Figure 3.4(a).

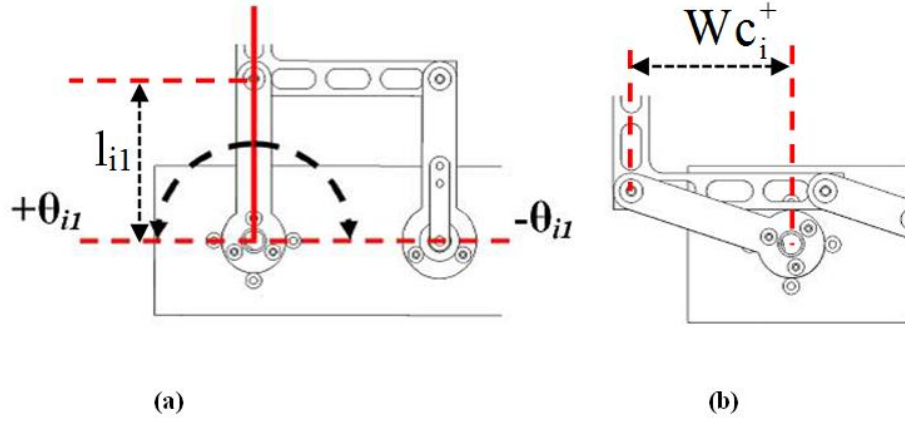


Figure 3.4 (a) Link and joint parameters (b) Joint limit (Dede et al., 2014).

The zero position of the driving link's angular position, θ_{i1} , is represented with solid red line in Figure 3.4(a). Wc_i^+ parameter presented in Figure 3.4(b) indicates the workspace limitation of the mechanism in the positive direction, which is denoted in Figure 3.4(a) with $+\theta_{i1}$. Therefore, in Figure 3.4, Wc_i is theoretically half of the workspace limit along \bar{u}_i and the workspace limitation equation is written with respect to the total angular range of each driving link θ_{i1}^T , which is less than a half rotation.

$$\begin{aligned} \bar{Wc} &= \sum_{i=1}^3 Wc_i \bar{u}_i \quad i=1,2,3 \\ Wc_{TOTAL} &= l_{i1} \cdot \sin(\theta_{TOTAL}^T) \end{aligned} \quad (3.2)$$

Inverse kinematics solution of HIPHAD is provided for the whole kinematic chain including the passive joints on the three legs. The actuating and passive joint angles in the kinematic chain of the leg 1 are given by θ_{11} , θ_{12} , θ_{13} and θ_{14} respectively and these joint angles are denoted in Figure 3.5. As it can be observed from Figure 3.5, axis of rotation joint angles θ_{11} and θ_{12} is the \bar{u}_2 axis and axis of rotation of joint angles θ_{13} and

θ_{14} is the $-\vec{u}_1$ axis. Inverse kinematics analysis to calculate for these angles are used in calibration of the device and stiffness analysis of the device.

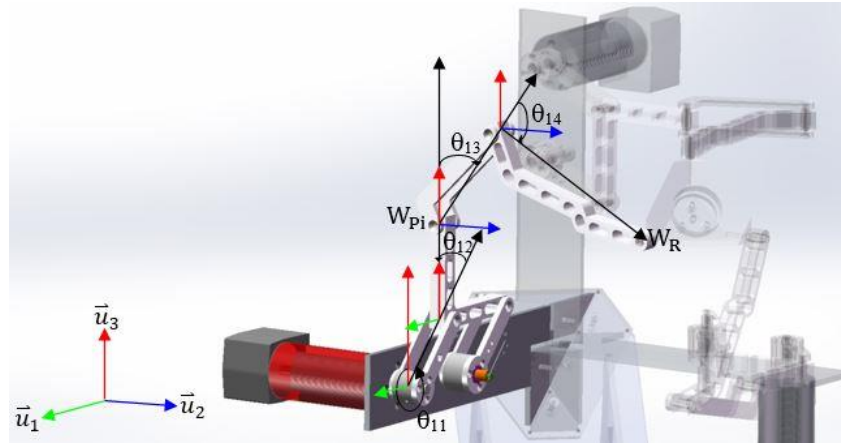


Figure 3.5 Active and passive joint angles of a leg

Due to the mechanical structure of HIPHAD, the actuating joints cannot pass the joint limits provided in (Dede et al., 2014). Therefore, σ in Equation 3.4 can only be 1.

$$\sin(\theta_{i1}) = \frac{W_{ri} - S_i + E}{l_i} \quad i=1,2,3 \quad (3.3)$$

$$\cos(\theta_{i1}) = \sigma \sqrt{1 - \sin^2(\theta_{i1})} \quad i=1,2,3 \quad (3.4)$$

Equation 3.5 provides the solution for θ_{i1} using Equation 3.3 and 3.4.

$$\theta_{i1} = \arctan2(\sin(\theta_{i1}); \cos(\theta_{i1})) \quad (3.5)$$

Link 2, which is the coupler link of the parallelogram, is always secured at the same angular position due to the parallelogram. Therefore, the angle between the first link and the second link, which is given in Figure 3.7 by θ_{i2} , the link 2 has to be maintained parallel and it is given in the Equation 3.6.

$$\begin{aligned}\theta_{i1} + \theta_{i2} &= 0 \\ \theta_{i2} &= -\theta_{i1}\end{aligned}\quad (3.6)$$

Once the θ_{i1} is found, the rest of the joint angles can be found using the difference between the position vectors \overline{W}_{P1} , \overline{W}_{P2} , \overline{W}_{P3} and \overline{W}_r . These position vectors are given in Equations 3.7, 3.8, 3.9 and 3.10.

$$\overline{W}_{P1} = \begin{bmatrix} S_1 + l_{11} \cdot \sin(\theta_{11}) - E \\ P_1 \\ l_{11} \cdot \cos(\theta_{11}) + l_{122} \end{bmatrix} \quad (3.7)$$

$$\overline{W}_{P2} = \begin{bmatrix} l_{21} \cdot \cos(\theta_{21}) + l_{222} \\ S_2 + l_{21} \cdot \sin(\theta_{21}) - E \\ P_2 \end{bmatrix} \quad (3.8)$$

$$\overline{W}_{P3} = \begin{bmatrix} P_3 \\ l_{31} \cdot \cos(\theta_{31}) + l_{322} \\ S_3 + l_{31} \cdot \sin(\theta_{31}) - E \end{bmatrix} \quad (3.9)$$

$$\overline{W}_r = \begin{bmatrix} S_1 + l_{11} \cdot \sin(\theta_{11}) - E \\ S_2 + l_{21} \cdot \sin(\theta_{21}) - E \\ S_3 + l_{31} \cdot \sin(\theta_{31}) - E \end{bmatrix} \quad (3.10)$$

\overline{W}_{P1} , \overline{W}_{P2} and \overline{W}_{P3} is subtracted from the \overline{W}_r . This vector will only have two components, since it will always be on a plane depending on the actuated axis.

$$\overline{W}_r - \overline{W}_{P1} = \begin{bmatrix} 0 \\ S_2 + l_{21} \cdot \sin(\theta_{21}) - E - P_1 \\ S_3 + l_{31} \cdot \sin(\theta_{31}) - E - l_{11} \cdot \cos(\theta_{11}) - l_{122} \end{bmatrix} \quad (3.11)$$

$$\bar{W}_r - \bar{W}_{P2} = \begin{bmatrix} S_1 + l_{32} \cdot \sin(\theta_{32}) - E - l_{11} \cdot \cos(\theta_{12}) - l_{122} \\ 0 \\ S_3 + l_{21} \cdot \sin(\theta_{22}) - E - P_1 \end{bmatrix} \quad (3.12)$$

$$\bar{W}_r - \bar{W}_{P3} = \begin{bmatrix} S_1 + l_{21} \cdot \sin(\theta_{23}) - E - P_1 \\ S_2 + l_{32} \cdot \sin(\theta_{33}) - E - l_{11} \cdot \cos(\theta_{13}) - l_{122} \\ 0 \end{bmatrix} \quad (3.13)$$

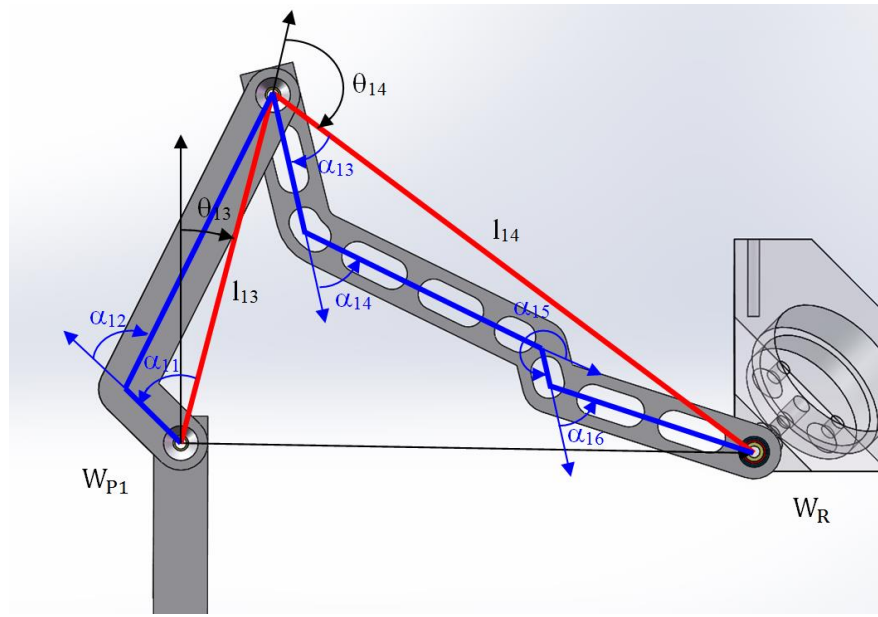


Figure 3.6 Geometric and Kinematic properties of 3rd and 4th links of the 1st leg

Writing the loop closure equations in \bar{u}_2 - and \bar{u}_3 -directions and then summing the squares of these equations will give the result for the θ_{i4} . \bar{u}_2 and \bar{u}_3 components of the loop closure equations are given in Equation 3.14 and 3.15.

$$l_{13} \cdot \sin(\theta_{13}) + l_{14} \cdot \sin(\theta_{13} + \theta_{14}) = W_{R2} \quad (3.14)$$

$$l_{13} \cdot \cos(\theta_{13}) + l_{14} \cdot \cos(\theta_{13} + \theta_{14}) = W_{R3} \quad (3.15)$$

In order to solve for the inverse task to calculate the passive joint angles, first, squares of Equation 3.14 and 3.15 are taken and summed as follows:

$$\begin{aligned}
& l_{13}^2 \cdot \sin^2(\theta_{13}) + l_{14}^2 \cdot \sin^2(\theta_{13} + \theta_{14}) + l_{13}^2 \cdot \cos^2(\theta_{13}) + l_{14}^2 \cdot \cos^2(\theta_{13} + \theta_{14}) + \quad (3.16) \\
& 2 \cdot l_{13} \cdot l_{14} \cdot \sin(\theta_{13}) \cdot \sin(\theta_{13} + \theta_{14}) + 2 \cdot l_{13} \cdot l_{14} \cdot \cos(\theta_{13}) \cdot \cos(\theta_{13} + \theta_{14}) \\
& = W_{R2}^2 + W_{R3}^2
\end{aligned}$$

Equation 3.16 can be reduced to Equation 3.17 by using the difference of two angles of cosine. Then the angle θ_{14} can be found by manipulating the Equation 3.17 as given in Equations 3.18 to 3.19. It should be noted that workspace of HIPHAD is placed away from the singularities. For this reason, there is only one physically possible solution for θ_{14} within the workspace.

$$l_{13}^2 + l_{14}^2 + 2 \cdot l_{13} \cdot l_{14} \cdot \cos(\theta_{14}) = W_{R2}^2 + W_{R3}^2 \quad (3.17)$$

$$\cos(\theta_{14}) = \frac{W_{R3}^2 + W_{R2}^2 - l_{13}^2 - l_{14}^2}{2 \cdot l_{13} \cdot l_{14}} \quad (3.18)$$

$$\sin(\theta_{14}) = \sqrt{1 - \cos^2(\theta_{14})} \quad (3.19)$$

$$\theta_{14} = \text{atan2}(\sin(\theta_{14}); \cos(\theta_{14})) \quad (3.20)$$

Once θ_{14} is found, θ_{13} can be calculated using the following matrix equation and trigonometric equality provided in Equation 3.21 and 3.22.

$$\begin{bmatrix} l_4 \cdot \sin(\theta_{14}) & l_3 + l_4 \cdot \cos(\theta_{14}) \\ l_3 + l_4 \cdot \cos(\theta_{14}) & l_4 \cdot \sin(\theta_{14}) \end{bmatrix} \cdot \begin{bmatrix} \cos(\theta_{13}) \\ \sin(\theta_{13}) \end{bmatrix} = \begin{bmatrix} W_{R2} \\ W_{R3} \end{bmatrix} \quad (3.21)$$

$$\theta_{13} = \text{atan2}(\sin(\theta_{13}); \cos(\theta_{13})) \quad (3.22)$$

Angles calculated in this section are used in stiffness calculations of HIPHAD for the two proposed methods since the stiffness is dependent on the leg configuration. Another

relevant analysis that has to be carried out is the quasi-static force equilibrium analysis and it is provided in the following section.

3.4. Quasi-static Equilibrium Force Analysis

In this sub-section, Recursive Newton-Euler (RNE) method is used to find the reaction forces on each joint and node assuming that there is no motion and there is an external force applied to the moving platform. Therefore, the calculation are carried out for the quasi-static equilibrium case. In order to accommodate this complex calculation, RNE method is applied for each leg separately. The main reason to calculate the reaction forces at each node is that both joint reactions and the internal node reactions are required for SMA. In this sub-section, the calculations are shown only for the first leg because, the procedure applied for the quasi-static force equilibrium analysis of the other legs is the same.

The geometry of the links used in HIPHAD has complex geometries that has to be divided into smaller geometric parts for stiffness analysis. Accordingly, these smaller geometries have to be analyzed first and then connected to each other. Therefore, reaction forces at these nodes have to be calculated.

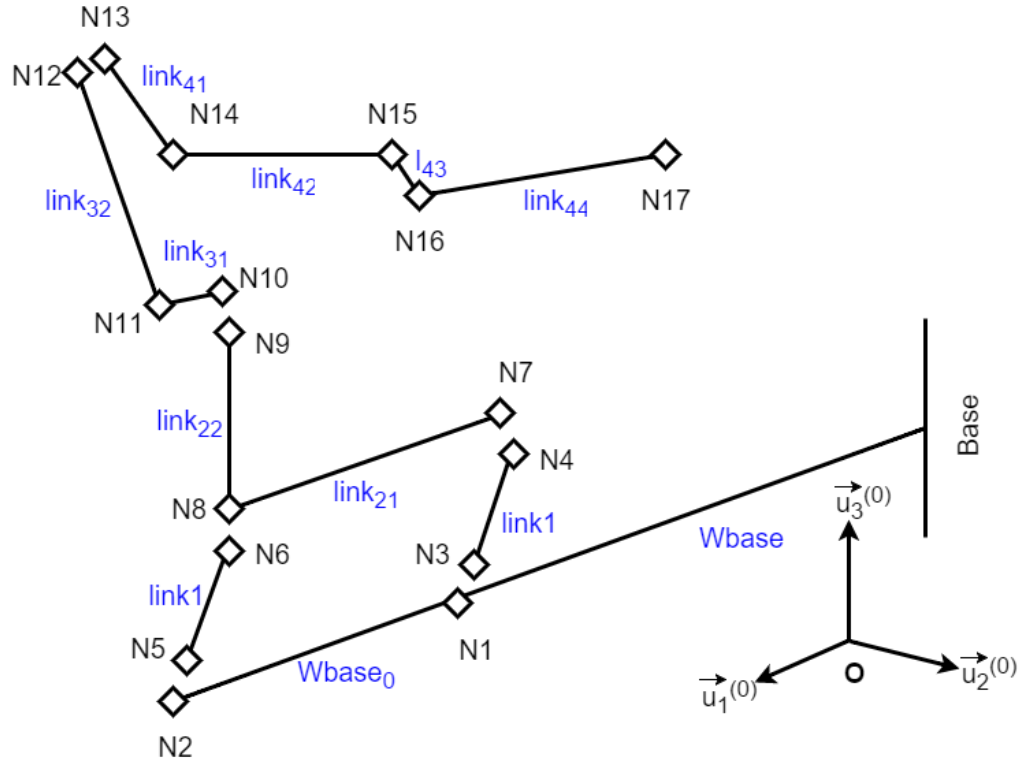


Figure 3.7 Geometric divisions of links and nodes represented for leg 1

Considering the structure of HIPHAD, forces exerted on the moving platform are received or compensated by the actuators on each leg and the components of the external force vector along \bar{u}_1 , \bar{u}_2 and \bar{u}_3 are shared among these actuators according to their directions. In example, external force in \bar{u}_1 -direction is received and balanced by the leg 1 actuator that has an axis of motion about \bar{u}_2 -direction. Leg 1 construction with its nodes and flexible links is represented in Figure 3.7.

Links with passive joints coming after the parallelograms in each leg, are held in their static position by the actuation provided by the other two actuators. The necessary force application point to keep these links in their static position is the N17 point which is shown in Figure 3.7. Considering this design feature, forces that can be balanced by each leg are given in Table 3.3. Forces R_{1i} , R_{2i} and R_{3i} are the reaction forces due to the weights of the free links of leg i acting at i^{th} leg's N17 point. F_1 , F_2 and F_3 are the external force components along \bar{u}_1 , \bar{u}_2 and \bar{u}_3 axes acting on the wrist point, Wr. GE is the weight of the mobile platform. In calculating gravitational and external force effects of links on each node, RNE calculations are carried out for each leg individually.

$$\sum \vec{M}_{J3} = (\vec{J}_5 - \vec{J}_3)^{(0)} \times \vec{F}_{17} + \sum_{n=5}^{10} ((\vec{C}_{n1} - \vec{J}_3)^{(0)} \times \vec{g} \cdot \vec{G}_{n1}) + \vec{M}_{J3} \quad (3.24)$$

In the moment equations 3.23 and 3.24, \vec{M}_{J4} and \vec{M}_{J3} are the moments that can be created on the joints. The vector from the O origin to the kth joint is defined as \vec{J}_k and the vector from the O origin to the nth center of gravity is defined as \vec{C}_{ni} , where i stands for the leg number. As long as joint 3 and joint 4 are considered as fully passive joints without any frictional resistance, moment around \vec{u}_1 -direction is always equal to zero for the first leg.

$$(\vec{J}_5 - \vec{J}_4)^{(0)} \times \vec{F}_{17} = \begin{bmatrix} -R_{21} \cdot l_4 \cdot \cos(\theta_{34}) + R_{31} \cdot l_4 \cdot \sin(\theta_{34}) \\ F_1 \cdot l_4 \cdot \cos(\theta_{34}) \\ -F_1 \cdot l_4 \cdot \sin(\theta_{34}) \end{bmatrix} \quad (3.25)$$

$$(\vec{J}_5 - \vec{J}_3)^{(0)} \times \vec{F}_{17} = \begin{bmatrix} -R_{21} \cdot l_3 \cdot \cos(\theta_3) - R_{21} \cdot l_4 \cdot \cos(\theta_{34}) + R_{31} \cdot l_3 \cdot \sin(\theta_3) + R_{31} \cdot l_4 \cdot \sin(\theta_{34}) \\ F_1 \cdot l_3 \cdot \cos(\theta_3) + F_1 \cdot l_4 \cdot \cos(\theta_{34}) \\ -F_1 \cdot l_3 \cdot \sin(\theta_3) - F_1 \cdot l_4 \cdot \sin(\theta_{34}) \end{bmatrix} \quad (3.26)$$

Equations 3.25 and 3.26 gives the moments generated by the external forces and reaction forces. Vectors A and B, which are given in 3.27 and 3.28, represent the moments generated by the gravitational effects in 3.23 and 3.24, respectively. These vectors only have their \vec{u}_i elements not equal to zero for leg i.

$$\vec{A} = \sum_{n=7}^{10} ((\vec{C}_{n1} - \vec{J}_4)^{(0)} \times \vec{g} \cdot \vec{G}_{n1}) \quad (3.27)$$

$$\vec{B} = \sum_{n=5}^{10} ((\vec{C}_{n1} - \vec{J}_3)^{(0)} \times \vec{g} \cdot \vec{G}_{n1}) \quad (3.28)$$

Using this feature of the moments created by the gravitational effects, R_2 and R_3 can be computed by using the linear equation set given in Equation 3.29 and 3.30. This equation set is derived from the vector Equations 3.23 and 3.24 by extracting the scalar equations in \vec{u}_1 -direction.

$$-R_{21} \cdot l_4 \cdot \cos(\theta_{34}) + R_{31} \cdot l_4 \cdot \sin(\theta_{34}) + A_1 = 0 \quad (3.29)$$

$$\begin{aligned} -R_{21} \cdot l_3 \cdot \cos(\theta_3) - R_{21} \cdot l_4 \cdot \cos(\theta_{34}) + \\ R_{31} \cdot l_3 \cdot \sin(\theta_3) + R_{31} \cdot l_4 \cdot \sin(\theta_{34}) + B_1 = 0 \end{aligned} \quad (3.30)$$

R_{21} and R_{31} are solved by substituting R_{31} from Equations 3.29 into 3.30. After this operation, R_{31} and R_{21} are solved analytically as presented in Equations 3.31 and 3.32.

$$R_{31} = (-A_1 + R_{21} \cdot l_4 \cdot \cos(\theta_{34})) \quad (3.31)$$

$$R_{21} = \frac{(-A_1 + R_{21} \cdot l_4 \cdot \cos(\theta_{34})) \cdot (l_3 \cdot \sin(\theta_3) + l_4 \cdot \sin(\theta_{34}))}{l_4 \cdot \sin(\theta_{34}) \cdot (l_3 \cdot \cos(\theta_3) + l_4 \cdot \cos(\theta_{34}))} + \frac{B_1}{l_3 \cdot \cos(\theta_3) + l_4 \cdot \cos(\theta_{34})} \quad (3.32)$$

The same calculations are applied to the second leg that has similar structure to the one given in Figure 3.8. The only difference in the analysis for reaction force is the direction of the external force applied on N17 and the initial orientation of this leg with respect to the world frame. Due to these differences, moment arms for the gravitational forces have components on \vec{u}_3 - \vec{u}_1 plane this results in a moment about \vec{u}_2 -axis. Therefore, \bar{A} and \bar{B} only have elements in \vec{u}_2 -direction and the calculation for this part is derived from the scalar equations in \vec{u}_2 -direction. Analytical solution for reaction forces R_{12} and R_{32} are given in Equation 3.33 and 3.34.

$$R_{12} = (-A_2 + R_{32} \cdot l_4 \cdot \cos(\theta_{34})) \quad (3.33)$$

$$R_{32} = \frac{A_2 \cdot (l_3 \cdot \sin(\theta_3) + l_4 \cdot \sin(\theta_{34})) - B_2 \cdot l_4 \cdot \sin(\theta_{34})}{(l_3 \cdot \sin(\theta_3) + l_4 \cdot \sin(\theta_{34})) \cdot l_4 \cdot \cos(\theta_{34}) - (l_3 \cdot \cos(\theta_3) + l_4 \cdot \cos(\theta_{34})) \cdot l_4 \cdot \sin(\theta_{34})} \quad (3.34)$$

Once the reaction forces created by free links on mobile platform are calculated and distributed among the legs, then the moments and forces created on the nodes can be calculated by using free body diagrams (FBD) of the parts that are shown in Figures 3.9, 3.10 and 3.11. Moment equations are formulated with respect to the node that is closer to the HIPHAD base.

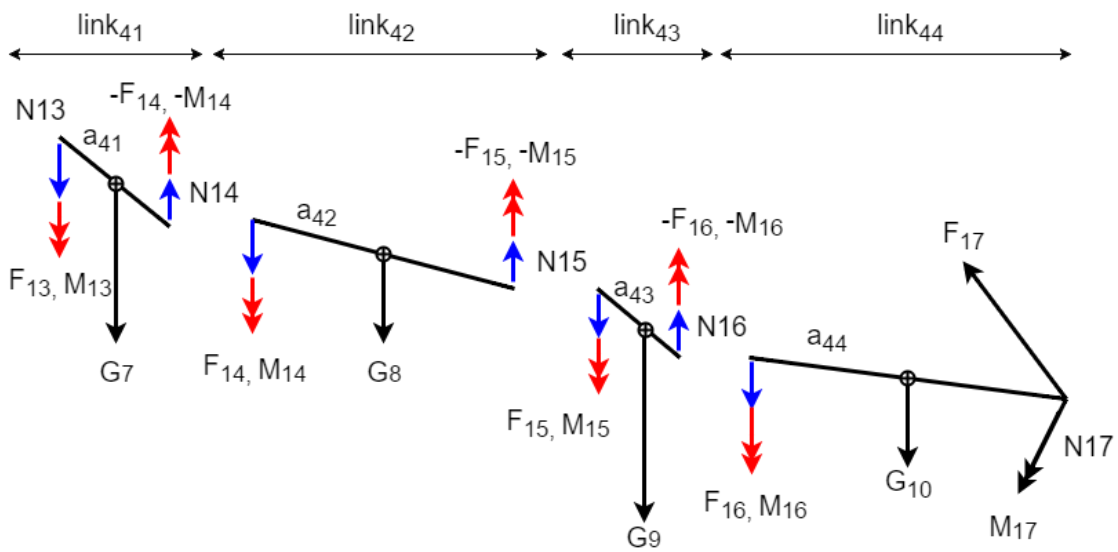


Figure 3.9 FBDs of l41, l42, l43 and l44 that are decomposed from link 4.

In Figure 3.9, FBD for link 4 is given. Link 4 is divided into smaller geometric parts named link41, link42, link43, link44 respectively from left to right. These smaller parts are presented in Figure 3.7 between nodes N13 and N17. a_{41} , a_{42} , a_{43} and a_{44} stand for the magnitude of the position vector from node, which is closer to the base, to the gravity center of the related part.

Force equilibrium condition for part link₄₄;

$$\begin{aligned}\vec{F}_{16} + \vec{G}_{10} + \vec{F}_{17} &= \vec{0} \\ \vec{F}_{16} &= -\vec{G}_{10} - \vec{F}_{17}\end{aligned}\tag{3.35}$$

Moment equilibrium conditions for part link₄₄:

$$\begin{aligned}\sum \vec{M}_{N16} &= \vec{0}; \\ \vec{M}_{16} + \vec{a}_{44} \times \vec{G}_{10} + \vec{l}_{44} \times \vec{F}_{17} + \vec{M}_{17} &= \vec{0} \\ \vec{M}_{16} &= -\vec{a}_{44} \times \vec{G}_{10} - \vec{l}_{44} \times \vec{F}_{17} - \vec{M}_{17}\end{aligned}\tag{3.36}$$

Force equilibrium conditions for part link₄₃:

$$\begin{aligned}\vec{F}_{15} + \vec{G}_9 - \vec{F}_{16} &= \vec{0} \\ \vec{F}_{15} &= -\vec{G}_9 + \vec{F}_{16}\end{aligned}\tag{3.37}$$

Moment equilibrium conditions for part link₄₃:

$$\begin{aligned}\sum \vec{M}_{N15} &= \vec{0}; \\ \vec{M}_{15} + \vec{a}_{43} \times \vec{G}_9 + \vec{l}_{43} \times (-\vec{F}_{16}) - \vec{M}_{16} &= \vec{0} \\ \vec{M}_{15} &= -\vec{a}_{43} \times \vec{G}_9 - \vec{l}_{43} \times (-\vec{F}_{16}) + \vec{M}_{16}\end{aligned}\tag{3.38}$$

Force equilibrium conditions for part link₄₂:

$$\begin{aligned}\vec{F}_{14} + \vec{G}_8 - \vec{F}_{15} &= \vec{0} \\ \vec{F}_{14} &= -\vec{G}_8 + \vec{F}_{15}\end{aligned}\tag{3.39}$$

Moment equilibrium conditions for part link₄₂:

$$\begin{aligned}\sum \vec{M}_{N14} &= \vec{0}; \\ \vec{M}_{14} + \vec{a}_{42} \times \vec{G}_8 + \vec{l}_{42} \times (-\vec{F}_{15}) - \vec{M}_{15} &= \vec{0} \\ \vec{M}_{14} &= -\vec{a}_{42} \times \vec{G}_8 - \vec{l}_{42} \times (-\vec{F}_{15}) + \vec{M}_{15}\end{aligned}\tag{3.40}$$

Force equilibrium conditions for part link₄₁:

$$\begin{aligned}\vec{F}_{13} + \vec{G}_7 - \vec{F}_{14} &= \vec{0} \\ \vec{F}_{13} &= -\vec{G}_7 + \vec{F}_{14}\end{aligned}\quad (3.41)$$

Moment equilibrium conditions for part link₄₁:

$$\begin{aligned}\sum \vec{M}_{N13} &= \vec{0}; \\ \vec{M}_{13} + \vec{a}_{41} \times \vec{G}_7 + \vec{l}_{41} \times (-\vec{F}_{14}) - \vec{M}_{14} &= \vec{0} \\ \vec{M}_{13} &= -\vec{a}_{41} \times \vec{G}_7 - \vec{l}_{41} \times (-\vec{F}_{14}) + \vec{M}_{14}\end{aligned}\quad (3.42)$$

The same procedure is carried out for link 3 that is given in Figure 3.10. Link 3 is divided into smaller geometric parts named l₃₁, l₃₂ respectively from left to right. a₃₁ and a₃₂ stands for the magnitude of the position vector from the node, which is closer to the base, to gravity center of the related part.

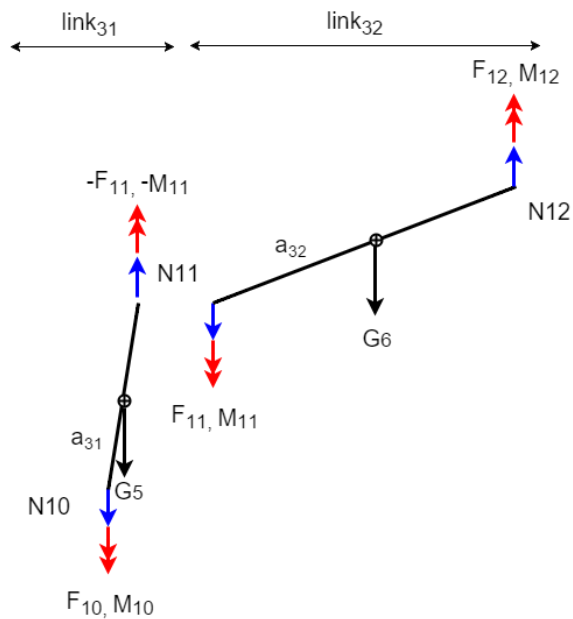


Figure 3.10 Reaction forces and moments on nodes for link 3.

$$\begin{aligned}\vec{F}_{12} &= -\vec{F}_{13} \\ \vec{M}_{12} &= -\vec{M}_{13}\end{aligned}\tag{3.43}$$

Force equilibrium condition for part link₃₂;

$$\begin{aligned}\vec{F}_{11} + \vec{G}_6 + \vec{F}_{12} &= \vec{0} \\ \vec{F}_{11} &= -\vec{G}_6 - \vec{F}_{12}\end{aligned}\tag{3.44}$$

Moment equilibrium condition for part link₃₂;

$$\begin{aligned}\sum \vec{M}_{N11} &= \vec{0}; \\ \vec{M}_{11} + \vec{a}_{32} \times \vec{G}_6 + \vec{l}_{32} \times \vec{F}_{12} + \vec{M}_{12} &= \vec{0} \\ \vec{M}_{11} &= -\vec{a}_{32} \times \vec{G}_6 - \vec{l}_{32} \times \vec{F}_{12} - \vec{M}_{12}\end{aligned}\tag{3.45}$$

Force equilibrium condition for part link₃₁;

$$\begin{aligned}\vec{F}_{10} + \vec{G}_5 - \vec{F}_{11} &= \vec{0} \\ \vec{F}_{10} &= -\vec{G}_5 + \vec{F}_{11}\end{aligned}\tag{3.46}$$

Moment equilibrium condition for part link₃₁;

$$\begin{aligned}\sum \vec{M}_{N10} &= \vec{0}; \\ \vec{M}_{10} + \vec{a}_{31} \times \vec{G}_5 + \vec{l}_{31} \times (-\vec{F}_{11}) - \vec{M}_{11} &= \vec{0} \\ \vec{M}_{10} &= -\vec{a}_{31} \times \vec{G}_5 - \vec{l}_{31} \times (-\vec{F}_{11}) + \vec{M}_{11}\end{aligned}\tag{3.47}$$

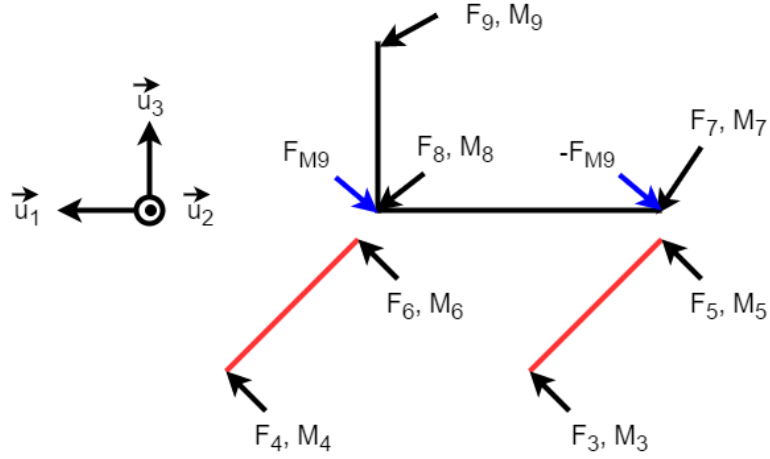


Figure 3.11 FBD of the parallelogram

\vec{F}_9 and \vec{M}_9 that are exerted on node N9 do not include force along \vec{u}_2 -axis and moment about \vec{u}_1 -axis. The system presented in Figure 3.11 cannot be solved since the parallelogram is a planar mechanism and there is a moment element about \vec{u}_3 -axis. To overcome this problem, component of \vec{M}_9 about \vec{u}_3 -axis is extracted from the force analysis of the parallelogram and then included to the calculation of reaction forces at nodes 7 and 8 as couple forces. This assumption enables forcing coming from node 9 to be transmitted to nodes 6 and 5. The force equilibrium for link 2 of four bar mechanism is written in Equation 3.48.

$$\begin{bmatrix} F_{9_x} \\ 0 \\ F_{9_z} \end{bmatrix} + \begin{bmatrix} F_{8_x} \\ 0 \\ F_{8_z} \end{bmatrix} + \begin{bmatrix} F_{7_x} \\ 0 \\ F_{7_z} \end{bmatrix} = \begin{bmatrix} 0 \\ 0 \\ 0 \end{bmatrix} \quad (3.48)$$

Moment equilibrium taken at node 8 is given in Equation 3.49.

$$\begin{bmatrix} 0 \\ M_{\theta_2} \\ M_{\theta_3} \end{bmatrix} + \begin{bmatrix} 0 & -1_{22} & 0 \\ 1_{22} & 0 & 0 \\ 0 & 0 & 0 \end{bmatrix} \cdot \begin{bmatrix} F_{9_1} \\ 0 \\ F_{9_3} \end{bmatrix} + \begin{bmatrix} 0 & 0 & 0 \\ 0 & 0 & -1_{21} \\ 0 & 1_{21} & 0 \end{bmatrix} \cdot \begin{bmatrix} F_{7_1} \\ 0 \\ F_{7_3} \end{bmatrix} = \begin{bmatrix} 0 \\ 0 \\ 0 \end{bmatrix} \quad (3.49)$$

From Equation 3.49, F_{7_3} is calculated as presented in Equation 3.50.

$$F_{7_3} = \frac{M_{9_2} + F_{9_1} \cdot l_{22}}{l_{21}} \quad (3.50)$$

Once \vec{u}_3 component of \vec{F}_7 is calculated the \vec{u}_1 element of it is written as in Equation 3.51.

$$F_{7_1} = \cot(\theta_{11}) \cdot F_{7_3} \quad (3.51)$$

Then \vec{F}_8 is calculated by substituting \vec{F}_7 into Equation 3.47. The reaction forces to balance the moment M_{9z} is included into the system by calculating couple forces. This calculation is given in Equation 3.52.

$$\begin{aligned} {}^{N8}F_{M9} &= -M_{9_z} \cdot l_{21} \\ {}^{N7}F_{M9} &= M_{9_z} \cdot l_{21} \end{aligned} \quad (3.52)$$

When these reaction force are superposed with \vec{F}_8 and \vec{F}_7 the resultant forces at nodes 7 and 8 are formed as given in Equations 3.53 and 3.54, respectively.

$$\begin{bmatrix} F_{8_x} \\ {}^{N8}F_{M9} \\ F_{8_z} \end{bmatrix} \quad (3.53)$$

$$\begin{bmatrix} F_{7_x} \\ {}^{N7}F_{M9} \\ F_{7_z} \end{bmatrix} \quad (3.54)$$

Once these forces are calculated, rest of the force analysis for HIPHAD is calculated by applying following procedure.

$$\begin{aligned}\vec{F}_6 &= -\vec{F}_8 \\ \vec{M}_6 &= -\vec{M}_8\end{aligned}\tag{3.55}$$

$$\begin{aligned}\vec{F}_5 &= -\vec{F}_7 \\ \vec{M}_5 &= -\vec{M}_7\end{aligned}\tag{3.56}$$

$$\begin{aligned}\vec{F}_4 + \vec{G}_2 + \vec{F}_6 &= \vec{0} \\ \vec{F}_4 &= -\vec{G}_2 - \vec{F}_6\end{aligned}\tag{3.57}$$

$$\begin{aligned}\vec{F}_3 + \vec{G}_1 + \vec{F}_5 &= \vec{0} \\ \vec{F}_3 &= -\vec{G}_1 - \vec{F}_5\end{aligned}\tag{3.58}$$

Moment equilibrium formulations for link11 and link 12 are provided in Equations 3.59 and 3.60.

$$\begin{aligned}\sum \vec{M}_{N4} &= \vec{0}; \\ \vec{M}_4 + \vec{a}_{11} \times \vec{G}_2 + \vec{l}_{11} \times \vec{F}_6 + \vec{M}_6 &= \vec{0} \\ \vec{M}_4 &= -\vec{a}_{11} \times \vec{G}_2 - \vec{l}_{11} \times \vec{F}_6 - \vec{M}_6\end{aligned}\tag{3.59}$$

$$\begin{aligned}\sum \vec{M}_{N3} &= \vec{0}; \\ \vec{M}_3 + \vec{a}_{11} \times \vec{G}_2 + \vec{l}_{11} \times \vec{F}_5 + \vec{M}_5 &= \vec{0} \\ \vec{M}_3 &= -\vec{a}_{11} \times \vec{G}_2 - \vec{l}_{11} \times \vec{F}_5 - \vec{M}_5\end{aligned}\tag{3.60}$$

Finally, forces acting on N2 and N1 nodes are calculated by the following equations given in Equations 3.61 and 3.62, respectively.

$$\begin{aligned}\vec{F}_2 &= -\vec{F}_4 \\ \vec{M}_2 &= -\vec{M}_4\end{aligned}\tag{3.61}$$

$$\begin{aligned}\vec{F}_1 &= -\vec{F}_3 \\ \vec{M}_1 &= -\vec{M}_3\end{aligned}\tag{3.62}$$

3.5. Calibration of the Haptic Device

The purpose of calibration is to match angular position measurements from the encoders, which are placed on a grounded leg of each parallelogram, to the wrist point, W_r , position. To achieve this, first the absolute position of W_r is measured using stereo cameras. Later, the position of the wrist at each end of the cubic workspace is transferred into joint space by inverse kinematics calculations in order to find the joint motion limits. Finally, the joint limits are matched with joint sensor readings acquired by the quadrature encoders that are represented in Section 3.2.

For absolute measurement of the wrist point, workspace is divided into two perpendicular planes, $\bar{u}_1 - \bar{u}_3$ and $\bar{u}_2 - \bar{u}_3$. On those planes, location of the mobile platform in \bar{u}_1 -, \bar{u}_2 - and \bar{u}_3 -directions are measured by two cameras, which are parallel to the normal of the selected planes as shown in the Figure 3.13 with red arrows. Blue arrows in this figure represent the Cartesian coordinate axes. 1, 2 and 3 stands for the \bar{u}_1 , \bar{u}_2 and \bar{u}_3 axes respectively.

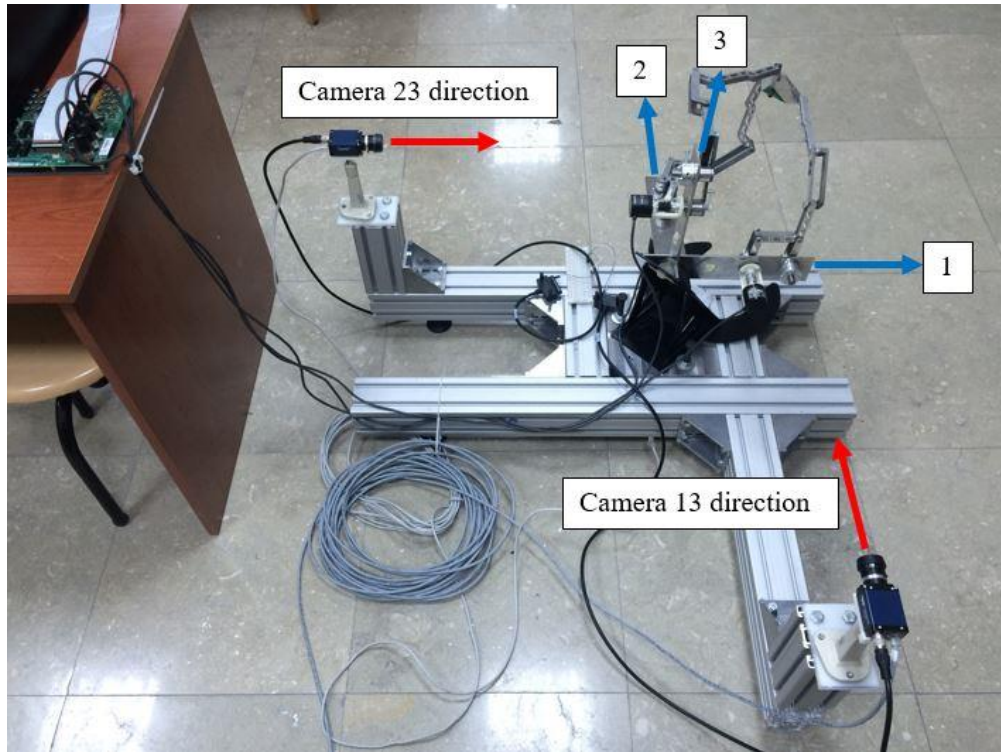


Figure 3.12 Test Setup for calibration

Before carrying out W_r position measurement tests, camera is calibrated by using camera calibration application of Matlab[®]. For calibration, a checkerboard pattern is placed on the mobile platform as represented in Figure 3.14. This is a 6 by 5 checkerboard pattern having squares with 7 mm side lengths. Part denoted with 1, is the ball head assembly that enables different orientations of the calibration pattern.

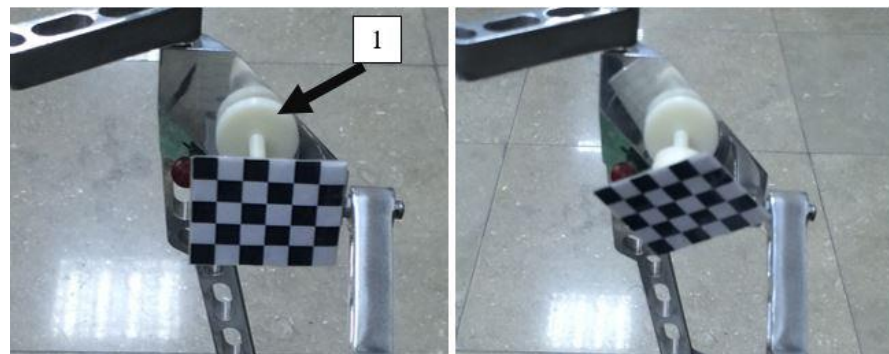


Figure 3.13 Checkerboard pattern in different orientations for calibration.

Once this geometric camera calibration is executed, intrinsic and extrinsic parameters of the cameras are obtained. Extrinsic parameters represent the rotation matrix and translation vector that relates the world coordinate system (Cartesian coordinates) to the camera coordinate system. Intrinsic parameters are described as the skew coefficient, the focal length, the principal point and the optical center (Zhang, 2000). Using these parameters, lens distortion is eliminated and planar measurements for mobile platform are carried out.

Total translation of the device along each direction, Wc_i , is divided into two. The two parts are denoted as Wc_i^+ and Wc_i^- representing the positive and negative translations that will be used for calculating θ_{i1}^+ and θ_{i1}^- angles. Test procedure is initiated by finding the mid-position of the joint range, where $\theta_{i1} = 0^\circ$, by using a set-square. Then the mobile platform is moved to its positive and negative limits along \vec{u}_i , which are denoted with Wc_i^+ and Wc_i^- , of the mechanism are measured via cameras. Measured workspace limits are used for calculating the joint limits θ_{i1}^+ and θ_{i1}^- as described in the Equation 3.63. This calibration methodology is applied to both versions of HIPHAD haptic device that had different position sensors. Previous version of HIPHAD had potentiometers as position sensors. The calibration results with the potentiometers were presented in (Dede et al., 2014). To eliminate noise on the analog signal from the potentiometers, these sensors were changed with encoders that are presented in Section 3.1.1. The calibration procedure was first applied on the HIPHAD having potentiometers and then, the same calibration technique is conducted for the new version with encoders. This section covers these two calibration processes.

$$\begin{aligned}\theta_{i1}^+ &= \arcsin(Wc_i^+/l_i) \\ \theta_{i1}^- &= \arcsin(Wc_i^-/l_i)\end{aligned}\quad i = 1, 2, 3 \quad (3.63)$$

The measured and the calculated parameters for older and newer versions are tabulated in Table 3.4 and 3.5

Table 3.4 Measured values from cameras and calculated joint limits by using potentiometers

Workspace Limits	Measured Values (mm)	Joint Limits	Calculated Values (°)
Wc_1^+ / Wc_1^-	60,45 / 60,45	$\theta_{11}^+ / \theta_{11}^-$	68,44 / 68,44
Wc_2^+ / Wc_2^-	58,89 / 60,25	$\theta_{21}^+ / \theta_{21}^-$	67,95 / 64,96
Wc_3^+ / Wc_3^-	58,86 / 62,03	$\theta_{31}^+ / \theta_{31}^-$	72,60 / 64,90

Table 3.5 Measured Values from Cameras and Calculated Joint Limits by using Encoders

Workspace Limits	Measured Values (mm)	Joint Limits	Calculated Values (°)
Wc_1^+ / Wc_1^-	60,98 / 61,01	$\theta_{11}^+ / \theta_{11}^-$	69.74/ 69.82
Wc_2^+ / Wc_2^-	60,11 / 60,44	$\theta_{21}^+ / \theta_{21}^-$	67.63/ 68,41
Wc_3^+ / Wc_3^-	61,13/ 61,21	$\theta_{31}^+ / \theta_{31}^-$	70.12 / 70.33

In the tests for the two versions of HIPHAD, two different cameras were used. The tests for the potentiometer version was carried out with simple webcams, which were not reliable as the ones that were used for the second version. Also for the tests with the second version, lens distortion was not taken into account. This difference in test procedure resulted in different measurements for the workspace of the mechanism, which can be observed from Table 3.4 and 3.5.

Pulses measured from the encoders at the edges and midpoints of the workspace are given in Table 3.6 with respect to the axis numbers that the encoder is mounted to. These values that are measured at the joint limits are indicated with “min” and “max” subscripts, and also for the mid-position of the workspace, they are indicated with “mid” subscript. Data provided in Table 3.6 show the mean values of 20 measurements. The confidence level for these measurements are 95%. The procedure for these measurements

are first the pulses are measured at the folded position of the mechanisms, then the mobile platform is taken to the mid position and retracted back to the initial position. After the mechanisms is retracted to its initial position, encoder measurement for the initial position is recorded again. Finally, the mechanisms is taken to its fully extended position and it is again taken back to its initial position. As a result of this procedure, it can be observed that the encoder measurement at the initial position is not equal to zero pulse. The main reason for this could be the elastic behavior of the stopper at the bottom of the coupler link of the parallelograms.

The measurement ranges in between the joint limits are provided to be used in constant gain, K_i , calculation for converting the raw data received from the encoders during operation to measured joint positions. Calculation of K_i is given in Equation 3.64. Sr_i in this equation is the total range of sensed signal which is the pulse range for encoder and the voltage range for potentiometer.

$$K_i = (\theta_{i1}^+ + \theta_{i1}^-) / Sr_i \quad (3.64)$$

Table 3.6 Number of pulses read from the encoders.

Encoder ₁		Encoder ₂		Encoder ₃				
Pulse	Pulse Range (Sr ₁)	Pulse	Pulse Range (Sr ₂)	Pulse	Pulse Range (Sr ₃)			
Pmin ₁	6.8	Pmin ₂	-4.25	Pmin ₃	0.8			
Pmid ₁	795.1	1593.3	Pmid ₂	767.6	1595.8	Pmid ₃	798.1	1593.9
Pmax ₁	1600.1	Pmax ₂	1591.6	Pmax ₃	1594.7			

Once the gain K_i is calculated from calibration, it is used to find the joint angles at any instant during operation. This is achieved via Equation 3.65 by using measured pulses from the sensors of the joints, Pm_i for $i=1, 2, 3$.

$$(Pm_i - Pmid_i) \times K_i = \theta_{i1} \quad (3.65)$$

3.6. Stiffness Calculation of HIPHAD Using SMA

Stiffness calculation of HIPHAD is explained under four subsections which are listed as general stiffness matrix formulation, coupling geometric constraints with stiffness matrix, equivalent stiffness matrix calculation for the desired node and stiffness mapping. In SMA method, the procedure explained in literature is followed and important parameters are given in this section. Table 3.7 provides the geometric properties of the links. L is the length of links and each small partition of the links, A is cross-sectional area of the link, I_y , and I_z are the second moment of area of the links about y and z axes at the center of volume and finally J is the moment of gyration.

Table 3.7 Material and geometric properties of links

	Wb1	Wb2	l11 / l12	l21	l22		
L (m)	0.144	0.076	0.065	0.076	0.076		
A (m ²)	0.0003	0.0003	0.000112	0.000196	0.000196		
I_y (m ⁴)	0.00000009	0.00000009	1.82933E-09	3.20133E-09	3.20133E-09		
I_z (m ⁴)	6.25E-10	6.25E-10	1.20883E-08	3.20133E-09	3.20133E-09		
J (m ⁴)	9.0625E-08	9.0625E-08	1.39176E-08	6.40267E-09	6.40267E-09		
	l31	l32	l41	l42	l43	l44	
L (m)	0.02	0.085071	0.0365514	0.0672424	0.0104433	0.0555788	
A (m ²)	0.000084	0.000084	0.000168	0.000168	0.000168	0.000168	
I_y (m ⁴)	1.372E-09	1.372E-09	2.744E-09	2.744E-09	2.744E-09	2.744E-09	
I_z (m ⁴)	8.9962E-09	8.9962E-09	2.016E-09	2.016E-09	2.016E-09	2.016E-09	
J (m ⁴)	1.03682E-08	1.03682E-08	4.76E-09	4.76E-09	4.76E-09	4.76E-09	

These properties are used to calculate the local stiffness matrices of links that are represented in this section with the symbols ${}^{Wb1}\hat{K}^{Wb1}$, ${}^{Wb2}\hat{K}^{Wb2}$, ${}^{l11}\hat{K}^{l11}$, ${}^{l21}\hat{K}^{l21}$, ${}^{l22}\hat{K}^{l22}$, ${}^{l31}\hat{K}^{l31}$, ${}^{l32}\hat{K}^{l32}$, ${}^{l41}\hat{K}^{l41}$, ${}^{l42}\hat{K}^{l42}$, ${}^{l43}\hat{K}^{l43}$ and ${}^{l44}\hat{K}^{l44}$ from the origin to the mobile platform. After these matrices are calculated, the rotation matrices are found using forward kinematics. The active and the passive joints' angular positions are calculated as presented in Section 3.1. The rotation matrices formulated with respect to the angular

positions of the joints are named $\hat{\mathbf{R}}^{(b,Wb1)}$, $\hat{\mathbf{R}}^{(b,Wb2)}$, $\hat{\mathbf{R}}^{(b,I11)}$, $\hat{\mathbf{R}}^{(b,I21)}$, $\hat{\mathbf{R}}^{(b,I22)}$, $\hat{\mathbf{R}}^{(b,I31)}$, $\hat{\mathbf{R}}^{(b,I32)}$, $\hat{\mathbf{R}}^{(b,I41)}$, $\hat{\mathbf{R}}^{(b,I42)}$, $\hat{\mathbf{R}}^{(b,I43)}$, $\hat{\mathbf{R}}^{(b,I44)}$ from the base to the mobile platform.

After the above calculations, stiffness matrices of the links in world frame are calculated using Equation 2.7. As a result of this, stiffness matrices become suitable to be integrated into the total stiffness matrix of the respective leg. The stiffness matrices rotated into world coordinates are denoted as ${}^b\hat{\mathbf{K}}^{Wb1}$, ${}^b\hat{\mathbf{K}}^{Wb2}$, ${}^b\hat{\mathbf{K}}^{I11}$, ${}^b\hat{\mathbf{K}}^{I21}$, ${}^b\hat{\mathbf{K}}^{I22}$, ${}^b\hat{\mathbf{K}}^{I31}$, ${}^b\hat{\mathbf{K}}^{I32}$, ${}^b\hat{\mathbf{K}}^{I41}$, ${}^b\hat{\mathbf{K}}^{I42}$, ${}^b\hat{\mathbf{K}}^{I43}$ and ${}^b\hat{\mathbf{K}}^{I44}$. Total stiffness matrix of each leg is developed using the analogy given in Equation 2.8. The legs of HIPHAD are represented with 17 nodes which were given in Figure 3.7. These nodes are placed in the beginning and at the end of the modeled element and if the node is shared by other modelled elements of the leg, it is superposed with the stiffness value of the same node of the neighbor element. The superposed resultant matrices are graphically provided in Figure 3.15 with red slots. Green slots in this figure denote that the same values of the stiffness matrix of the elements are used in the total stiffness matrix, $\hat{\mathbf{K}}_T$. Total stiffness matrix provided in this figure is a 102 by 102 matrix.

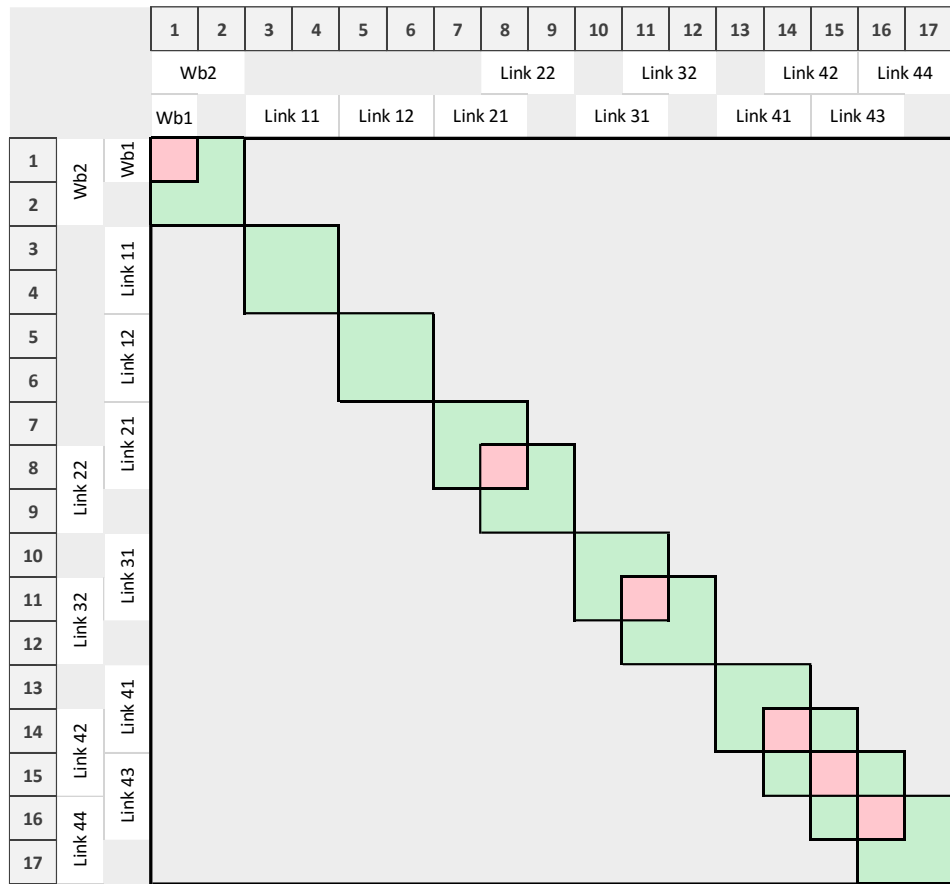


Figure 3.14 Construction of the total stiffness matrix \hat{K}_T of each leg.

Geometric constraints for the legs are derived from the orientation matrix. Matrix \hat{A}_{ij} is calculated using Equation 2.11, in which unit vectors in \bar{u}_1 - and \bar{u}_3 - direction are extracted from the rotation matrix of the node that is closer to the base on that specific joint. In Figure 3.16, boxes are color coded to indicate the two nodes that are linked by a specific joint. This figure shows the structure of matrix \hat{A}_T , which is a 30 by 102 matrix.

	Nodes																
	1	2	3	4	5	6	7	8	9	10	11	12	13	14	15	16	17
Joint 1	█		█														
Joint 2		█			█												
Joint 3				█			█										
Joint 4						█		█									
Joint 5									█	█							
Joint 6												█	█				

Figure 3.15 Construction of the overall \hat{A}_T matrix of a leg

Once these matrices are generated, they are combined in an overall stiffness matrix, \hat{K}_G . The general shape of this matrix is provided in Figure 3.17, which is parametrically given in Equation 2.14. The dimension of this matrix is 132 by 132. In Figure 3.17, gray areas show the zero matrices.

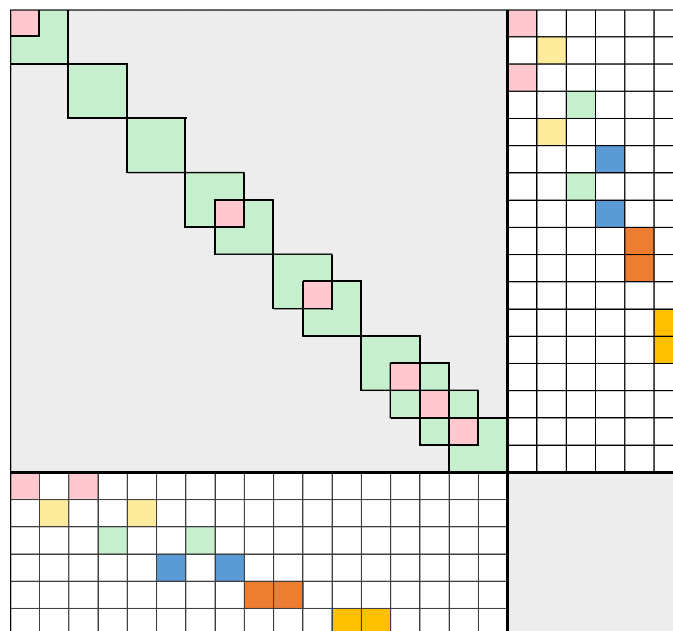


Figure 3.16 Global stiffness matrix, \hat{K}_G of HIPHAD.

To obtain the equivalent stiffness matrix for desired node on each leg, \hat{K}_G has to be multiplied with a permutation matrix, \hat{P} . This permutation matrix that is used for each leg is provided in Equation 3.66.

$$\hat{\mathbf{P}} = \begin{bmatrix} \hat{\mathbf{I}}_{(96,96)} & \hat{\mathbf{O}}_{(96,6)} & \hat{\mathbf{O}}_{(96,30)} \\ \hat{\mathbf{O}}_{(30,96)} & \hat{\mathbf{O}}_{(30,6)} & \hat{\mathbf{I}}_{(30,30)} \\ \hat{\mathbf{O}}_{(6,96)} & \hat{\mathbf{I}}_{(6,6)} & \hat{\mathbf{O}}_{(6,30)} \end{bmatrix} \quad (3.66)$$

As provided in Equation 2.19, $\hat{\mathbf{K}}_P$ is found using $\hat{\mathbf{K}}_G$ and $\hat{\mathbf{P}}$. Then equivalent stiffness matrix is calculated from Equation 2.25 and the result for this equation yields stiffness matrices $\hat{\mathbf{K}}_{eq}^{(1)}$, $\hat{\mathbf{K}}_{eq}^{(2)}$ and $\hat{\mathbf{K}}_{eq}^{(3)}$, which are equivalent stiffness matrices of each leg. Since this method includes large matrix operations, results are obtained semi-analytically.

Once these matrices are obtained, same procedure is followed for the mobile platform to combine the stiffness matrices of the legs. Calculations are derived from the model that is given in Figure 3.18. This figure shows the nodes of the equivalent links and the mobile platform. In this model, there are 7 nodes. Among these, nodes 4, 5, 6 and 7 define a rigid body.

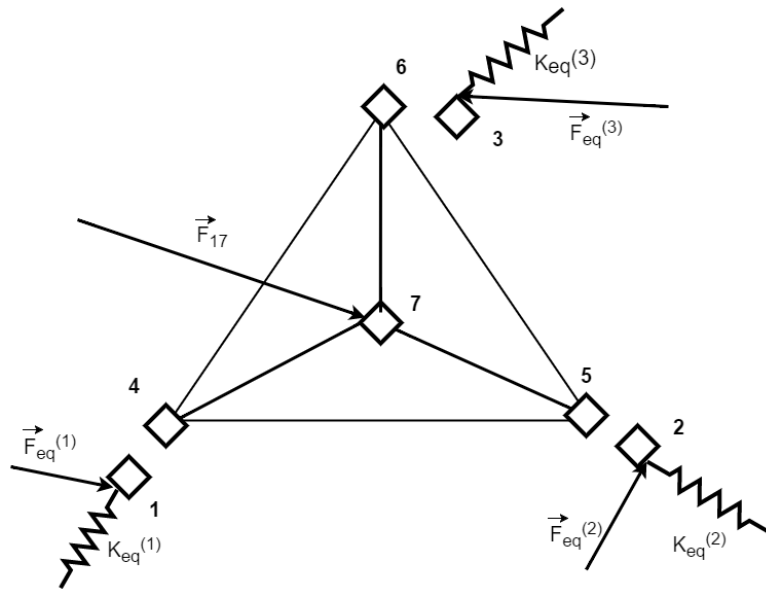


Figure 3.17 Equivalent stiffness model of the mobile platform

After the equivalent stiffness matrices and force vectors of the legs are calculated, these are assembled for the mobile platform using the model provided in Figure 3.18. Stiffness matrices of the legs are collected in the stiffness matrix represented in Equation 3.67.

$${}^w \mathbf{K}_T = \begin{bmatrix} \mathbf{K}_{eq}^{(1)} & \mathbf{0}_{(6,6)} & \mathbf{0}_{(6,6)} & \mathbf{0}_{(6,24)} \\ \mathbf{0}_{(6,6)} & \mathbf{K}_{eq}^{(2)} & \mathbf{0}_{(6,6)} & \mathbf{0}_{(6,24)} \\ \mathbf{0}_{(6,6)} & \mathbf{0}_{(6,6)} & \mathbf{K}_{eq}^{(3)} & \mathbf{0}_{(6,24)} \\ \mathbf{0}_{(24,6)} & \mathbf{0}_{(24,6)} & \mathbf{0}_{(24,6)} & \mathbf{0}_{(24,24)} \end{bmatrix} \quad (3.67)$$

The geometric constraints are included in the stiffness matrix as shown in Equation 3.68.

$${}^w \mathbf{A}_T = \begin{bmatrix} \mathbf{A}_{1,4} & \mathbf{0}_{(5,6)} & \mathbf{0}_{(5,6)} & -\mathbf{A}_{1,4} & \mathbf{0}_{(5,6)} & \mathbf{0}_{(5,6)} & \mathbf{0}_{(5,6)} \\ \mathbf{0}_{(5,6)} & \mathbf{A}_{2,5} & \mathbf{0}_{(5,6)} & \mathbf{0}_{(5,6)} & -\mathbf{A}_{2,5} & \mathbf{0}_{(5,6)} & \mathbf{0}_{(5,6)} \\ \mathbf{0}_{(5,6)} & \mathbf{0}_{(5,6)} & \mathbf{A}_{3,6} & \mathbf{0}_{(5,6)} & \mathbf{0}_{(5,6)} & -\mathbf{A}_{3,6} & \mathbf{0}_{(5,6)} \\ \mathbf{0}_{(5,6)} & \mathbf{0}_{(5,6)} & \mathbf{0}_{(5,6)} & \mathbf{B} & \mathbf{0}_{(5,6)} & \mathbf{0}_{(5,6)} & \mathbf{B}_{4,7} \\ \mathbf{0}_{(5,6)} & \mathbf{0}_{(5,6)} & \mathbf{0}_{(5,6)} & \mathbf{0}_{(5,6)} & \mathbf{B} & \mathbf{0}_{(5,6)} & \mathbf{B}_{5,7} \\ \mathbf{0}_{(5,6)} & \mathbf{0}_{(5,6)} & \mathbf{0}_{(5,6)} & \mathbf{0}_{(5,6)} & \mathbf{0}_{(5,6)} & \mathbf{B} & \mathbf{B}_{6,7} \end{bmatrix} \quad (3.68)$$

The matrices $\hat{\mathbf{K}}_T$ and $\hat{\mathbf{A}}_T$ are combined in a global stiffness matrix that is defined as $\hat{\mathbf{K}}_G$ that is formulated in Equation 3.69. The permutation operation is also applied for this stiffness matrix and formulation provided in Equation 2.25 is applied to yield the overall stiffness matrix of the haptic device. Results obtained from this method are provided in results section.

$$\hat{\mathbf{K}}_{G_{HIPHAD}} = \begin{bmatrix} \hat{\mathbf{K}}_T & \hat{\mathbf{A}}_T^T \\ \hat{\mathbf{A}}_T & \hat{\mathbf{0}}_{33,33} \end{bmatrix} \quad (3.69)$$

After the permutation of global stiffness matrix $\hat{\mathbf{K}}_{G_{HIPHAD}}$ for the mobile platform, equivalent stiffness matrix is calculated using the Equations 2.19 and 2.25.

3.7. Stiffness Calculation of HIPHAD Using VJM

Stiffness calculation of HIPHAD using VJM starts with defining the kinematic model of a leg first assuming that it is a serial kinematic chain. Another assumption is that the parallelogram is reduced into a two joint serial kinematic chain in which the two joints' motion is opposite to each other. This kinematic model is constructed from the links, active joints, passive joints and virtual joints. Although a robot link is defined by 6 DoF link model in VJM, in HIPHAD case, virtual joints are only used to represent compliant motion along the directions that the most deformation can occur. The model of 1st leg of HIPHAD is provided in Figure 3.19. $\vec{u}_3^{(2)}$, $\vec{u}_3^{(4)}$, $\vec{u}_3^{(7)}$, $\vec{u}_3^{(11)}$, $\vec{u}_3^{(12)}$ stand for the active and the passive joint axes. Other joints in this model are the virtual joints.

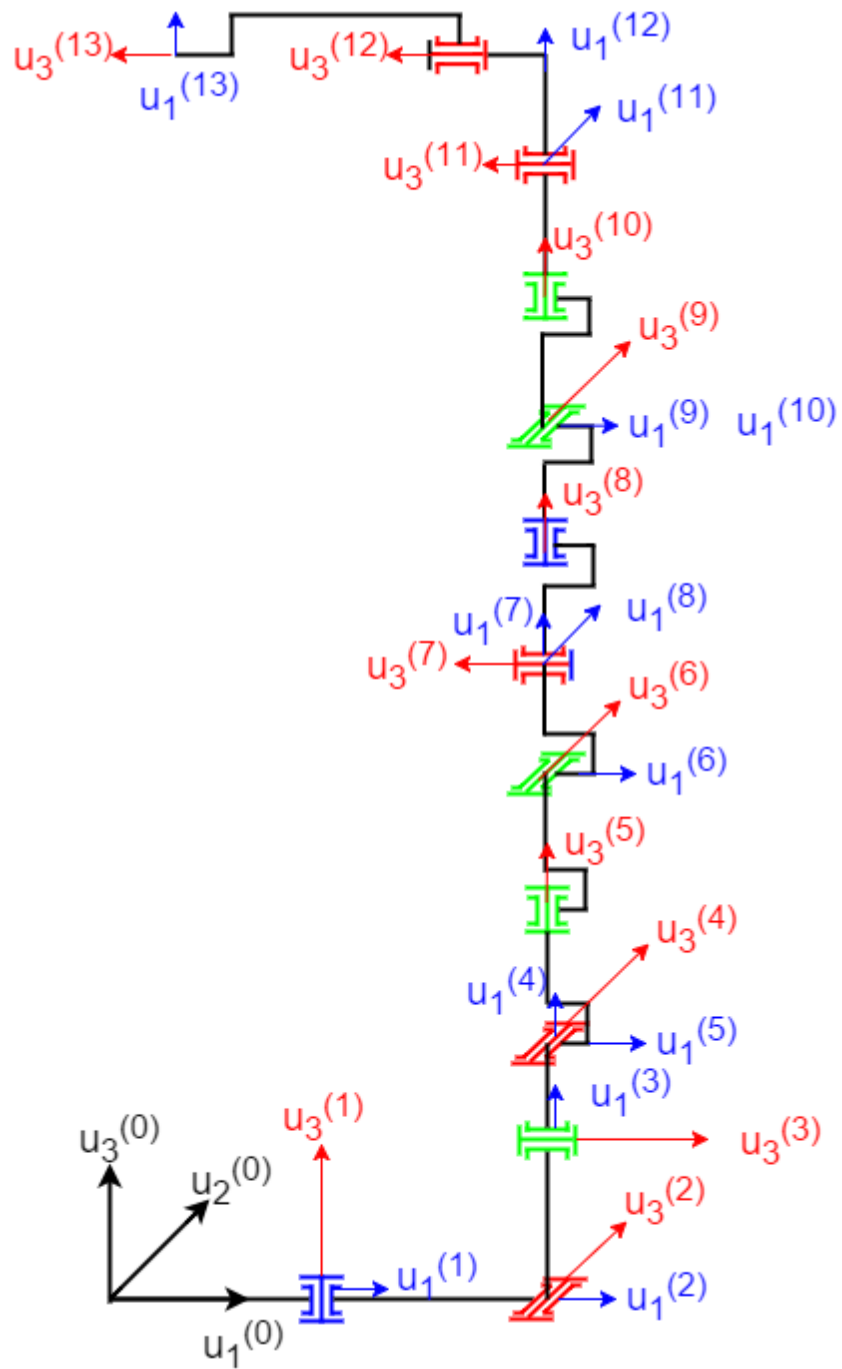


Figure 3.18 Kinematic model of leg 1 of HIPHAD.

Table 3.8 Denavit-Hartenberg(D-H) parameters of 1st leg's VJM model

	d	θ	a	α
1	0	0	Wb	0
2	0	θ ₂	0	-π/2
3	d2	θ ₃	l1	-π/2
4	0	θ ₄	0	π/2
5	0	θ ₅	0	π/2
6	l22	θ ₆	0	-π/2
7	0	θ ₇	0	π/2
8	0	θ ₈	0	π/2
9	l3	θ ₉	0	-π/2
10	0	θ ₁₀	0	π/2
11	0	θ ₁₁	0	-π/2
12	0	θ ₁₂	l4	0
13	0	θ ₁₃	0	0

Once the kinematic model is developed, the D-H parameters are found as shown in Table 3.8. Then, the position and orientation equations are written. Orientation and tip point position equation of leg 1 is written in Equations 3.70 and 3.71.

$$\begin{aligned} \hat{C}^{(0,13)} = & e^{\tilde{u}_3 \cdot \theta_2} \cdot e^{\tilde{u}_2 \cdot \theta_3} \cdot e^{\tilde{u}_3 \cdot \theta_4} \cdot e^{-\tilde{u}_2 \cdot \theta_5} \cdot \\ & e^{-\tilde{u}_3 \cdot \theta_6} \cdot e^{-\tilde{u}_2 \cdot \theta_7} \cdot e^{-\tilde{u}_3 \cdot \theta_8} \cdot e^{\tilde{u}_2 \cdot \theta_9} \cdot \\ & e^{-\tilde{u}_3 \cdot \theta_{10}} \cdot e^{\tilde{u}_2 \cdot \theta_{11}} \cdot e^{-\tilde{u}_3 \cdot \theta_{12}} \cdot e^{-\tilde{u}_3 \cdot \theta_{13}} \cdot e^{\tilde{u}_3 \cdot \pi} \end{aligned} \quad (3.70)$$

$$\begin{aligned} \vec{r} = & e^{\tilde{u}_3 \cdot \theta_2} \cdot e^{\tilde{u}_2 \cdot \theta_3} \cdot e^{\tilde{u}_3 \cdot \theta_4} \cdot e^{-\tilde{u}_2 \cdot \theta_5} \cdot \\ & e^{-\tilde{u}_3 \cdot \theta_6} \cdot e^{-\tilde{u}_2 \cdot \theta_7} \cdot e^{-\tilde{u}_3 \cdot \theta_8} \cdot e^{\tilde{u}_2 \cdot \theta_9} \cdot \\ & e^{-\tilde{u}_3 \cdot \theta_{10}} \cdot e^{\tilde{u}_2 \cdot \theta_{11}} \cdot e^{-\tilde{u}_3 \cdot \theta_{12}} \cdot e^{\tilde{u}_1 \cdot \pi} \cdot \begin{bmatrix} 0 \\ 0 \\ 1_4 \end{bmatrix} \end{aligned} \quad (3.71)$$

The formulations for \bar{r} and $\hat{C}^{(0,13)}$ are used to find the Jacobian matrix for both passive joints and active joints. It is done by using respective passive and virtual joint variables in calculating $\frac{\partial \bar{r}}{\partial \theta_i}$ and $\text{col}[\frac{\partial \hat{C}^{(0,13)}}{\partial \theta_i} \cdot \hat{C}^{(0,13)^T}]$, which results in velocity influence coefficients, \bar{J}_{r_i} and \bar{J}_{a_i} . In this calculation, due to the number of parameters, it is tedious to find the Jacobian matrix elements. For this reason, calculation of $\bar{J}_i^T = [\bar{J}_{r_i}^T \quad \bar{J}_{a_i}^T]$ is executed semi-analytically. Jacobian matrix for virtual joints are represented by J_θ and the Jacobian matrix for passive joints are represented by \bar{J}_q which are given in Equations 3.72 and 3.73.

$$\hat{J}_\theta = \begin{bmatrix} \bar{J}_{r_2} & \bar{J}_{r_4} & \bar{J}_{r_6} & \bar{J}_{r_7} & \bar{J}_{r_9} & \bar{J}_{r_{10}} & \bar{J}_{r_{11}} \\ \bar{J}_{a_2} & \bar{J}_{a_4} & \bar{J}_{a_6} & \bar{J}_{a_7} & \bar{J}_{a_9} & \bar{J}_{a_{10}} & \bar{J}_{a_{11}} \end{bmatrix} \quad (3.72)$$

$$\hat{J}_q = \begin{bmatrix} \bar{J}_{r_8} & \bar{J}_{r_{12}} \\ \bar{J}_{a_8} & \bar{J}_{a_{12}} \end{bmatrix} \quad (3.73)$$

Once the Jacobian matrices are calculated for each leg, then the matrix shown in Equation 3.73 is calculated, which includes the effect of passive joints into the mathematical model of stiffness calculation. In Equation 3.74, K_{c1} is the stiffness matrix of the respective leg, which the upper left 6x6 matrix.

$$\begin{bmatrix} K_{c1} & * \\ * & * \end{bmatrix} = \begin{bmatrix} \hat{J}_\theta \cdot K^{-1} \cdot \hat{J}_\theta^T & \hat{J}_q \\ \hat{J}_q^T & 0_{2,2} \end{bmatrix}^{-1} \quad (3.74)$$

In the calculation of stiffness matrices of the other two legs that are leg 2 and leg 3, the position vector and orientation matrix is rotated. Required rotations to find orientation matrix and position vector of their tip points are given in Equations 3.75 and 3.76.

$$\hat{\mathbf{R}}_2 = \begin{bmatrix} \cos(\pi/2) & -\sin(\pi/2) & 0 \\ \sin(\pi/2) & \cos(\pi/2) & 0 \\ 0 & 0 & 1 \end{bmatrix} \cdot \begin{bmatrix} 1 & 0 & 0 \\ 0 & \cos(\pi/2) & -\sin(\pi/2) \\ 0 & \sin(\pi/2) & \cos(\pi/2) \end{bmatrix} \quad (3.75)$$

$$\hat{\mathbf{R}}_3 = \begin{bmatrix} \cos(\pi/2) & -\sin(\pi/2) & 0 \\ \sin(\pi/2) & \cos(\pi/2) & 0 \\ 0 & 0 & 1 \end{bmatrix} \cdot \begin{bmatrix} \cos(\pi/2) & 0 & \sin(\pi/2) \\ 0 & 1 & 0 \\ -\sin(\pi/2) & 0 & \cos(\pi/2) \end{bmatrix} \quad (3.76)$$

Then same procedure is executed and stiffness matrices of the other two legs are calculated by using Equation 3.73. Since the legs tip points are defined on the same point of mobile platform, the stiffness matrices of legs are superposed (Pashkevich, Wenger & Chablat, 2007) as provided in Equation 3.77

$$\hat{\mathbf{K}}_{\text{HIPHAD}} = \hat{\mathbf{K}}_{C1} + \hat{\mathbf{K}}_{C2} + \hat{\mathbf{K}}_{C3} \quad (3.77)$$

CHAPTER 4

EXPERIMENTAL TEST SETUP

To verify the accuracy of stiffness matrix calculations, experimental tests are required to be conducted. In experimentation, calculated stiffness models are compared with the measured stiffness of the mechanism. Experimentation method is described in this chapter. The hardware and the software used in the experiments are listed in Table 4.1.

Table 4.1 Hardware and software list.

HARDWARE	SOFTWARE
PC	MATLAB© Simulink (High-level programming) Mathworks Inc.
Teledyne Dalsa Genie C1600	Quarc v2.1 Quanser©
HIPHAD	
QUARC Q8 DAQ Card	
Gigabit Ethernet Card	

During the experimentation, a computer is used as media for determining the position of the mobile platform of HIPHAD and allows a mapping of the displacement values. The indirect measurements of the mobile platform is achieved by acquiring the encoder signals via QUARC Q8 DAQ Card. The computer is also used as a media for acquiring image information Teledyne Dalsa Genie C1600 cameras to be later processed for direct measurement of the mobile platform. The streamline for carrying out direct measurement of the mobile platform position is as follows: the acquired raw images are taken via Gigabit Ethernet card (GigE) and are processed in Matlab environment.

In this experiments, stereo cameras are used for direct (absolute) measurement of the mobile platform postion. Therefore, the accuracy of the experimentation depends on

an appropriate selection of these cameras. The parameters influencing the selection process are sensor size, working distance, field of view and focal length. These parameters are explained in Figure 4.1. Among these parameters, the field of view for this experimentation was selected as 130 mm by 130 mm square surface for both cameras, which is enough to cover the total workspace of the mechanism to be acquired from the mobile platform position.

Sensor size of the camera is 5.28x7.04 mm. The lenses used in the cameras are FUJINON HF16HA-1B that has 16 mm focal length. With this camera lens composition, smallest feature that can be detected by cameras is 0.165 mm calculated for the camera axis that has 1600 pixels. Table 4.2 gives the smallest feature that can be detected along with the given camera and working distance combinations.

Table 4.2 Camera Parameters

Field of View (mm)	Working Distance (mm)	Focal Length (mm)	Sensor Size (mm)	Pixel Size (mm)	Smallest Feature (mm)
130	393.9394	16	5.28	0.0044	0.216667
130	295.4545	16	7.04		0.1625

To increase measurement accuracy and precision, sub-pixel interpolation is implemented in the image processing algorithm. Therefore, the smallest feature that can be detected by the cameras needs to be recalculated. To accommodate this calculation, radius of 4 circles with different radii are measured. The selected diameter of the circles are 3.03, 3.08, 3.5, 4 mm. The diameter of circle with 3.03 mm diameter is measured 20 times with the cameras and average of this measurement came out to be 68.2289 pixels with a standard deviation of $\sigma=0.0277$. For the circle having 3.08 mm diameter, image processing algorithm resulted in 70.2525 pixels for average diameter measurement with a standard deviation of $\sigma=0.0798251$. As a result, cameras along with the developed image processing algorithm found to be capable of measuring 0.025 mm with 1 pixel. The other two circles were used to verify this result.

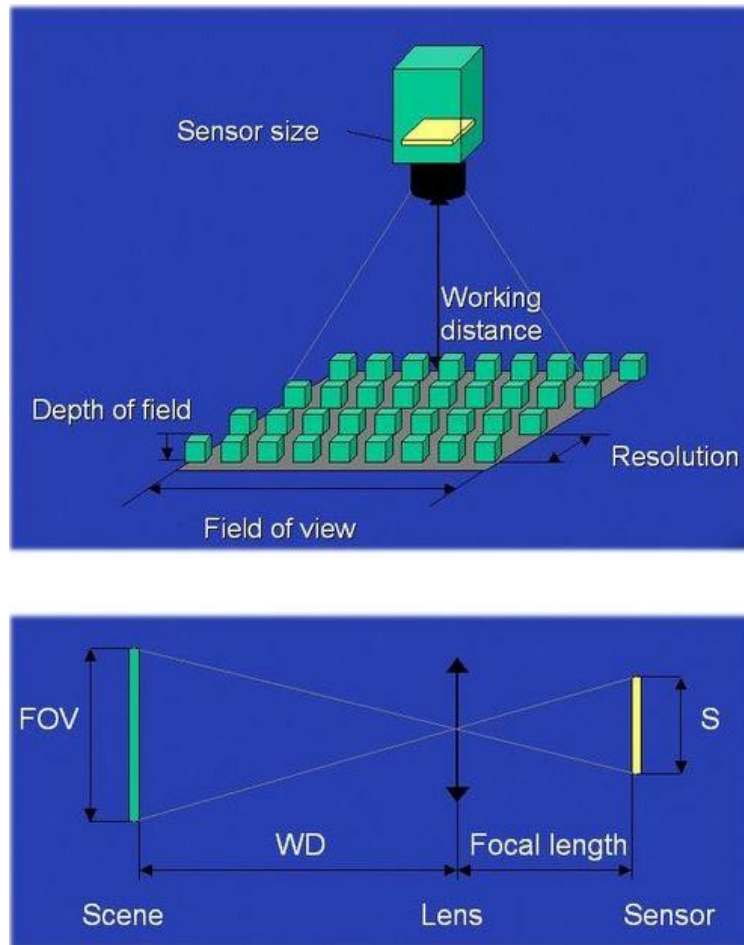


Figure 4.1 Parameters affecting the selection of cameras for machine vision
 (Source: Calculating Camera Sensor Resolution and Lens Focal Length,
 27.06.2014, <http://digital.ni.com/>)

Throughout the experiments, some external forcing is applied on HIPHAD. This forcing deforms the mechanism of HIPHAD. However, not only the mechanism but the basement for the haptic device deformed and vibrated during the experimentation. Experiencing these effects during tests alters the real deformations and this leads to a decreased accuracy in experimentation. For this reason, a test rig is constructed using Aluminum sigma profiles, which is denoted with 2 in Figure 4.2, and a basement block is manufactured by precise machining to add more weight to the test rig for stable and accurate operation is denoted by 1 in Figure 4.2. When the HIPHAD mechanism is mounted on the basement block, it also ensures the orthogonality of the HIPHAD with respect to the coordinates of cameras. The cameras are also attached to this basement

construction, which absorbs the vibration and allows taking snapshots with reduced blurring effect.

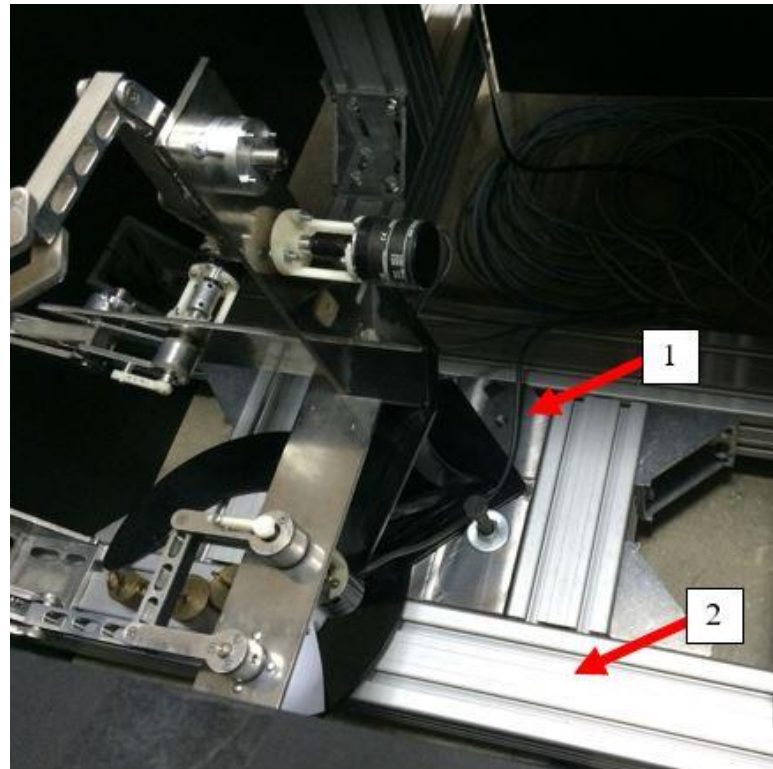


Figure 4.2 Experimentation basement.

To conduct this experimentation, HIPHAD is also modified. This modification includes the removal of the actuators of the haptic device and substituting a brake for in their places. By this way, compliance of the actuators are eliminated and only the mechanism's compliance is measured. This brake is shown in Figure 4.3. The brakes are working simply by fastening two screws to the brake to apply enough pressure on the actuation shaft in order to maintain its angular position. The actuation shaft and braking screw on a brake assembly are provided in Figure 4.3 with 1 and 2, respectively.

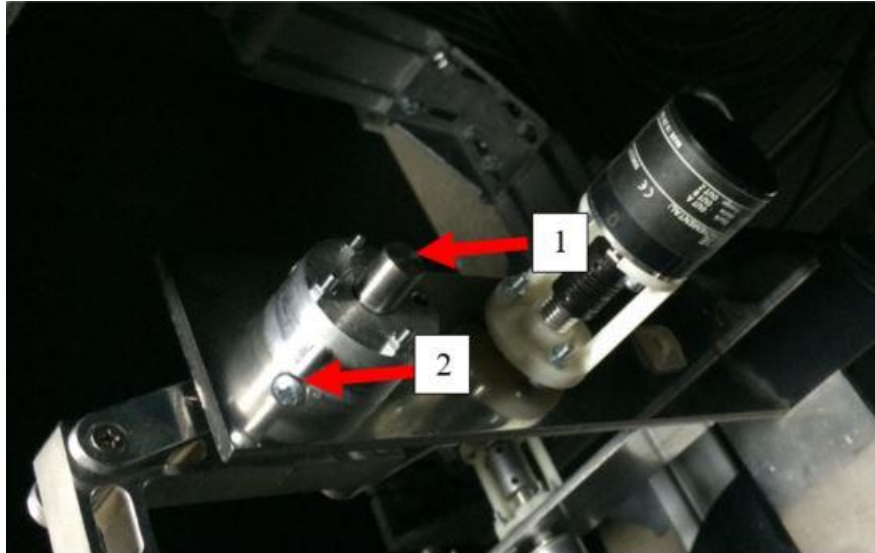


Figure 4.3 Brake replacement for the actuators

For increasing accuracy and repeatability of the measurements, the illumination is provided by led arrays that are placed on the black wall shown in Figure 4.5. Experimental setup is composed of a closed black room covering the surrounding of the test rig, mechanism, cameras, and light sources. Complete experimentation setup is presented in Figure 4.5. HIPHAD, QUANSER Q8 DAQ card, PC for taking sensor signals for calculating position information, PC for processing images for stereo measurements, walls of the dark room, led strays and camera looking towards plane 23 are denoted in Figure 4.4 with numbers from 1 to 8, respectively.

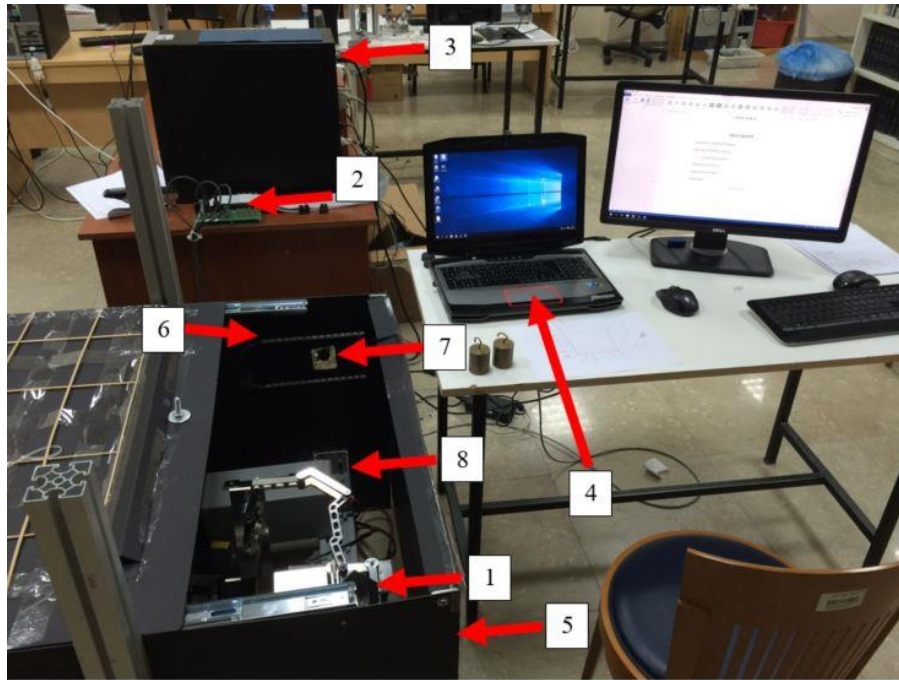


Figure 4.4 Complete experimentation setup

The experiments are carried out by first determining the nodes to be used for measuring compliant displacements under some load. The cubic workspace of the mechanism defined for the motion of the wrist point is divided into equal three parts on each side of the cube resulting in 27 measurement nodes.

To settle the wrist point of the HIPHAD on this specified positions, the encoders are used. After the calibration process that is explained in Section 3.5, kinematics is used to move the wrist point to a specified node. Once the HIPHAD is positioned on the node, the image acquisition process is initiated. For this operation, a GigE camera object is created in Matlab script that allows frame transfer from camera to Matlab. At this stage, 2 images are acquired which are taken before and after the force along the direction of measurement is applied on the mobile platform of HIPHAD. This testing procedure is schematically explained in Figure 4.5, in which numbers denote the sequence of the stages. The sequence from 1 to 6 in Figure 4.5 is as follows: (1) measurement of the mobile platform's indirect position measurement using encoders and acquiring via Quanser Q8 DAQ card, (2) position calculation of mobile platform to settle mobile platform on the designated node, (3) image acquisition of the mobile platform without external forces, (4) application of external forces on the mobile platform by calibrated

weights, (5) image acquisition of the mobile platform under external forces, (6) image processing and compliant displacement calculation.

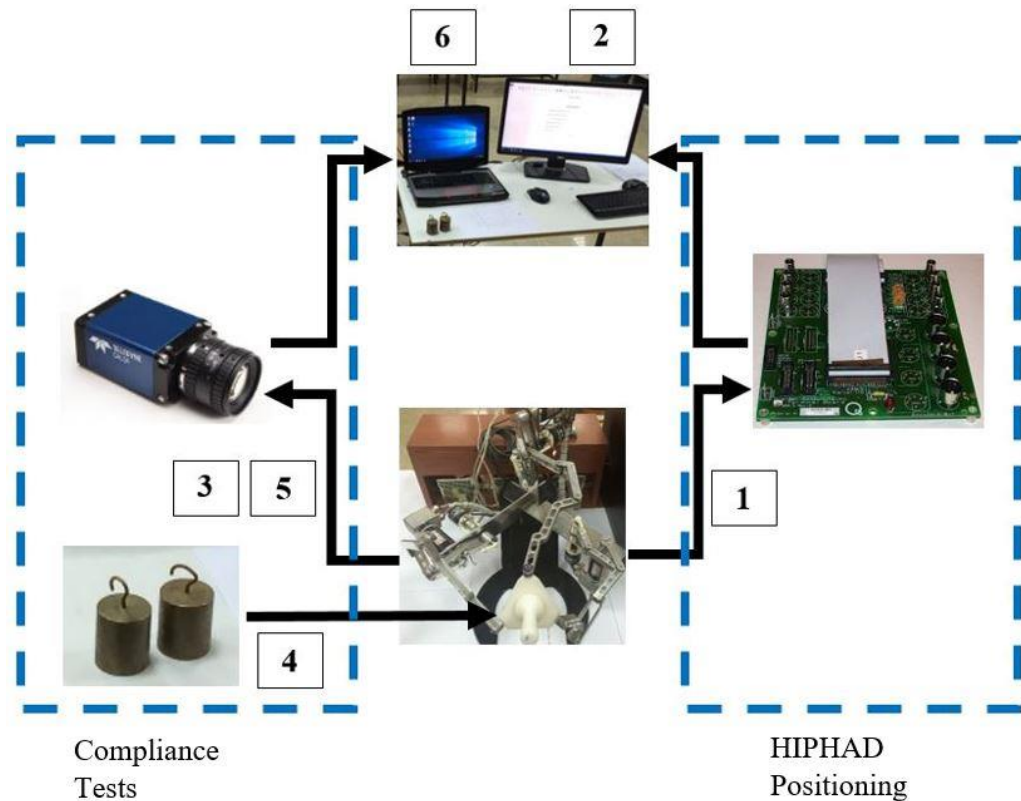


Figure 4.5 Experimentation stages

After image acquisition, these images are processed by high pass filter and converted to a binary image. Following that, a blob analysis is applied on this binary image that is extracted from the raw image and measurement of the tracking object is carried out in camera coordinates. The camera coordinates are represented in Figure 4.6 with black arrows. The coordinate system has its x-direction aligned with the world coordinate that is given with red arrows. The y-direction of camera coordinate system, however, is in the opposite direction of the z-axis of the world coordinate system.

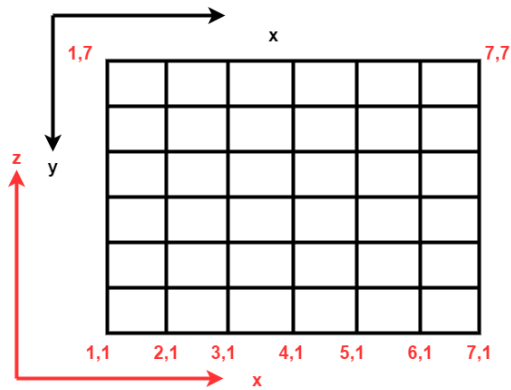


Figure 4.6 Meshes applied on the image plane

The tracking image is composed of 4 circles having different diameters placed on a white background. Differences in circle diameters allow the measuring algorithm to detect the four circles. This is important for calibrating each measurement by itself using long and short sides of the rectangle defined among the centers of these circles and following a circle precisely. Otherwise, blob analysis algorithm might select a circle randomly and this gives false results. Once the algorithm detects each circle, it tracks it between 2 images that are taken for 2 cases, which are the one without external forces and the one under external forces.

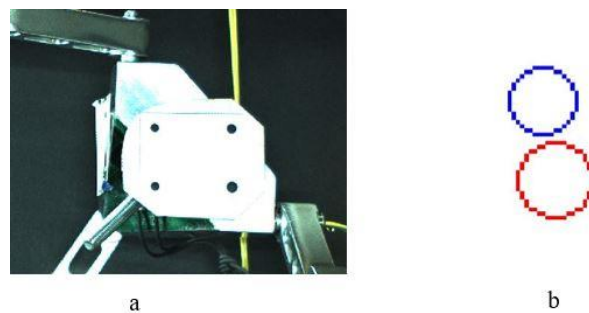


Figure 4.7 (a) Tracking patterns having 4 different circles. (b) Result of pattern tracking

These two images are taken for the same node. Once these two images are tracked by the algorithm the compliant displacement of the wrist point is illustrated as provided in Figure 4.7 (b). Blue and red circles display the initial and final positions of the tracked pattern, respectively. In this measurement technique, measurement performance is increased by applying sub-pixel interpolation and image filtering such as a 2D median filter. To illustrate the efficiency of image processing techniques employed in this work, a non-interpolated and non-filtered measurement result and the resultant image that is

created after the image processing techniques are applied are shown in Figure 4.8 (a), (b), respectively.

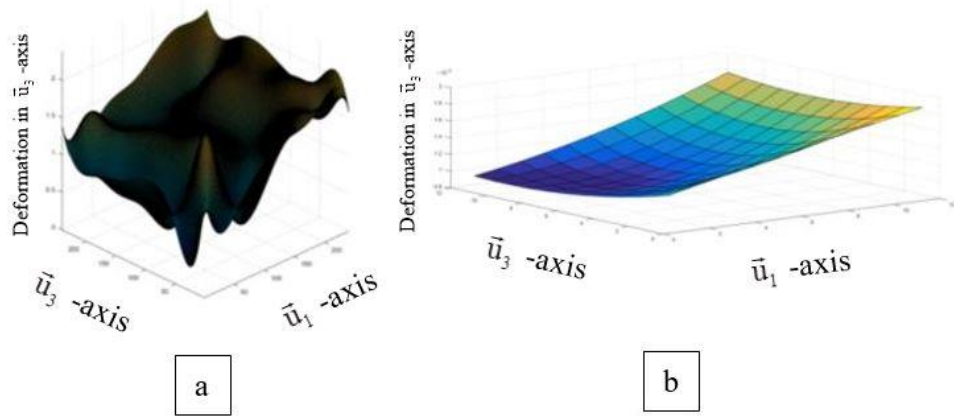


Figure 4.8 (a) Non-interpolated and non-filtered measurement result. (b) Sub-pixel Interpolated and filtered measurement result.

CHAPTER 5

RESULTS

Calculation of stiffness model of HIPHAD haptic device is studied by using 2 semi-analytical methods. The results of these calculations are evaluated by comparing them to the compliance of HIPHAD acquired from the experimentation throughout its workspace. It should be noted that actuated joints of each leg are fixed at a position by brakes and experimentation is carried out without the inclusion of the actuator compliances. The cubic workspace of the manipulator is sliced into 8 cubes with equal lengths. Measurements are carried out at each corner of these cubes. In Figure 5.1, the color coded dots indicate the nodes in which the compliant displacement measurements are done. Nodes are placed along each axis with equal distances from each other so that the first node is placed on 160th, the second node is placed on the 220th and the third node is placed on 280th mm away from the world frame that is provided in Figure 5.1 with black color.

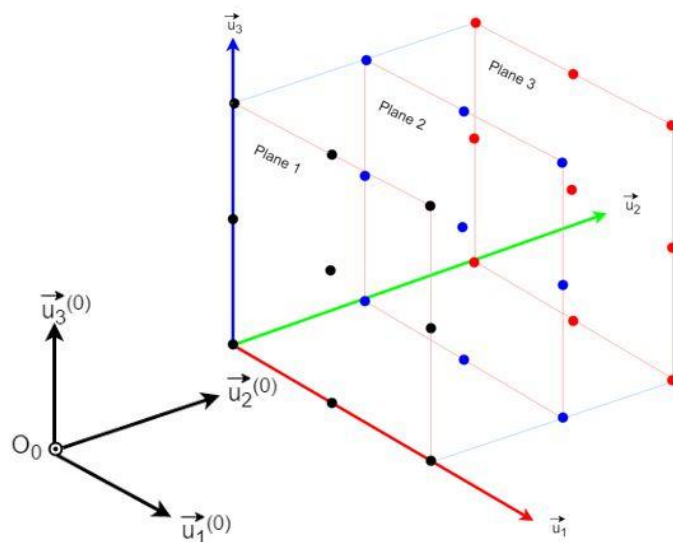


Figure 5.1 Placement of the nodes for experimentation.

Initially, various external forces along \bar{u}_3 -axis are applied on the mobile platform of HIPHAD at the position (220,220,220) and they are listed in Table 5.1. When the actuated joint of the HIPHAD is fixed rigidly, the displacements of the mobile platform with respect to the applied forces are shown in Figure 5.2. The displacement graph of HIPHAD shows a linear trend along all axes. The compliant displacements along x and y are due to the deformation of the base platform and this resulting applied force to have components along these directions.

Table 5.1 External forces resulting in displacements given in Figure 5.2.

Forcing, N			
-0,981 z-axis	-1.962 z-axis	-4.905 z-axis	-6,867 z-axis

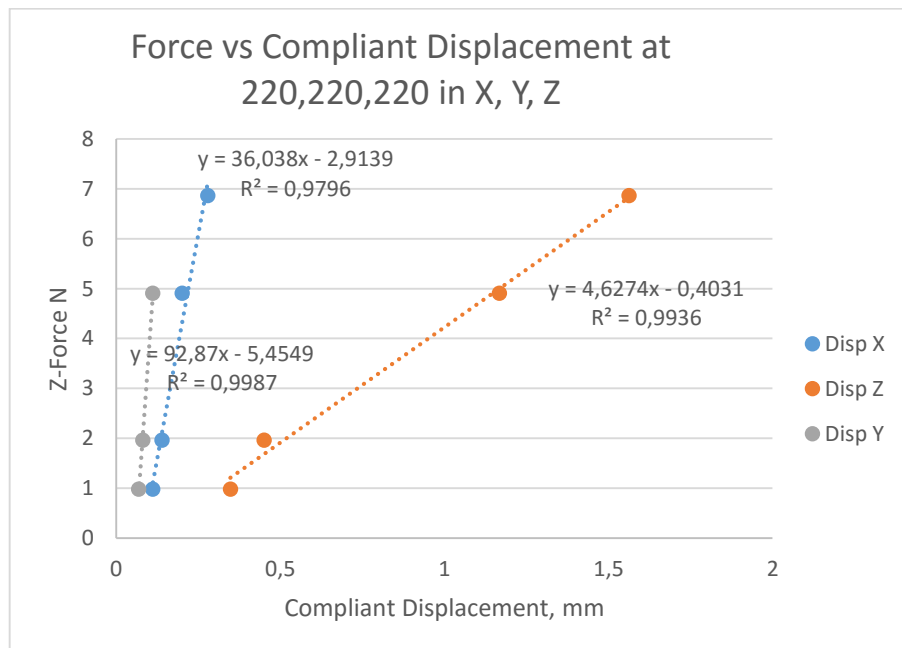


Figure 5.2 Force vs Compliant Displacement at (220,220,220).

This test is carried out to find the joint stiffness values that are not known and can only be found experimentally. The procedure is outlined in Figure 5.3. In HIPHAD case, compliant deformations are calculated in VJM by modelling only the links as flexible bodies. After obtaining the test result for compliant displacements, the compliant displacement calculated using the VJM model is subtracted from the measured

deformations and resultant vector \bar{C}_d is accepted to be the compliant displacement due to the joint stiffness values. Then a model is formulated for the compliance resulting from the joint stiffness values and equated to the compliance difference, \bar{C}_d . This model is the simplified stiffness model of HIPHAD and it includes only the joint stiffness values. The model is valid under some assumptions: (1) In this experimentation force is applied on negative z axis therefore, stiffness model of HIPHAD is formulated only using third leg, (2) this leg is assumed to be a fully actuated serial kinematic chain, (3) stiffness values of 6th and 7th joints are assumed to be equal to the 10th and 11th joints. By this way Equation 5.1 can be decomposed to 3 scalar equations with unknowns K_{04} , K_{06} and K_{07} . These joint stiffness values are used in VJM to model joint compliances of passive joints.

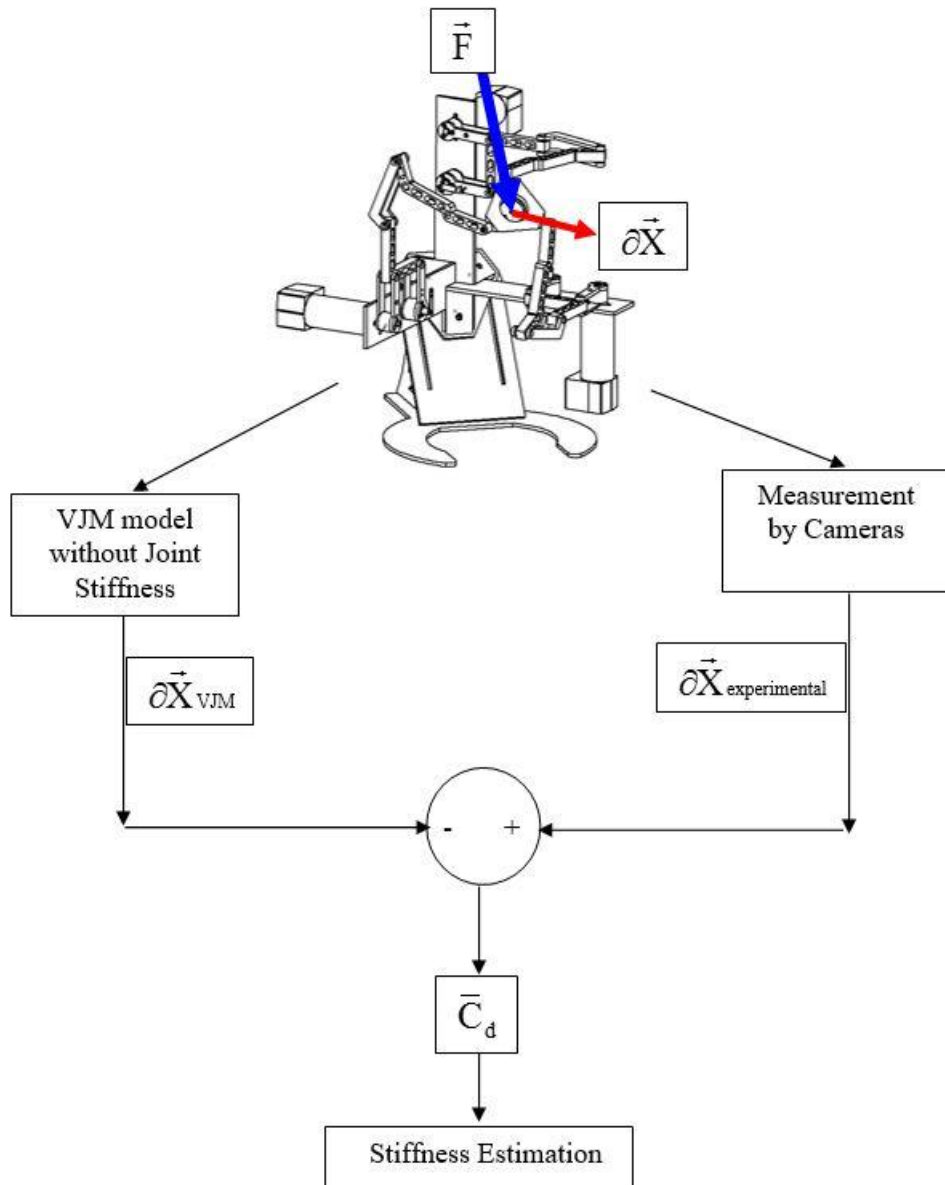


Figure 5.3 Procedure of joint stiffness estimation

Joint stiffness values of KQ4, KQ6, KQ7, KQ10 and KQ11 are found using the formulation described in Equation 5.1. The formulation yields the joint stiffness values for KQ4, KQ6, KQ7, KQ10 and KQ11 to be at 11.0974, 99.25, 99.25, 99.25 and 99.25 rad/Nm, respectively.

$$\begin{bmatrix} 0 \\ 0 \\ C_{dz} \end{bmatrix} = \begin{bmatrix} \bar{J}_4 & \bar{J}_6 & \bar{J}_7 & \bar{J}_{10} & \bar{J}_{11} \end{bmatrix} \cdot \begin{bmatrix} K\theta_4 & 0 & 0 & 0 & 0 \\ 0 & K\theta_6 & 0 & 0 & 0 \\ 0 & 0 & K\theta_7 & 0 & 0 \\ 0 & 0 & 0 & K\theta_{10} & 0 \\ 0 & 0 & 0 & 0 & K\theta_{11} \end{bmatrix} \cdot \begin{bmatrix} \bar{J}_4^T \\ \bar{J}_6^T \\ \bar{J}_7^T \\ \bar{J}_{10}^T \\ \bar{J}_{11}^T \end{bmatrix} \cdot \begin{bmatrix} 0 \\ 0 \\ F_z \end{bmatrix} \quad (5.1)$$

5.1. Experimental Results

In this section, compliant displacement measurements are carried out when forces are applied along the Cartesian frame axes. The force along each axis is provided by pulling the mobile platform by hanging a 700 g of weight that is passing through a plate which changes the direction of the force. The weight provides forces in positive directions with respect to the world frame along \bar{u}_1 - and \bar{u}_2 -axes. However, along \bar{u}_3 -axis, the force created by the weight is in the negative direction of the \bar{u}_3 -axis. The compliant displacements are measured at each node presented in Figure 4.6. It should be noted that the compliant displacement measurements at 9 nodes, which are on the same plane, are used in an interpolation algorithm to estimate the compliant displacement values in between the nodes. The compliant displacements throughout the planes of measurement are plotted in the figures below.

Test results for compliant displacement along the \bar{u}_1 -direction on plane 1 (described in Figure 5.1) yields the results provided in Figure 5.4. In this figure, displacement values range between 1.75 and 0.7 mm. The maximum displacement on this plane is found on node defined at N(160,280), which is 1.72 mm and minimum displacement is measured at node N(160,160) that is 0.84 mm in (+) \bar{u}_1 -direction. The surface plot shows an increase in the displacement values on the nodes defined at the workspace boundary along \bar{u}_3 -axis. On the left and right bottom corners, HIPHAD gives the lowest compliant displacements and on the top corners, it gives the highest ones. In the middle ranges of \bar{u}_1 direction, HIPHAD has lower compliances through all levels along \bar{u}_3 -axis. The stiffness variations through the plot indicate that for plane 1, HIPHAD has a greater stiffness at the bottom corners and less stiffness at the top corners. This is a

result of increasing moment arm due to the extension of HIPHAD. This moment arm is defined between wrist point W_r and the tip point of the parallelogram W_p , which means that any increase of distance in between these points results in an increase of HIPHAD compliance.

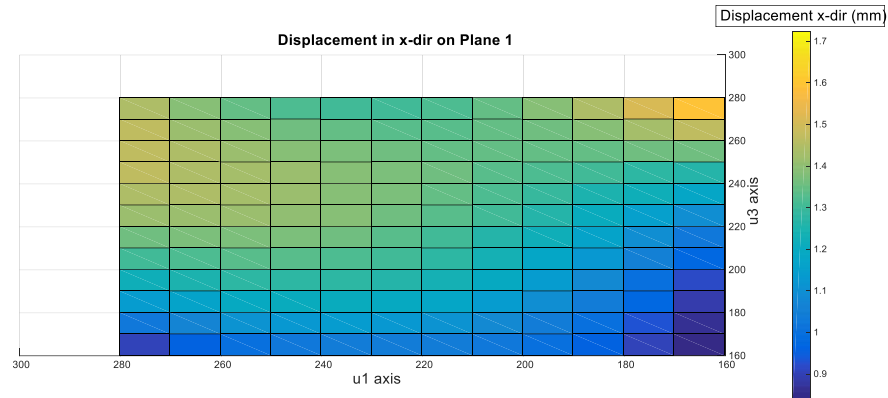


Figure 5.4 Compliant displacement values of HIPHAD in \vec{u}_1 -axis on Plane 1.

On Plane 2, the compliant displacement values are measured and interpolated as given in Figure 5.5. Maximum and minimum displacement values on this plane are found on the nodes defined at $N(280,280)$ and $N(210,160)$, which are 2.56 and 1.33 mm, respectively. As it was the case for the 1st plane, the compliant displacement values measured for the 2nd plane show an increasing trend towards the workspace boundary along \vec{u}_3 -axis. The arc having dark blue to green colors shows that HIPHAD has a greater stiffness in the middle for all levels along \vec{u}_3 -axis. The dark blue area in the middle is a result of the distance between wrist point, W_r , and W_p becoming the smallest at that node. For Plane 2, distance between W_r and W_p decreases as mobile platform is moved from 160 mm to 220 mm along \vec{u}_1 -axis. After 220th mm, compliant displacement map of HIPHAD becomes the mirror of the previous part.

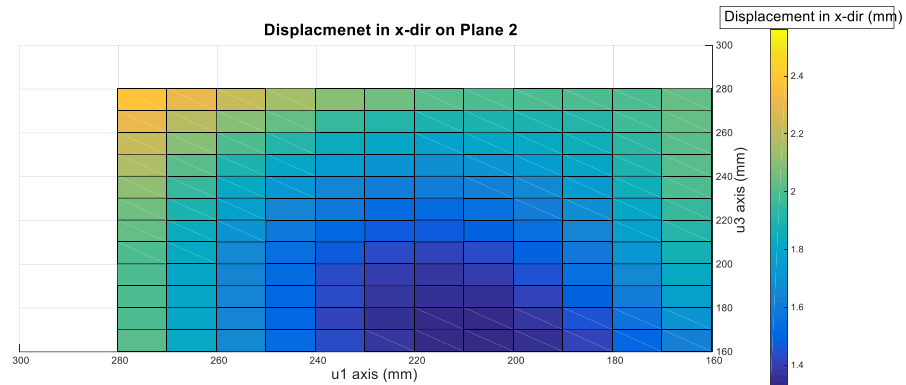


Figure 5.5 Compliant displacement values of HIPHAD in \vec{u}_1 -axis on Plane 2.

Figure 5.6 is plotted according to the data acquired on Plane 3. For this measurement set, maximum and minimum values of compliant displacements are measured on nodes N(280,280) and N(210,160), which came out to be 3.442 and 1.630 mm, respectively. On this plane, HIPHAD's mobile platform experience larger compliant displacements and shows the similar trend with the plane 2 in terms of having an arc of minimum compliance in the middle of the \vec{u}_1 -axis. Another similarity between the measurements on all planes is that the compliant displacements are increased towards the outer boundary of the workspace along \vec{u}_3 -axis. This is a confirmation of the previously described observations for compliant displacement along \vec{u}_1 -axis. Plane 3 is located at the extended boundary of the workspace along \vec{u}_2 -axis and as a result of this, the distance between the W_r and W_p increases with respect to the previous planes, which result in largest compliant displacement values measured on this plane.

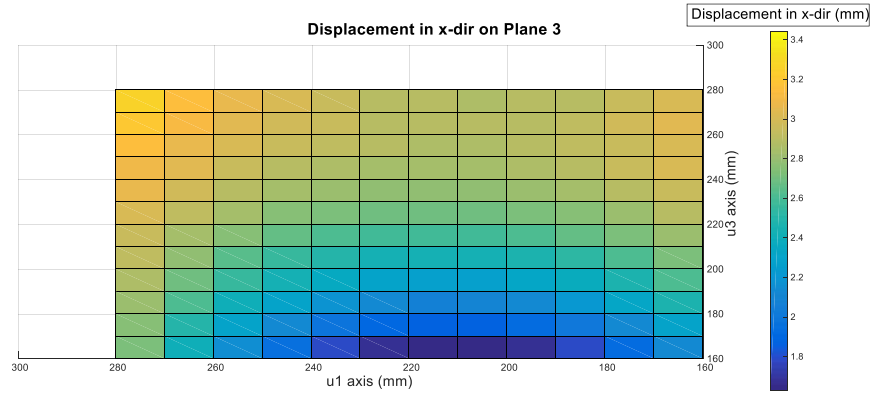


Figure 5.6 Compliant displacement values of HIPHAD in \vec{u}_1 -axis on Plane 3.

To provide better visualization of HIPHAD compliance map, in between the nodes that measurements are received, interpolation is carried out for the whole workspace. It can be observed from Figure 5.7 that HIPHAD shows an increasing compliance (or decreasing stiffness) values when the mobile platform is moved from the fully folded position at 160, 160 and 160 mm to fully extended position at 280, 280 and 280 mm along \vec{u}_1 , \vec{u}_2 and \vec{u}_3 directions respectively.

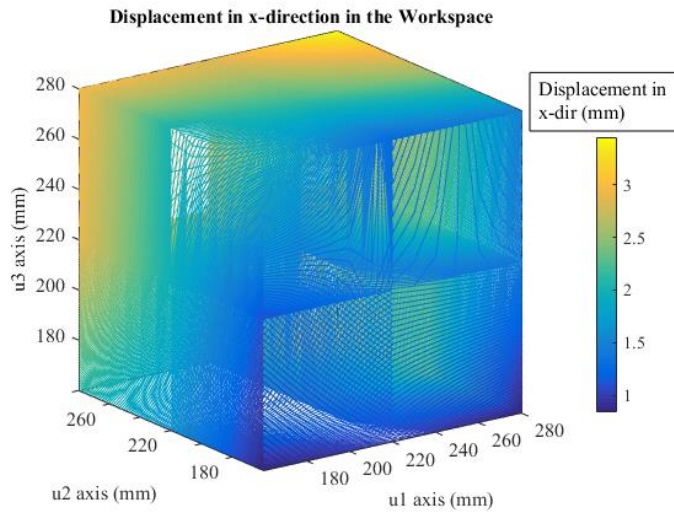


Figure 5.7 Compliant displacement of the HIPHAD under 700 g of force along (+) \vec{u}_1 -axis throughout its workspace.

Test results for compliant displacement in the \vec{u}_2 -direction on plane 1 yields the results provided in Figure 5.8. In this figure, displacement values measured between

2.490 and 0.7903 mm. The maximum displacement on this plane is found on node defined at N(220,160,280), which is 2.490 mm and minimum displacement is measured at node N(160,160,160) that is 0.7903 mm in (+) \vec{u}_2 -direction. The surface plot shows an increase in the displacement values on the nodes defined at the workspace boundary along \vec{u}_3 -axis. On the right bottom corner, HIPHAD gives the lowest displacement and along \vec{u}_1 axis compliance displacement of HIPHAD increases. On the top corners, it gives the highest displacement values. The stiffness change through the plot shows that for this plane HIPHAD has a greater stiffness on the right bottom corner and less stiffness on the top edge of the workspace.

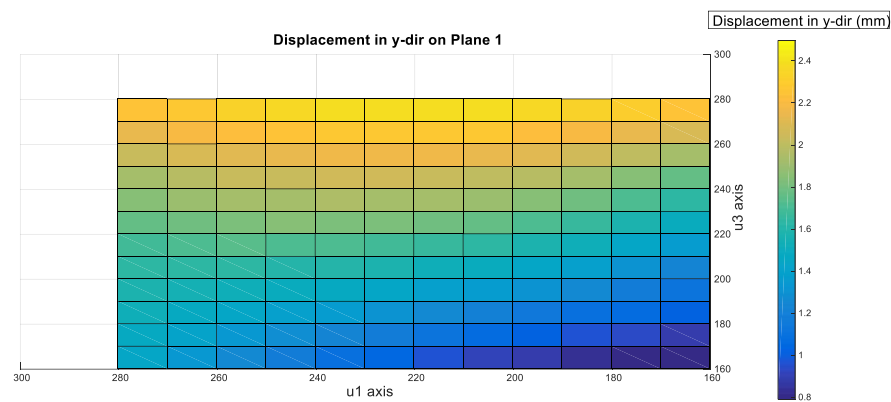


Figure 5.8 Compliant displacement values of HIPHAD in \vec{u}_2 -direction on Plane 1.

HIPHAD gives the displacement values on Plane 2 as provided in Figure 5.9. Maximum and minimum displacement values on this plane are given on the nodes defined at N(160,220,280) and N(210,220,280) which are 2.491 and 0.6752 mm, respectively. As it was the case for the 1st plane, the compliant displacement values measured for the 2nd plane show an increasing trend towards the workspace boundary along \vec{u}_3 -axis. The dark blue region compressed towards the bottom edge of the workspace shows that HIPHAD has a greater stiffness. This region corresponds to the region where the parallelogram is moving. In this region difference between W_r and W_p gets the smallest values. For Plane 2, distance between W_r and W_p decreases as mobile platform is moved from 160 mm to 220 mm along \vec{u}_3 -axis.

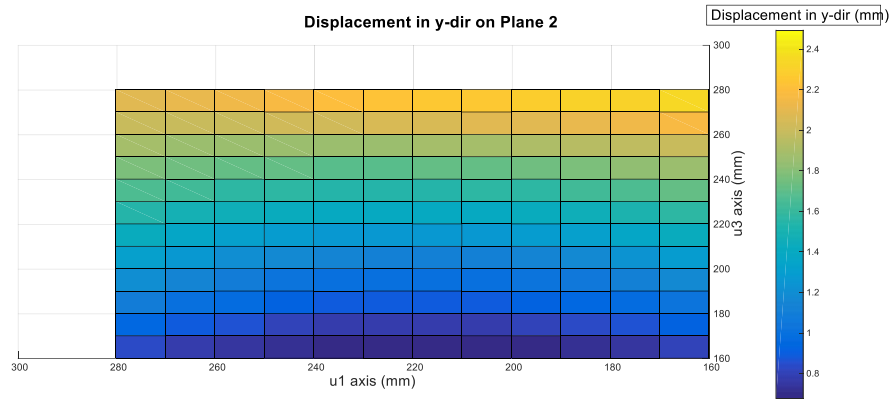


Figure 5.9 Compliant displacement values of HIPHAD in \vec{u}_2 -direction on Plane 2.

Displacement values measured on Plane 3 are provided in Figure 5.10. Maximum and minimum displacement values on this plane are given on the nodes defined at N(280,280,250) and N(160,160,280) which are 1.693 and 0.5095 mm, respectively. Likewise, the 1st and 2nd planes, displacement values measured for 3rd plane show an increasing trend for higher \vec{u}_3 values. The arc, having dark blue color shows that HIPHAD has a greater stiffness on the nodes defined at the workspace boundary along \vec{u}_1 -axis. Compared to Plane 2, compliant displacements of HIPHAD becomes smaller on this plane. The displacement trend represented for previous planes of the same direction of compliance displacement is also given for Plane 3 that is greater stiffness values are observed on the edge along \vec{u}_1 -axis.

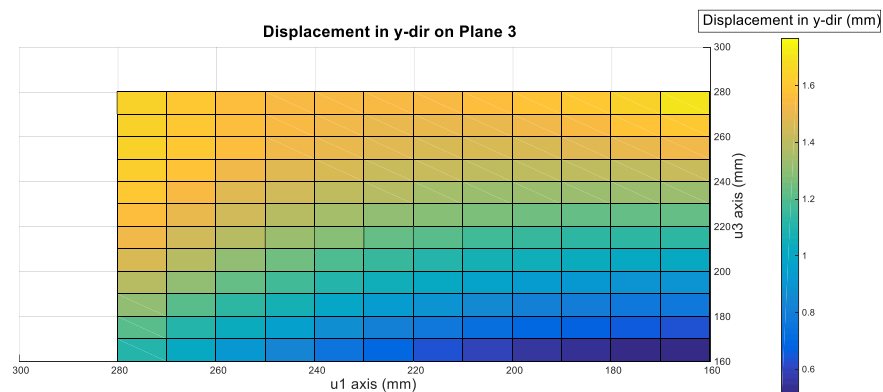


Figure 5.10 Compliant displacement values of HIPHAD in \vec{u}_2 -direction on Plane 2.

Visualization of HIPHAD compliance throughout its workspace is provided in Figure 5.11. HIPHAD shows an increasing compliance or decreasing stiffness values when the mobile platform is moved from 160 to 280 mm in \vec{u}_2 direction. It is clear that compliance of HIPHAD depends more on the displacement of the mobile platform in \vec{u}_1 and \vec{u}_3 directions.

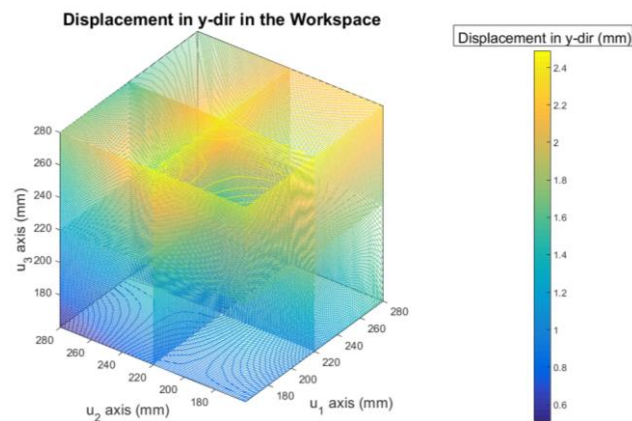


Figure 5.11 Compliance displacement of the HIPHAD under 700 g forcing along $(+)\vec{u}_2$ -direction throughout its workspace.

Test results for compliant displacement in the \vec{u}_3 -direction on plane 1 yields the results provided in Figure 5.12. The maximum displacement on this plane is found on node defined at N(230,160,220), which is -0.323 mm and minimum displacement is measured at node N(230,160,160) that is -0.020 mm in \vec{u}_3 -direction. The surface plot shows an increase in the displacement values on the nodes defined at the workspace boundary along \vec{u}_1 -axis, however, compared to the previous plots provided for other two axes, this plot does not show a clear trend for compliance. The displacement values are denoting a close change on the plane. Along \vec{u}_1 axis, the compliance of HIPHAD increases in a region that narrows in the middle of \vec{u}_1 axis then spreads on the edge of the plane.

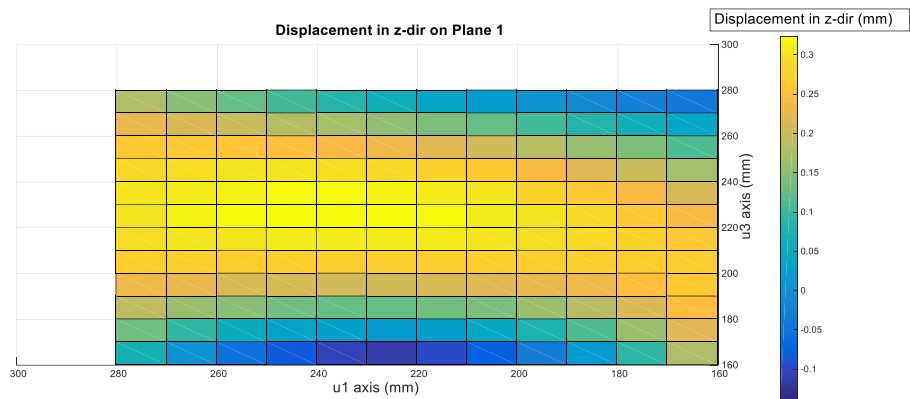


Figure 5.12 Compliant displacement values of HIPHAD in \vec{u}_3 -direction on Plane 1.

Test results for compliant displacement in the \vec{u}_3 -direction on plane 2 yields the results provided in Figure 5.13. The maximum displacement on this plane is found on node defined at N(280, 220,280), which is -3.181 mm and minimum displacement is measured at node N(160,220,220) that is -1.234 mm in \vec{u}_3 -direction. The surface plot shows an increase in the displacement values on the nodes defined at the workspace boundary along \vec{u}_1 -axis. The arc-shaped increase in compliance of HIPHAD happens here for the \vec{u}_3 -axis but propagates along \vec{u}_1 axis.

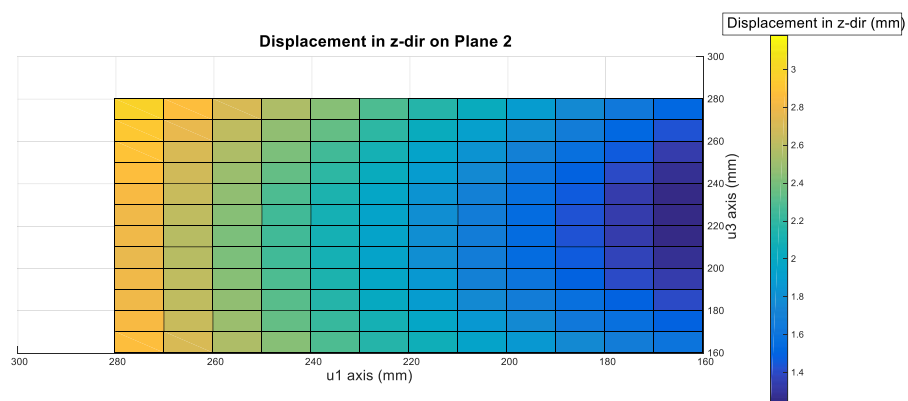


Figure 5.13 Compliant displacement values of HIPHAD in \vec{u}_3 -direction on Plane 2.

Displacement values measured on Plane 3 are provided in Figure 5.14. Maximum and minimum displacement values on this plane are given on the nodes defined at N(280,280,160) and N(160, 280,210) which are -3.499 and -1.618 mm along \vec{u}_3 -axis. The surface plot shows an increase in the displacement values on the nodes defined at the workspace boundary along \vec{u}_1 -axis. The arc-shaped increase in compliance of HIPHAD happens here for the \vec{u}_3 -axis but propagates along \vec{u}_1 axis. Likewise, the 2nd plane, displacement values measured for 3rd plane show an increasing trend at the nodes defined towards the edge of the workspace along the \vec{u}_1 axis. The arc having dark blue to green colors shows that HIPHAD has a greater stiffness that is on the right edge of the plane which are the smaller values of \vec{u}_1 axis. Compared to Plane 2, compliant displacements of HIPHAD becomes larger on this plane.

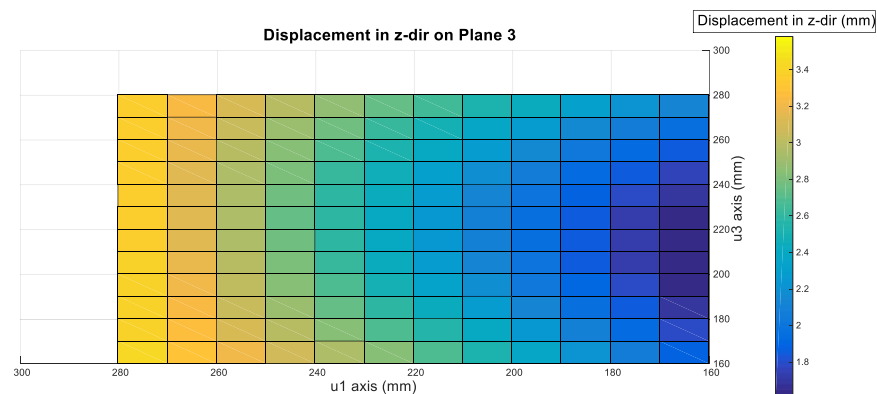


Figure 5.14 Compliant displacement values of HIPHAD in \vec{u}_3 -direction on Plane 3.

To provide better visualization of HIPHAD compliance map, in between the nodes that measurements are received, interpolation is carried out for the whole workspace. It can be observed from Figure 5.15 that HIPHAD shows an increasing compliance (or decreasing stiffness) values when the mobile platform is moved from the fully folded position at 160, 160 and 160 mm to fully extended position at 280, 280 and 280 mm along \vec{u}_1 , \vec{u}_2 and \vec{u}_3 directions respectively.

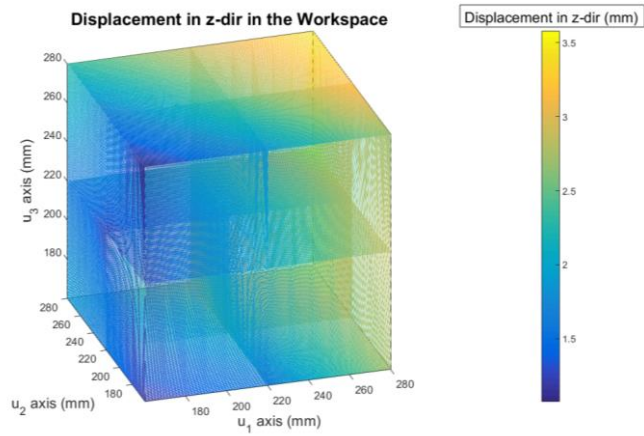


Figure 5.15 Compliance displacement of the HIPHAD under 700 g forcing along $(-\vec{u}_3)$ -direction throughout its workspace.

In the measurement taken for all three axes, HIPHAD shows a decreasing stiffness when the legs are extended. The decrease in stiffness for all three axes shows resembling compliance trends with different magnitudes. As it is observed from the compliant displacement figures, the stiffness of HIPHAD in \vec{u}_1 and \vec{u}_3 directions shares the same trend that shows dependency on the position of the mobile platform in all directions equally. On the other hand stiffness in \vec{u}_2 direction shows a dependency more on \vec{u}_1 and \vec{u}_3 directions. In following subsection results for analytical methods are provided.

5.2. Semi-Analytical Results

This section provides compliant displacement results obtained by semi-analytical methods on Planes 1, 2 and 3, which are the same planes used in the experimental tests. Same number of nodes are used in the semi-analytical studies as well. In VJM method calculations, joints' stiffness values that were determined by the formulation provided in Section 3.7 are used. Nodes from 0 to 27 represent the positions of the mobile platform in between 160 mm and 280 mm. Among these, measurements on nodes 1, 14 and 27 are

the ones to be compared with the experimental results obtained on the nodes used for experimental tests.

5.2.1. Semi-Analytical Results of VJM

Maximum and minimum compliant displacements on Plane 1 along \bar{u}_1 -axis under + 6.867 N force are calculated on nodes N(212,160,160) and N(280,160,280), which came out to be 1.351 and 0.372 mm, respectively. The surface plot in Figure 5.16 shows higher values near the right top corner, which is around 1.2 mm. However, it was expected that the larger compliant displacements would happen at the left top corner where the mobile platform is at the extended boundary of the workspace. On the contrary, the largest stiffness value was calculated at the top left corner of this plot.

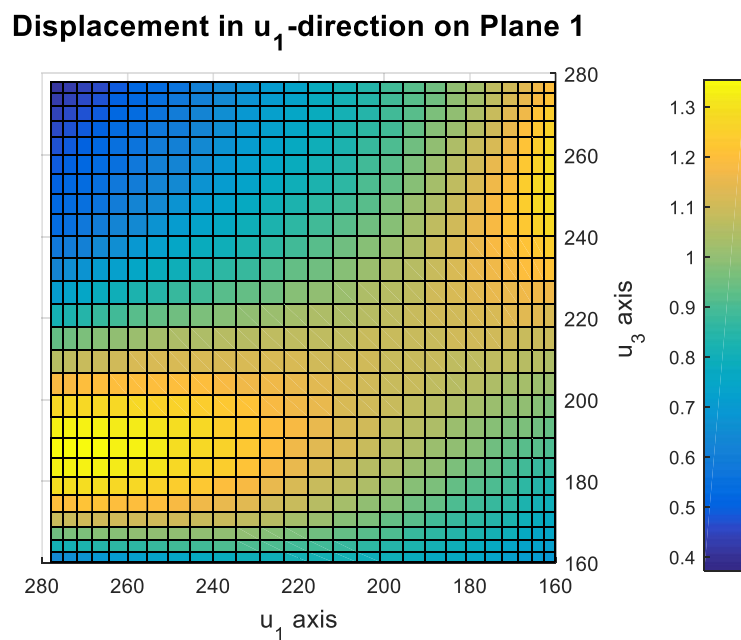


Figure 5.16 Calculated compliant displacement values of HIPHAD by VJM in \bar{u}_1 -direction on Plane 1.

The surface plot constructed with the analytical results obtained for compliant displacements on Plane 2 along \bar{u}_1 -direction is shown in Figure 5.17. This plot shows a region of larger compliant displacement values of HIPHAD at the top right corner. The maximum value of compliance displacement is 2.020 mm and minimum are 0.814 mm. These values are acquired on nodes N(160,220,280) and N(257,220,160). It was again expected that the larger compliant displacements would happen at the left top corner where the mobile platform is at the extended boundary of the workspace.

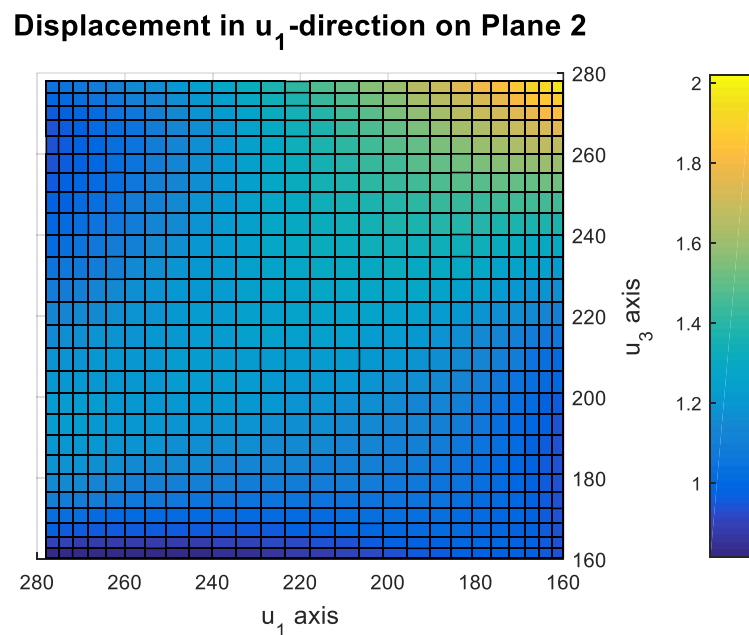


Figure 5.17 Calculated compliant displacement values of HIPHAD by VJM in \bar{u}_1 -direction on Plane 2.

Compliant displacements calculated on Plane 3 are provided in Figure 5.18. In this figure, compliant displacements range between 2.58 mm and 0.77 mm. These maximum and minimum values are calculated on the nodes N(280,280,280) and N(205,280,160). Dark blue elements are the displacement values around 0.8 mm, the transition region between blue and green regions are giving displacements around 1.4 mm and yellow areas are representing displacement values around 2.4 mm. On this plane, as expected, the stiffness of HIPHAD shows an increasing compliance towards the edge of the workspace along the \bar{u}_3 and \bar{u}_1 -axis. The arc having dark blue to green colors shows that HIPHAD has a greater stiffness in the middle for all levels along \bar{u}_3 -axis.

Displacement in u_1 -direction on Plane 3

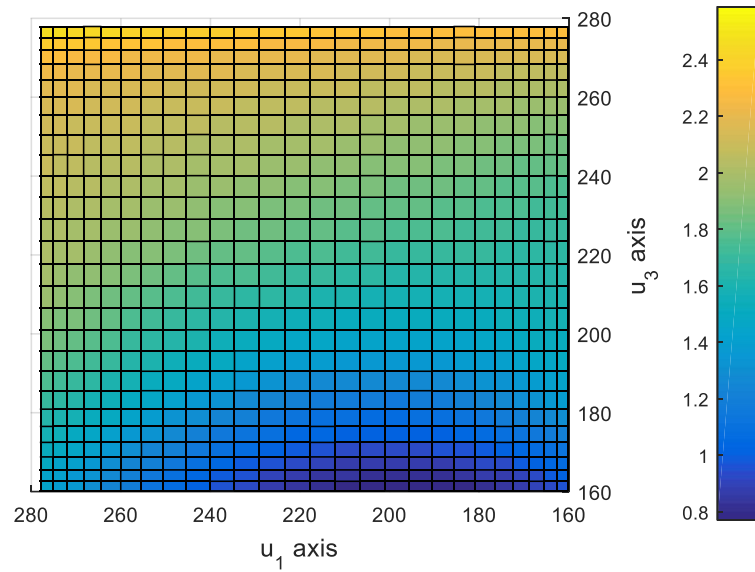


Figure 5.18 Calculated compliant displacement values of HIPHAD by VJM in \vec{u}_1 -axis on Plane 3.

Figure 5.19 shows the compliant displacement values of HIPHAD in \vec{u}_2 -direction on Plane 1. The data here has a range between 1.892 and 0.593 mm on the nodes N(280,160,187) and N(191,160,280). Dark blue regions show values around 0.8 mm while yellow areas are changing between 1.8 mm. On the top left corner compliant displacement of the HIPHAD shows a local peak and gives a 1.402 mm displacement.

Displacement in u_2 -direction on Plane 1

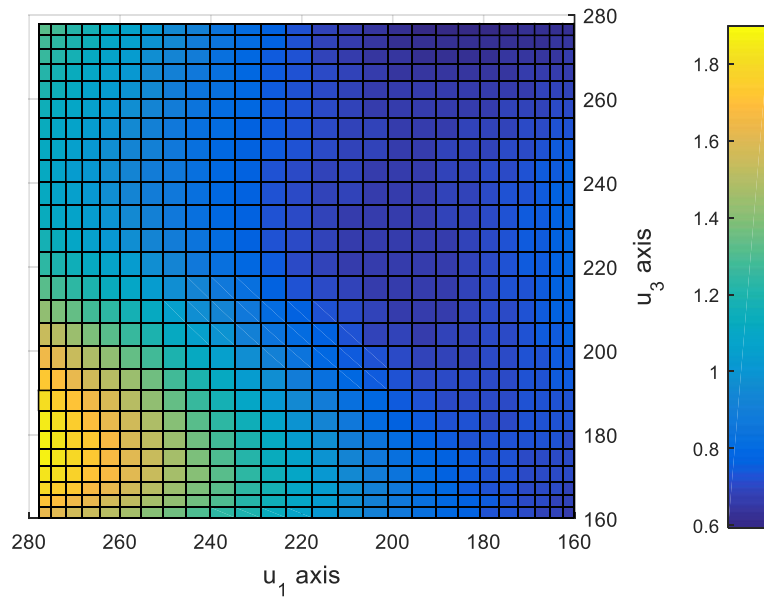


Figure 5.19 Calculated compliant displacement values of HIPHAD by VJM in \bar{u}_2 -direction on Plane 1.

In the surface plot provided in Figure 5.20, which is given for Plane 2, low stiffness areas given with yellow are splitting along the left edge and the higher stiffness regions on right top corner get smaller. Maximum and minimum values for HIPHAD on this plane are 2.070 mm and 0.755 mm on the middle of the left edge. According to the VJM model HIPHAD gets stiffer to towards the positive \bar{u}_1 direction. The nodes for the maximum and minimum values are N(280,220,280) and N(160,220,200).

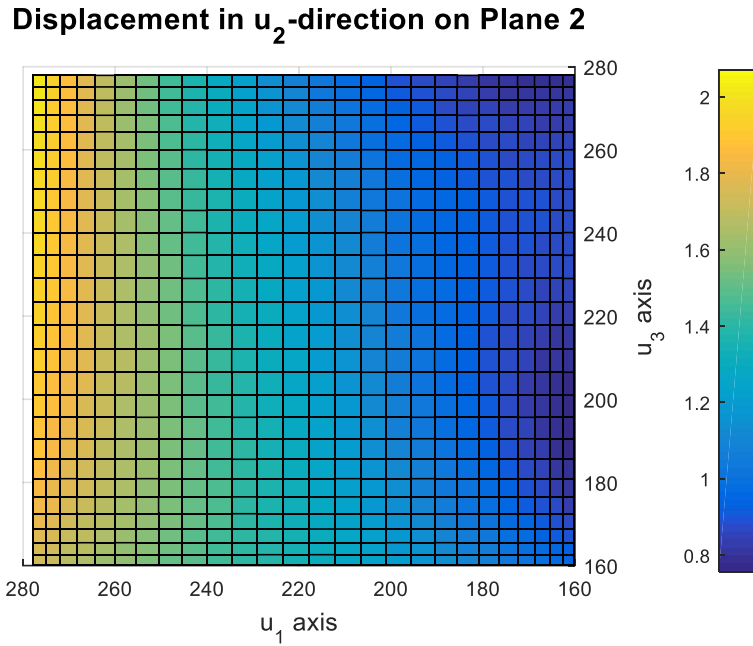


Figure 5.20 Calculated compliant displacement values of HIPHAD by VJM in \vec{u}_2 -direction on Plane 2.

The plot in Figure 5.21 is built with the results calculated on Plane 3 for compliant displacements in the \vec{u}_2 -direction. This plot shows a distributed region of lower compliance of HIPHAD to the top edge. The maximum value of compliance displacement is 2.729 mm and minimum are 0.3689 mm. These values are acquired on nodes N(280, 280,280) and N(160, 280, 280). Other than the dark blue region settled to the right top corner there is one more dark blue area on the right bottom corner which are giving displacement values around 0.5 mm. Moreover, there is a trend for high compliance values to shift to the top edge which is clearly seen when 2nd and 3rd Planes are compared to each other.

Displacement in u_2 -direction on Plane 3

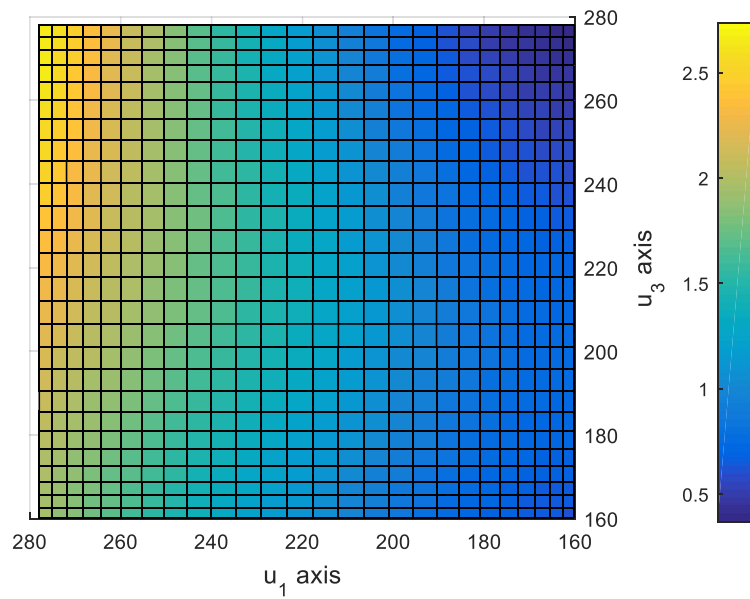


Figure 5.21 Calculated compliant displacement values of HIPHAD by VJM in \bar{u}_2 -direction on Plane 3.

Test results for compliant displacement in \bar{u}_3 -direction on plane 1 yields the results provided in Figure 5.22. Displacement values on this plane are measured between -0.415 and -2.239 mm. The maximum displacement on this plane is found on node defined at N(280, 160, 160), which is -2.239 mm and minimum displacement is measured at node N(160, 160, 280) that is -0.415 mm in \bar{u}_3 -direction. The surface plot shows an increase in the displacement values on the nodes defined at the higher \bar{u}_1 values. The compliance along \bar{u}_3 -axis propagates along \bar{u}_1 axis. The dark blue region shows the displacement values around -0.5 mm, light blue region denotes displacements of -0.8 to -1.2 mm and yellow region provides the displacement values between -2.2 mm.

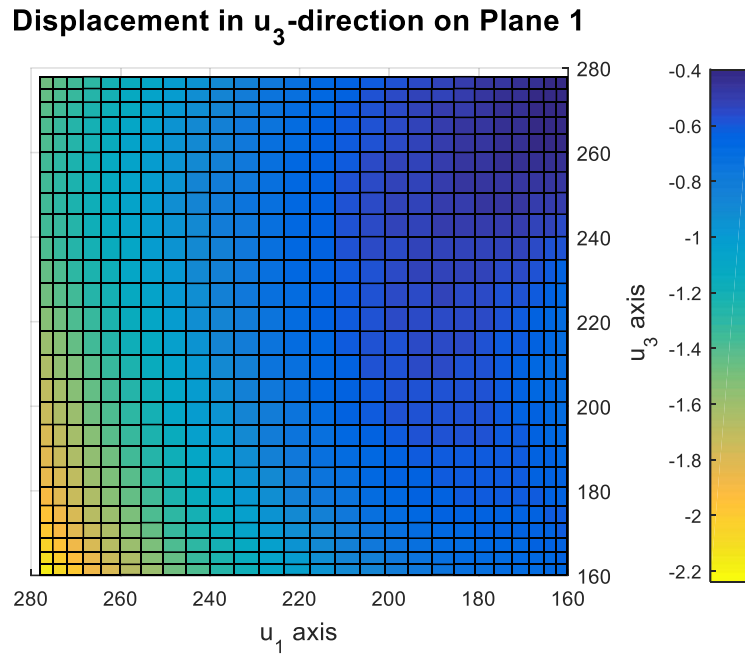


Figure 5.22 Calculated compliant displacement values of HIPHAD by VJM in \vec{u}_3 -direction on Plane 1.

In the surface plot provided in Figure 5.23, which is given for Plane 2, low stiffness areas, which are given with yellow, are splitting along the left edge and the higher stiffness regions on right top corner get smaller. Maximum and minimum values for HIPHAD on this plane are -2.091 mm and -0.589 mm. According to the VJM model HIPHAD gets stiffer towards the negative \vec{u}_1 direction. The nodes for the maximum and minimum values are N(280,220,250) and N(160,220,280).

Displacement in u_3 -direction on Plane 2

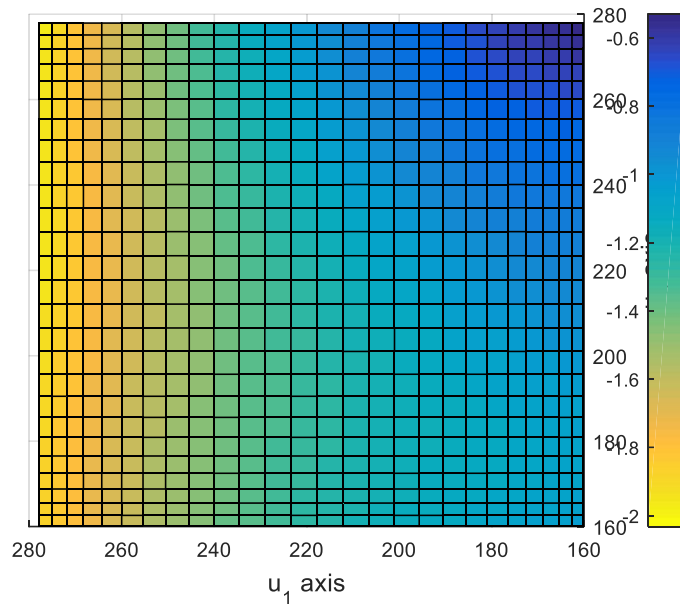


Figure 5.23 Calculated compliant displacement values of HIPHAD by VJM in \vec{u}_3 -direction on Plane 2.

Displacement values calculated on Plane 3 are provided in Figure 5.24. Maximum and minimum displacement values on this plane are given on the nodes defined at N(280,280,160) and N(160, 280,210) which are -2.835 and -0.347 mm. Dark blue elements are the displacement values around -0.6 mm, area between yellow and dark blue regions shows the displacement values between -2 and -1 mm and yellow areas are representing displacement values above -2.2 mm. Likewise, the 2nd plane, displacement values measured for 3rd plane show an increasing trend for higher \vec{u}_1 values. The compliance calculation reveals that HIPHAD has a greater stiffness that is on the right edge of the plane which are the smaller values of \vec{u}_1 axis. Compared to Plane 2, compliant displacements of HIPHAD becomes larger on this plane.

Displacement in u_3 -direction on Plane 3

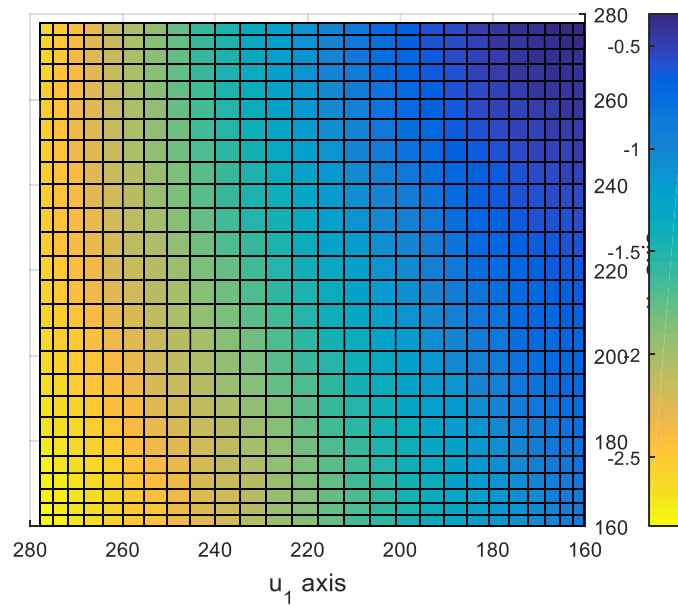


Figure 5.24 Calculated compliant displacement values of HIPHAD by VJM in \bar{u}_3 -direction on Plane 3.

In the following sub-section, results of SMA method will be written and discussed.

5.2.2. Semi-Analytical Results of SMA

Displacement values calculated via SMA based stiffness matrices yield values of 3.5×10^{-6} mm at maximum in all three measurements of displacements on Planes 1, 2 and 3. The surface plots for these calculations are provided in Figures 5.25, 5.26 and 5.27. In Figure 5.25 compliant displacements of HIPHAD shows a symmetry along the line intersecting \bar{u}_3 axis at node N(280,160,280). The maximum value for compliant displacement is 2.7×10^{-6} mm and minimum displacement is -4×10^{-6} mm at node N(240,160,160). The stiffness values on the left edge of this plane show higher values.

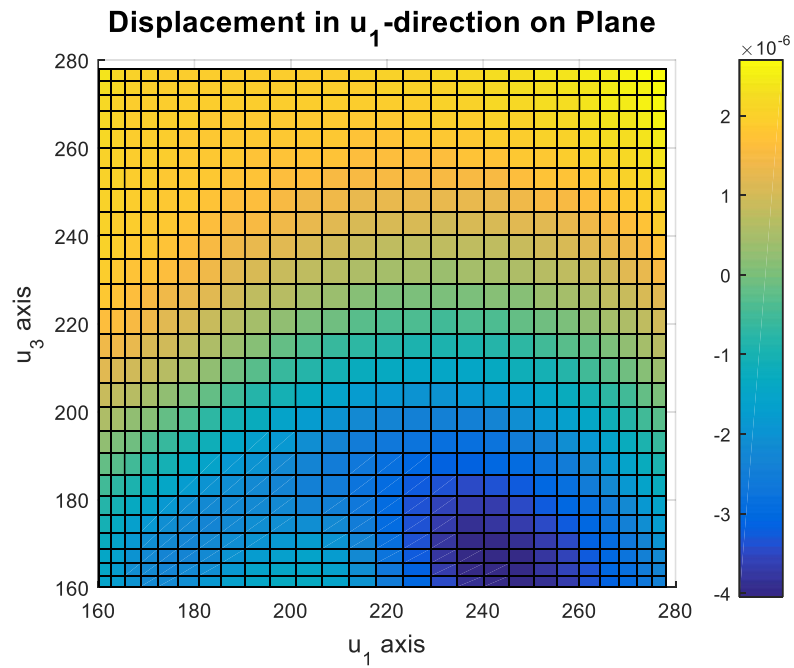


Figure 5.25 Calculated compliant displacement values of HIPHAD by SMA in \bar{u}_1 -direction on Plane 1.

For the 2nd Plane compliant displacement values, provided in Figure 5.26, shares the same trend for compliant displacement but for this plane displacement values gets higher values. In this plane, maximum value for compliant displacement is 1×10^{-6} mm and minimum displacement is -3×10^{-6} mm at nodes N(160,220,160) and N(260,220,160).

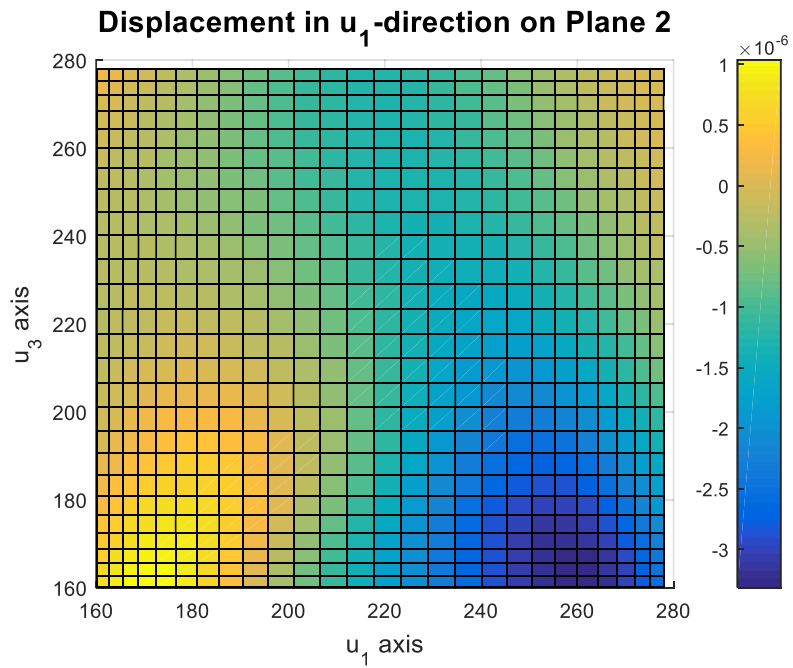


Figure 5.26 Calculated compliant displacement values of HIPHAD by SMA in \bar{u}_1 -direction on Plane 2.

In Figure 5.27, high compliance region closes the neck in the middle of the Plane 2 and creates a compliant displacement plot given in Plane 3. Other than the increasing values for the displacements, the stiffness does not change a lot and shows slightly more displacements than the one calculated on Plane 2.

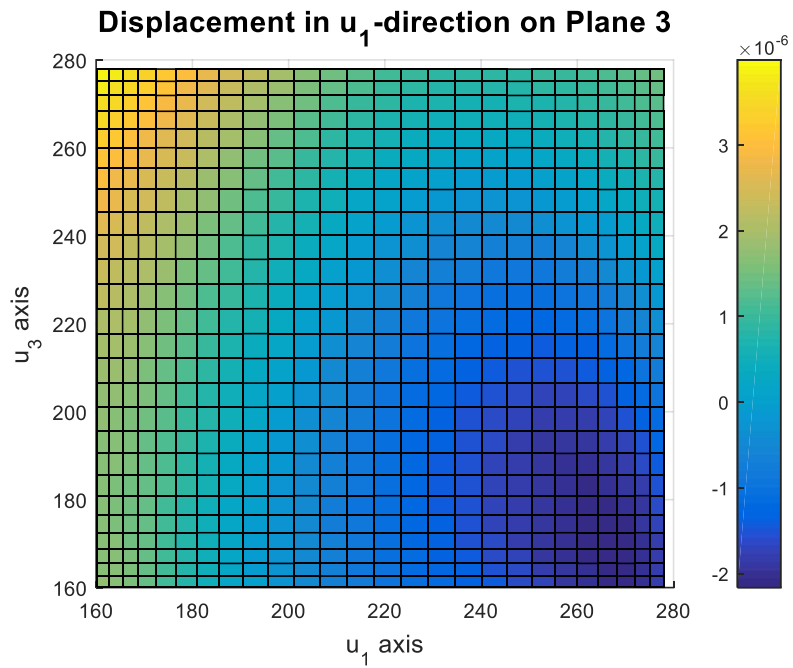


Figure 5.27 Calculated compliant displacement values of HIPHAD by SMA in \vec{u}_1 -direction on Plane 3.

Displacement values calculated for \vec{u}_2 -direction are bounded between 2.5×10^{-7} and -1.5×10^{-7} mm. Compliancy trends are not matching the experimental results. According to the previously presented results of VJM and experimental, dark blue areas should lean on the left bottom corner that is not the case for \vec{u}_2 – direction compliance for Plane 1.

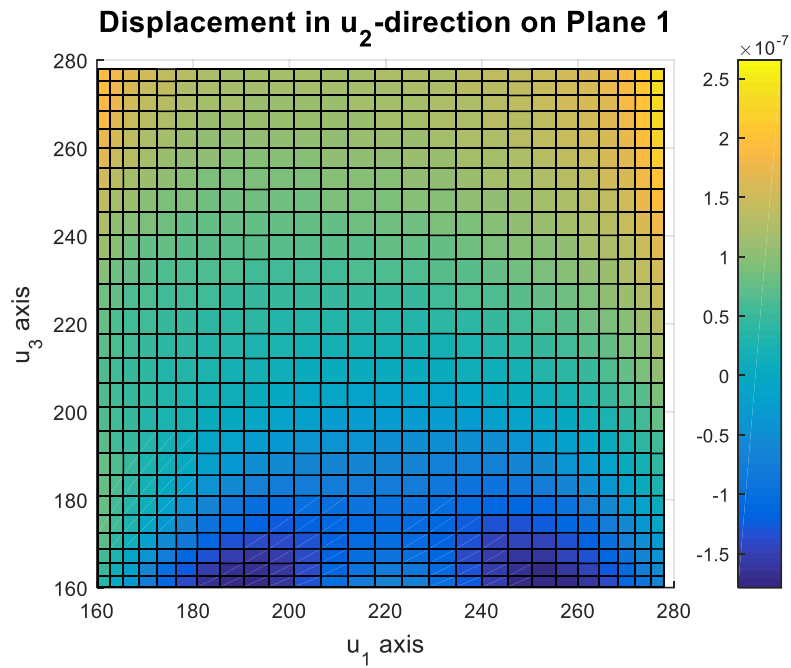


Figure 5.28 Calculated compliant displacement values of HIPHAD by SMA in \vec{u}_2 -direction on Plane 1.

The results given in Figure 5.28 and Figure 5.29, shows a resembling trend with the experimental results, however, magnitude of the compliant displacement is far less than the one measured in experimentation. As measured in experiments, stiffness model developed with SMA shows higher stiffness values in the left bottom corner, where the HIPHAD is at the folded position. The other high stiffness region calculated by SMA model is the difference of the trend given by SMA and real device.

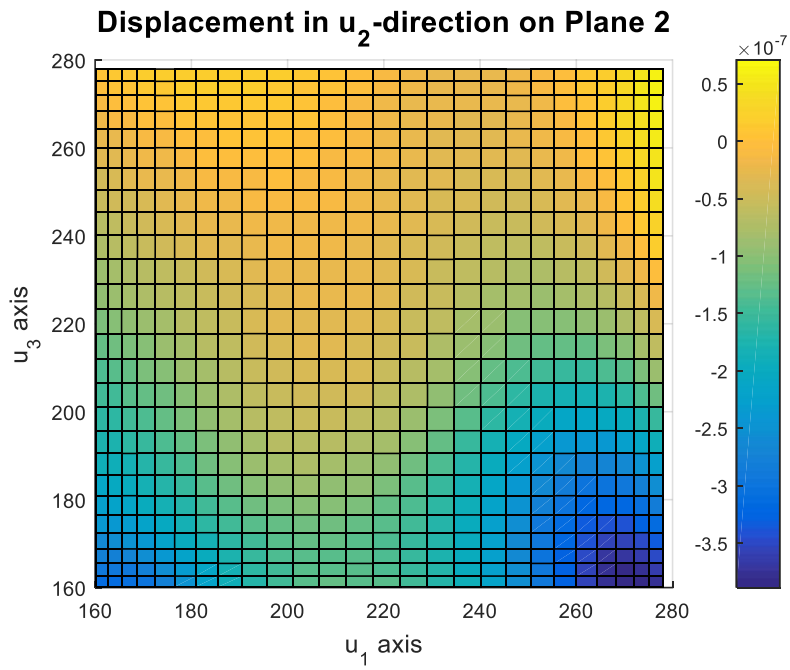


Figure 5.29 Calculated compliant displacement values of HIPHAD by SMA in \bar{u}_2 -direction on Plane 2.

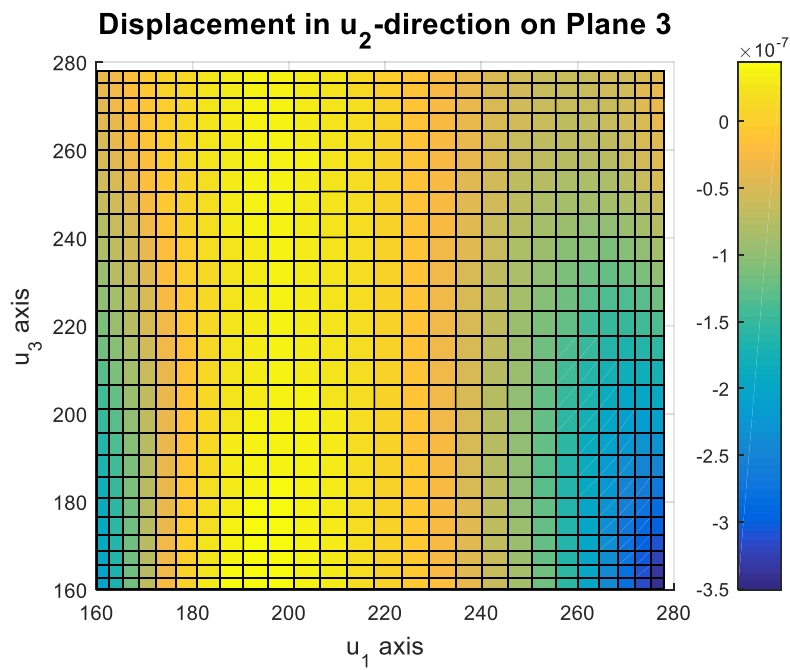


Figure 5.30 Calculated compliant displacement values of HIPHAD by SMA in \bar{u}_2 -direction on Plane 3.

Displacement values calculated in \bar{u}_3 -axis on Plane 1, 2 and 3 are provided in Figures 5.31-33. Maximum and minimum displacement values on this plane are -3.5×10^{-7} mm and 1.5×10^{-7} mm. From Plane 1 to Plane 3 displacement values change between the levels of -5×10^{-7} and 5×10^{-7} . On second plane, compliant regions of the workspace leans on the right edge. On 3rd Plane, stiff regions of HIPHAD are concentrated on the left edge of the plane and displacement values are ranging between 1.5×10^{-7} mm.

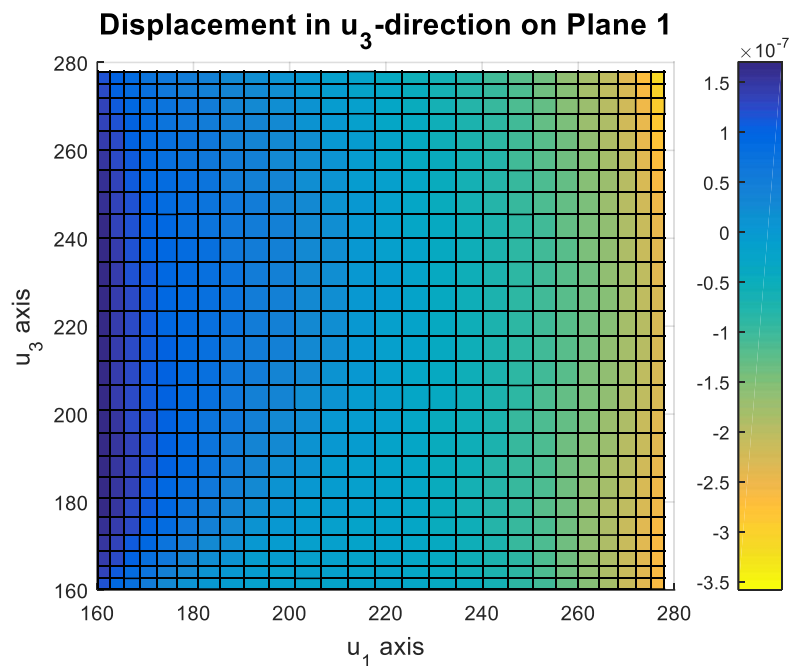


Figure 5.31 Calculated compliant displacement values of HIPHAD by SMA in \bar{u}_3 - direction on Plane 1.

For SMA it is expected to represent changes in stiffness from one plane to the other. This is due to the highly non-linear model of stiffness model of HIPHAD. However, there is no joint stiffness defined in SMA, which is more dominant in compliant displacement of HIPHAD. Therefore, without joint stiffness values, SMA provides inaccurate results.

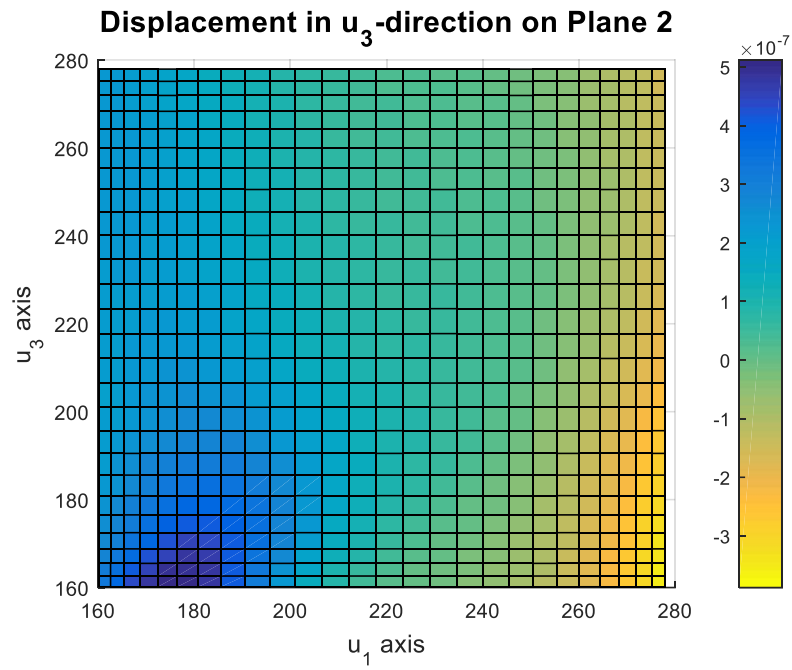


Figure 5.32 Calculated compliant displacement values of HIPHAD by SMA in \vec{u}_3 -direction on Plane 2.

In 3rd plane, dark blue region denotes the displacement values around 2×10^{-7} mm and yellow region defines the displacement values close to -5×10^{-7} . With the extension of legs along the direction of \vec{u}_1 .

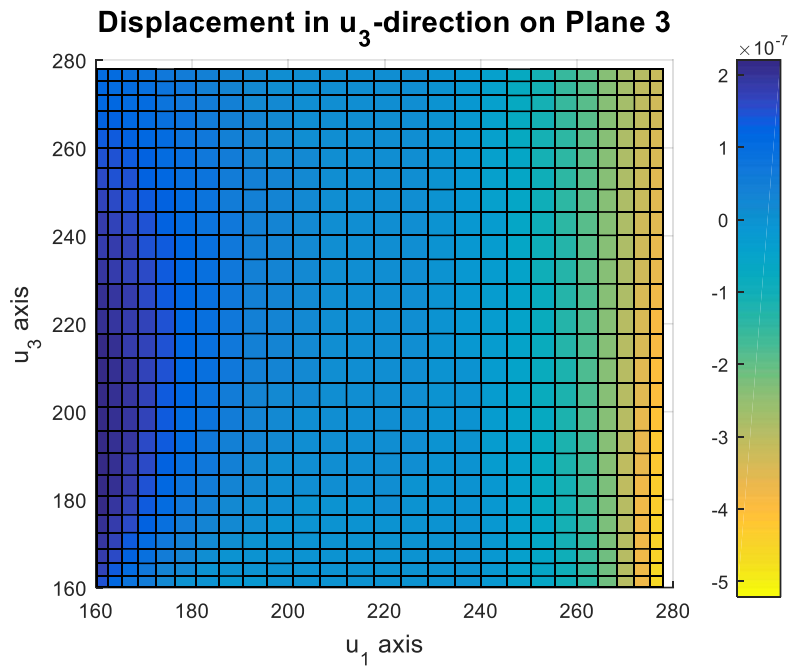


Figure 5.33 Calculated compliant displacement values of HIPHAD by SMA in \vec{u}_3 -direction on Plane 3.

5.3. Comparison

Results obtained in VJM for the compliance in \vec{u}_1 -axis on Plane 1, has close local maximum and local minimum points with the experimental results that are placed on the folded position along \vec{u}_1 -axis. These points are on N(160,160,280) and N(160,160,160). From the right bottom corner, the propagation of the compliance also shares the similar trends, however, the resemblance fades away towards the node N(280,160,280). The range of compliant displacement calculation errors are provided in Figure 5.34. It is clearly seen in the subplot for Plane 1 that when HIPHAD moves towards the N(280,160,280) error values are around -2mm. Other than this particular spot, error values range between -0.5 mm and -1mm.

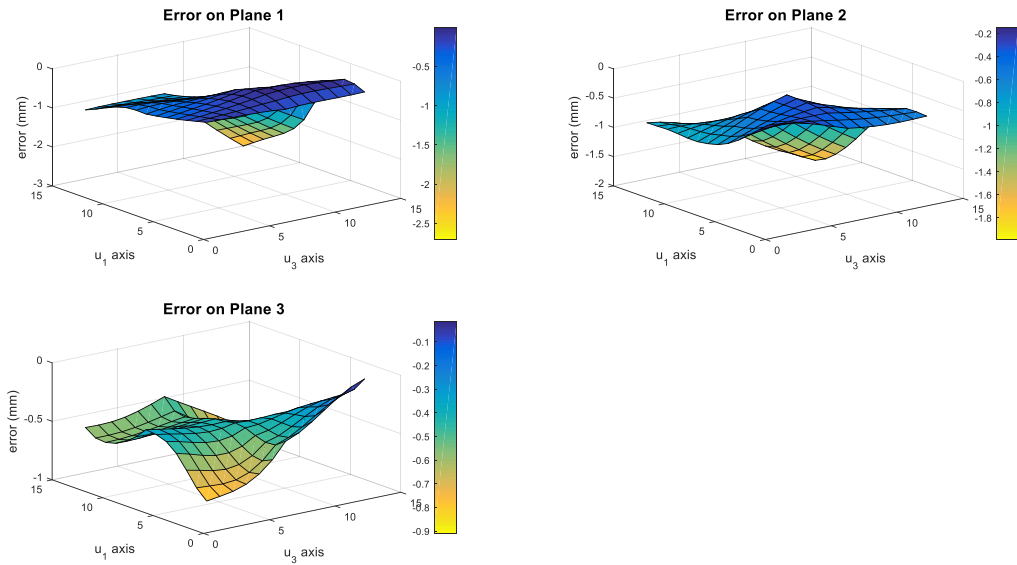


Figure 5.34 Surface plots representing the errors between VJM displacements and measured displacements on \vec{u}_1 -direction

For the second plane, the region of higher stiffness values is generated on the same edge, while the maximum displacements are obtained on different corners. Other than the nodes in which maximum compliant displacements are calculated, results obtained by VJM range between 1.2 and 1.6 mm. The experimental results for this plane also show a small change in displacements that is in the range of 1.5 to 2 mm. In Figure 5.34, error in between the calculated compliant displacements with the measured ones are bounded in the region of -0.2 to -1.8mm.

Finally, for the displacement values in the same direction on Plane 3, calculated and measured local maximum and minimum values for the compliant displacements are spotted at the similar nodes. Propagation of the stiffness characteristics of HIPHAD obtained through experimentation and through VJM calculation shares the same trend on this plane. Considering the values of the compliant displacements, the results obtained with VJM calculation range between 0.8 to 2.6 mm while measured compliant displacements at the same nodes came out to be between 1.7 and 3.2 mm. The error values between the calculated and the measured compliant displacements are represented in Figure 5.34 in Error on Plane 3 subplot. This subplot shows that error is bounded between -0.1 and -0.9 mm. Root mean squares (RMS) of the errors for VJM method are given in Table 5.2, which is calculated by using errors at nodes that are used in experimental tests.

Table 5.2 RMSE of compliant displacements calculated by VJM calculations results and experimental measurements in \vec{u}_1 -axis

RMS Errors of Displacements in \vec{u}_1 -axis		
Plane 1	Plane 2	Plane 3
0.4878 mm	0.7537 mm	1.3659 mm

The VJM method fails to provide the trend of the experimental results in all three sets of measurements for \vec{u}_2 -direction that is executed on Planes 1, 2 and 3. On plane 1, displacement calculation using VJM for \vec{u}_2 -direction yields a range that is 0.6 to 1.9 mm. The higher displacements occur on the left edge that intersects the measured values on the outermost corner, which is the vicinity of the node N(280,160,280). In experimental case, HIPHAD deforms in the range of 0.8 to 2.2 mm that is on the top edge of the same plane. Error surface plot for displacement values in the \vec{u}_2 -direction on Plane 1 is given in Figure 5.35 under the title Error on Plane 1. Clearly given in this surface plot that, VJM provides a low overall error other than the error that is colored by blue in Figure 5.35, which corresponds to the right top corner of the same plane. The error for this plane is bounded between -0.1 and 0.6 mm.

The same outcome is read from the two figures that are plotted for the Plane 2 and 3. In VJM method likewise the first section, the higher displacement values are calculated on the left edge and the displacement range of HIPHAD model is between 0.8 and 2.2 mm. Other than the trend stiffness propagation, the range of displacements measured in experimentation settles in the range of 0.8 to 2.2 mm from bottom to top of the same plane. Giving the error plot for this surface that is provided in Figure 5.35 under the title of Error on Plane 2, the error is bounded between -0.4 and 0.5 mm and it is symmetrically distributed around the line that intersects 220 mm on \vec{u}_3 axis.

In the third plane, displacement measurements are between 0.5 and 2.5 mm for analytical calculations held in VJM while the experimental results are between 0.6 and 1.7mm. Looking over the error plot given in Figure 5.32 under the title Error on Plane 3, the error is bound to -1.5 to 1 mm.

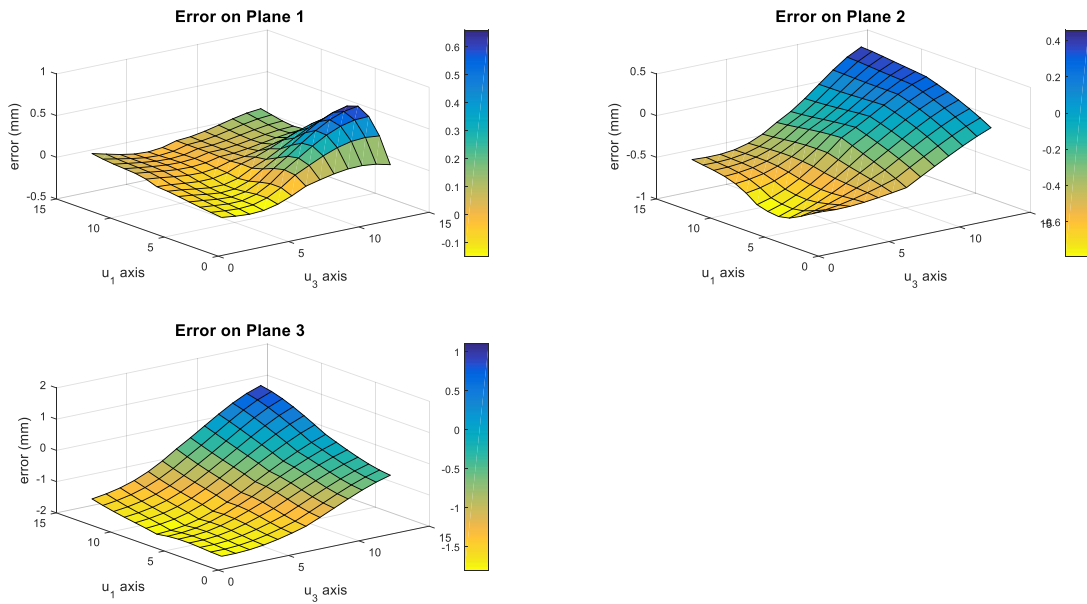


Figure 5.35 Surface plots representing the errors between VJM displacements and measured displacements on y-direction

The RMSE results are provided in Table 5.3 to give a clue on the overall performance.

Table 5.3 RMSE of displacements calculated by VJM and measured in experimentation in \bar{u}_2 -direction

RMS Errors of Displacements in \bar{u}_2-direction		
Plane 1	Plane 2	Plane 3
0.4467 mm	0.5674 mm	1.999 mm

Among all three displacement calculations with VJM, the one for \bar{u}_3 -direction gives the best fit for the creation and propagation of the stiffness characteristic on two out of three planes. On Plane 1, VJM gives a compliance of HIPHAD that results in a displacement range of -2.2 to -0.4 mm. The trend for stiffness characteristic change with respect to the coordinate axis fits at some point where the local maximum displacements are occurring with the experimental results, the displacement calculations have an offset

between the real displacement measurements on this plane that the experimental results are floating in the range of -0.1 to 0.25.

The displacement measurements on Plane 2 and 3 fits with the VJM results in the sense of developing the manner of the stiffness characteristics. Moreover, the calculated displacements are close to the one that is measured on HIPHAD. The calculated displacements for HIPHAD on Planes 2 and 3 are in the ranges of -2 to -0.6 and -2.5 to -0.5 mm. The error plot for the planes is given in Figure 5.36 respectively.

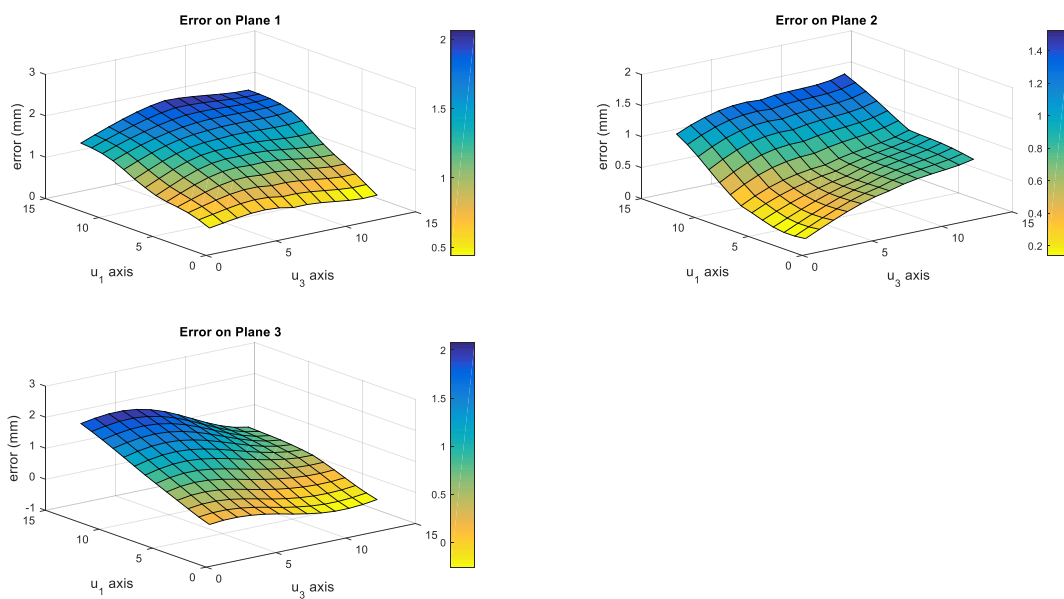


Figure 5.36 Surface plots representing the errors between VJM displacements and measured displacements on \vec{u}_3 -direction

The RMSE results are provided in Table 5.3 to give the overall performance.

Table 5.4 RMSE of displacements calculated by VJM and measured in experimentation in \bar{u}_3 -direction

RMS Errors of Displacements in \bar{u}_3-direction		
Plane 1	Plane 2	Plane 3
1.7315 mm	1.4336 mm	1.3084 mm

Compared to the VJM and experimental results, SMA results are not comparable in terms of accuracy. The ranges for displacements are around 10^{-7} mm for calculations in \bar{u}_1 -, \bar{u}_2 - and \bar{u}_3 -directions. Considering the trend of stiffness propagation throughout the workspace, SMA is able to give the resembling trend with the experimental data in \bar{u}_1 -, \bar{u}_2 - and \bar{u}_3 -directions.

Computational cost of the two semi-analytical methods is also measured. To measure the time for executing one loop, codes are run for computing compliant displacements on one node. Same computational environment, which is Matlab, is used for this test. As a result, computational times required for the same calculation with SMA and VJM are measured to be 0.074 s and 0.035s, respectively.

In this section, experimental and semi-analytical results for obtaining compliant displacements are visualized with the figures. These displacement values show the change of stiffness value of HIPHAD in its workspace. Once the results for experimental and semi-analytical data are discussed, then results with VJM method and experimental results are compared to each other by means of calculating the difference of compliant displacement result at each node throughout the workspace. Then the RMSE values are provided to show the overall error of the semi-analytical method calculation.

In the following section, these results are discussed and possible reasons for errors in calculated compliance of HIPHAD are given.

CHAPTER 6

CONCLUSIONS

In this thesis, stiffness matrix calculation of HIPHAD haptic device is executed by two semi-analytical methods. The methods used in this master thesis are selected among the possible methods in the literature of stiffness matrix calculation methods. In this thesis, first, the possible sources of errors in accuracy and repeatability of robots are presented and the compensation methods used in the literature are provided. Then, the methods for calculating stiffness matrix is provided and the experimental methods used by other researchers are presented.

This thesis explains three main studies on obtaining the stiffness characteristics of HIPHAD haptic device, which are stiffness calculation using VJM, SMA and measuring compliant displacements of the HIPHAD due to the stiffness characteristics by using stereo vision cameras. The cameras are initially used in calibration of encoders, which is used to measure the angular positions of actuated joints and thus, indirectly measure the position of the wrist point. After the calibration process, the experimentation is carried out to reveal the stiffness characteristic of HIPHAD. Two cameras are used to measure the absolute position of the mobile platform, specifically the wrist point position. By this way, compliant displacement of the mobile platform is measured along three orthogonal axes.

VJM is one of the methods that is used in this thesis. To carry out VJM calculations, each leg of HIPHAD is modeled with active joints, passive joints, and virtual joints. Then, Jacobian matrices for passive joints and virtual joints are calculated and Cartesian stiffness matrix of each are found. These Cartesian stiffness matrices are superposed to develop HIPHAD's equivalent stiffness matrix. In the other semi-analytical method called SMA, the stiffness matrix of HIPHAD is constructed by assembling the stiffness matrices of links by defining geometric constraints. These geometric constraints include constraints defined by a joint and rigid body constraints.

Experimental results indicate that HIPHAD becomes more compliant on the most extended positions. In addition, the measured displacement of the mobile platform under forces is not only caused by the compliance of manipulator but due to the wear and backlash in the joints. Due to this reason, any method to be used to model stiffness of HIPHAD should include the effects of the joint clearances within the model. However, joint clearance models are not included in the VJM or SMA method of stiffness modelling.

The analytical results with VJM modelling came out to be closer to the results obtained by experimentation. RMS of errors calculated by the difference between the VJM and experimentation results changes from 1.38 mm to 0.20 mm. In addition, VJM shows the best resemblance of the actual stiffness map of HIPHAD considering the stiffness change with respect to the position of the wrist point along \vec{u}_1 -, \vec{u}_2 - and \vec{u}_3 -axes.

The reason of the error between VJM results and experimental results are the calculation of the joint stiffness values. They are calculated on the node defined at 220mm, 220mm, 220mm along \vec{u}_1 -, \vec{u}_2 - and \vec{u}_3 -axes however, these stiffness values are used in calculations for the whole workspace with the assumption that they are the same at any location. Another reason of inaccuracy of the model is the simplified stiffness model of HIPHAD to reduce computational expenses. As a result of using a simplified model, VJM takes 0.035s to run a single loop.

Analytical results for SMA shows similar results considering the change of stiffness throughout the workspace. However, SMA model results in very small compliant displacements since it only includes links stiffness matrices. However, the most flexible parts of the HIPHAD mechanism is observed to be the joint structures compared to the link structures. SMA gives the most detailed illustration of stiffness variation of HIPHAD throughout its workspace since it includes all of the compliance elements other than the joint stiffness values. The calculation of stiffness matrix using this method took 0.074s to run a single loop.

It should be noted that VJM provides an easier implementation of joint stiffness values without any need of changing matrices of high dimensions. This allows the designer to change the stiffness model easily. Evaluating the flexibility, simplicity,

computational cost and accuracy of two methods that are applied for the calculation of stiffness matrix of HIPHAD, VJM provides better results under the same conditions.

As a future work, joint stiffness values should be recalculated without using the assumptions made in this thesis. This calculation can be accommodated by measuring rotational compliant displacements in addition to the translational compliant displacements. It can be observed from HIPHAD mechanism's current condition that most of the initial displacement when a force is applied is due to the joint clearances which have increased due to joint wear in time. Therefore, joint clearance models can be included in the stiffness model to increase accuracy of the model output. However, it is foreseen that addition of joint stiffness and possibly joint clearance to the SMA method would make the calculations even more complex and decrease the computation time drastically even if a solution can be obtained. Nevertheless, addition of accurately calculated joint stiffness models and joint clearance should be studied as a future work on VJM method.

Additionally, based on the obtained stiffness characteristics of HIPHAD, future work on the design changes for the HIPHAD mechanism can include an improved joint structure design that has smaller joint clearances and use of materials with high strength-to-weight ratio, such as carbon-fiber pipes, for constructing the links.

REFERENCES

- Aginagaa J., Zabalzaa I., Altuzarrab O., Nájeraa J. (2012, August). Improving static stiffness of the parallel manipulator using inverse singularities, *Robotics and Computer-Integrated Manufacturing*, 28(4), 458-471, ISSN 0736-5845.
- Ahmad, A., Andersson, K., Sellgren, U., & Khan, S. (2014). A stiffness modeling methodology for simulation-driven design of haptic devices. *Engineering with Computers*, 30(1), 125-141.
- Alici, G., & Shirinzadeh, B. (2005). Enhanced stiffness modeling, identification and characterization for robot manipulators. *Robotics, IEEE Transactions on*, 21(4), 554-564.
- Aoyagi, S., Suzuki, M., Takahashi, T., Fujioka, J., & Kamiya, Y. (2012). Calibration of kinematic parameters of robot arm using laser tracking system: compensation for non-geometric errors by neural networks and selection of optimal measuring points by genetic algorithm. *International Journal of Automation Technology*, 6(1), 29-37.
- Barbieri, L., Bruno, F., Cosco, F., & Muzzupappa, M. (2014). Effects of device obtrusion and tool-hand misalignment on user performance and stiffness perception in visuo-haptic mixed reality. *International Journal of Human-Computer Studies*, 72(12), 846-859.
- Basdogan, C.; Ho, C.-H.; Srinivasan, M.A., (2001). "Virtual environments for medical training: graphical and haptic simulation of laparoscopic common bile duct exploration," in *Mechatronics, IEEE/ASME Transactions on*, vol.6, no.3, pp.269-285, doi: 10.1109/3516.951365
- Baser, O., Konukseven, E. I., & Gurocak, H. (2012, September). Stability and transparency improvement in haptic device employing both mr-brake and active actuator. In *RO-MAN, 2012 IEEE* (pp. 12-18). IEEE.
- T. Bilginca, E. Gezgin, and M. I. C. Dede, "Integration of the Hybrid-Structure Haptic Interface HIPHAD v1.0," in *Proceedings of the International Symposium of Mechanism and Machine Theory*, Izmir, Turkey, pp. 267-284, October 5-8, 2010.
- Carbone, G. (2003). Stiffness evaluation of multibody robotic systems (Doctoral dissertation, PhD Dissertation, LARM, University of Cassino, Cassino).
- Carbone, G. (2011). Stiffness analysis and experimental validation of robotic systems. *Frontiers of Mechanical Engineering*, 6(2), 182-196.
- Ceccarelli, M., & Carbone, G. (2002). A stiffness analysis for CaPaMan (Cassino parallel manipulator). *Mechanism and Machine Theory*, 37(5), 427-439.

- Ceccarelli, M., & Carbone, G. (2005). Numerical and experimental analysis of the stiffness performances of parallel manipulators. In 2nd international colloquium collaborative research centre (Vol. 562, pp. 21-35).
- Chen, J., & Chao, L. M. (1987). Positioning error analysis for robot manipulators with all rotary joints. *Robotics and Automation, IEEE Journal of*,3(6), 539-545.
- Clinton, C. M., Zhang, G., & Wavering, A. J. (1997). Stiffness Modeling of a Stewart Platform Based Milling Machine.
- Colgate, J. E., & Brown, J. M. (1994, May). Factors affecting the z-width of a haptic display. In *Robotics and Automation, 1994. Proceedings, 1994 IEEE International Conference on* (pp. 3205-3210). IEEE.
- Corradini, C., Fauroux, J. C., & Krut, S. (2003). Evaluation of a 4-degree of freedom parallel manipulator stiffness. In *Proceedings of the 11th World Congress in Mechanisms and Machine Science, Tianjin (China)*.
- Deblaise, D., Hernot, X., & Maurine, P. (2006, May). A systematic analytical method for PKM stiffness matrix calculation. In *Robotics and Automation, 2006. ICRA 2006. Proceedings 2006 IEEE International Conference on* (pp. 4213-4219). IEEE.
- Di Alessio, F. L., Nitti, M., Renna, F., Attolico, G., & Distanto, A. (2004). Characterizing the 3D Tracking Performance of a Haptic Device. In *Proc. of the 4th International Conference EuroHaptics* (pp. 5-7).
- Calculating Camera Sensor Resolution and Lens Focal Length, (27.06.2014), retrieved from: <http://digital.ni.com/public.nsf/allkb/1948AE3264ECF42E86257D00007305D5>
- Gong, C., Yuan, J., & Ni, J. (2000). Nongeometric error identification and compensation for robotic system by inverse calibration. *International Journal of Machine Tools and Manufacture*, 40(14), 2119-2137.
- Gosselin, C. (1990). Stiffness mapping for parallel manipulators. *Robotics and Automation, IEEE Transactions on*, 6(3), 377-382.
- Gosselin, C. (2002). *International Journal Of Robotics And Automation* 17(1):17-27
- Hirche, S., & Buss, M. (2012). Human-oriented control for haptic teleoperation. *Proceedings of the IEEE*, 100(3), 623-647.
- Hokayem, P. F., & Spong, M. W. (2006). Bilateral teleoperation: An historical survey. *Automatica*, 42(12), 2035-2057.

- Huang, T., Zhao, X., & Whitehouse, D. J. (2002). Stiffness estimation of a tripod-based parallel kinematic machine. *Robotics and Automation, IEEE Transactions on*, 18(1), 50-58.
- Kern, T. A. (2009). *Engineering haptic devices: a beginner's guide for engineers*. Springer Science & Business Media.
- Klimchik, A. (2011). Enhanced stiffness modeling of serial and parallel manipulators for robotic-based processing of high performance materials (Doctoral dissertation, Ecole Centrale de Nantes (ECN)(ECN)(ECN)(ECN); Ecole des Mines de Nantes).
- Klimchik, A., Bondarenko, D., Pashkevich, A., Briot, S., & Furet, B. (2014). Compliance error compensation in robotic-based milling. In *Informatics in Control, Automation and Robotics* (pp. 197-216). Springer International Publishing.
- Kosić, D., Đalić, V., & Marić, P. (2010). Robot Geometry Calibration in an Open Kinematic Chain Using Stereo Vision. In *Proc. International Scientific Conference UNITECH* (pp. 528-531).
- Koul, M. H., Manivannan, M., & Saha, S. K. (2013, July). Enhancing the Z-width of Haptics Interfaces through Dual-rate Sampling. In *Proceedings of Conference on Advances In Robotics* (pp. 1-6). ACM.
- Kumar, V. (1997, April). Affine connections for the Cartesian stiffness matrix. In *Robotics and Automation, 1997. Proceedings., 1997 IEEE International Conference on* (Vol. 2, pp. 1376-1381). IEEE.
- Lawrence, D.A., "Stability and transparency in bilateral teleoperation," in *Robotics and Automation, IEEE Transactions on*, vol.9, no.5, pp.624-637, Oct 1993 doi: 10.1109/70.258054
- Lee, D. Y., Nam, Y. J., Park, M. K., & Yamane, R. (2010). Transparency improvement of a 1 DOF hybrid haptic device with wide-ranged torque reflection. *International Journal of Applied Electromagnetics and Mechanics*, 33 (1, 2).
- Lei, W. T., & Sung, M. P. (2008). NURBS-based fast geometric error compensation for CNC machine tools. *International Journal of Machine Tools and Manufacture*, 48(3), 307-319.
- Lim, H. O., Setiawan, S., & Takanishi, A. (2001). Balance and impedance control for biped humanoid robot locomotion. In *Intelligent Robots and Systems, 2001. Proceedings. 2001 IEEE/RSJ International Conference on* (Vol. 1, pp. 494-499). IEEE.
- Logan, D. (2011). *A first course in the finite element method*. Cengage Learning.
- López, J., Breñosa, J., Galiana, I., Ferre, M., Giménez, A., & Barrio, J. (2012). Mechanical design optimization for multi-finger haptic devices applied to virtual

grasping manipulation. *Strojniški vestnik-Journal of Mechanical Engineering*, 58(7-8), 431-443.

Majou, F. (2004). Kinetostatic analysis of translational parallel kinematic machines (Doctoral dissertation, Ph. D. thesis, Université Laval, Quebec, Canada and Ecole Centrale Nantes, France).

Majou, F., Gosselin, C., Wenger, P., & Chablat, D. (2007). Parametric stiffness analysis of the Orthoglide. *Mechanism and Machine Theory*, 42(3), 296-311.

McGuire, W., Gallagher, R. H., & Ziemian, R. D. (2000). Matrix structural analysis.

Meggiolaro, M. A., Dubowsky, S., & Mavroidis, C. (2004). Error identification and compensation in large manipulators with application in cancer proton therapy. *Sba: Controle & Automação Sociedade Brasileira de Automatica*, 15(1), 71-77.

Meggiolaro, M. A., Dubowsky, S., & Mavroidis, C. (2005). Geometric and elastic error calibration of a high accuracy patient positioning system. *Mechanism and Machine Theory*, 40(4), 415-427.

Merlet, J. P. (2006). *Parallel robots* (Vol. 128). Springer Science & Business Media.

<http://www.ni.com/white-paper/3638/en/#toc3>, access date: 15.09.2015

Pashkevich, A., Wenger, P., & Chablat, D. (2007, April). Kinematic and stiffness analysis of the Orthoglide, a PKM with simple, regular workspace and homogeneous performances. In *Robotics and Automation, 2007 IEEE International Conference on* (pp. 549-554). IEEE.

Pashkevich, A., Chablat, D., & Wenger, P. (2008, May). Stiffness analysis of 3-dof overconstrained translational parallel manipulators. In *Robotics and Automation, 2008. ICRA 2008. IEEE International Conference on* (pp. 1562-1567). IEEE.

Pashkevich, A., Chablat, D., & Wenger, P. (2009). Stiffness analysis of overconstrained parallel manipulators. *Mechanism and Machine Theory*, 44(5), 966-982.

Pêgo, J. M. T., Gonçalves, R. S., Carvalho, J. C. M., Carbone, G., & Ceccarelli, M. (2013). Stiffness Analysis of CaPaMan-2bis Using Finite Element Analysis. In *22nd International Congress of Mechanical Engineering (COBEM 2013) November* (pp. 3-7).

Pinto, C., Corral, J., Altuzarra, O., & Hernández, A. (2010). A methodology for static stiffness mapping in lower mobility parallel manipulators with decoupled motions. *Robotica*, 28(05), 719-735.

Przemieniecki, J. S. (1985). *Theory of matrix structural analysis*. Courier Corporation.

- Schwenke, H., Knapp, W., Haitjema, H., Weckenmann, A., Schmitt, R., & Delbressine, F. (2008). Geometric error measurement and compensation of machines—an update. *CIRP Annals-Manufacturing Technology*, 57(2), 660-675.
- Shen, H., Fu, J., He, Y., & Yao, X. (2012). On-line asynchronous compensation methods for static/quasi-static error implemented on CNC machine tools. *International Journal of Machine Tools and Manufacture*, 60, 14-26.
- Stuart, J. L., & Weaver, J. R. (1991). Matrices that commute with a permutation matrix. *Linear Algebra and Its Applications*, 150, 255-265.
- Švaco, M., Šekoranja, B., Šuligoj, F., & Jerbić, B. (2014). Calibration of an industrial robot using a stereo vision system. *Procedia Engineering*, 69, 459-463.
- Varalakshmi, B. D., Thriveni, J., Venugopal, K. R., & Patnaik, L. M. (2012). Haptics: State of the Art Survey. *International Journal of Computer Science Issues*, 9(5).
- Wang, S. M., Yu, H. J., & Liao, H. W. (2004, January). A new high-efficiency error compensation system for CNC multi-axis machine tools. In *ASME 2004 International Mechanical Engineering Congress and Exposition* (pp. 461-470). American Society of Mechanical Engineers.
- Xi, F., Zhang, D., Mechefske, C. M., & Lang, S. Y. (2004). Global kinetostatic modelling of tripod-based parallel kinematic machine. *Mechanism and Machine Theory*, 39(4), 357-377.
- Yoon, W. K., Suehiro, T., Tsumaki, Y., & Uchiyama, M. (2004). Stiffness analysis and design of a compact modified delta parallel mechanism. *Robotica*, 22(04), 463-475.
- Zhang, D., & Gosselin, C. M. (2002). Kinetostatic modeling of parallel mechanisms with a passive constraining leg and revolute actuators. *Mechanism and Machine Theory*, 37(6), 599-617.